

JUL 06 2004

REPORT DOCUMENTATION PAGE			Form Approved OMB No. 0704-0188	
Public reporting burden for this collection of information is estimated to average 1 hour per response, including the time for reviewing instructions, searching existing data sources, gathering and maintaining the data needed, and completing and reviewing the collection of information. Send comments regarding this burden estimate or any other aspect of this collection of information, including suggestions for reducing this burden, to Washington Headquarters Services, Directorate for Information Operations and Reports, 1215 Jefferson Davis Highway, Suite 1204, Arlington, VA 22202-4302, and to the Office of Management and Budget, Paperwork Reduction Project (0704-0188), Washington, DC 20503.				
1. AGENCY USE ONLY (Leave blank)		2. REPORT DATE 30.Jun.04		3. REPORT TYPE AND DATES COVERED DISSERTATION
4. TITLE AND SUBTITLE INTERCOMPARISON OF GLOBAL RESEARCH AND OPERATIONAL FORECASTS			5. FUNDING NUMBERS	
6. AUTHOR(S) MAJ ROMAN JENNIFER C				
7. PERFORMING ORGANIZATION NAME(S) AND ADDRESS(ES) UNIVERSITY OF UTAH			8. PERFORMING ORGANIZATION REPORT NUMBER CI04-400	
9. SPONSORING/MONITORING AGENCY NAME(S) AND ADDRESS(ES) THE DEPARTMENT OF THE AIR FORCE AFIT/CIA, BLDG 125 2950 P STREET WPAFB OH 45433			10. SPONSORING/MONITORING AGENCY REPORT NUMBER	
11. SUPPLEMENTARY NOTES				
12a. DISTRIBUTION AVAILABILITY STATEMENT Unlimited distribution In Accordance With AFI 35-205/AFIT Sup 1			12b. DISTRIBUTION CODE	
13. ABSTRACT (Maximum 200 words) <div style="text-align: center;"> DISTRIBUTION STATEMENT A Approved for Public Release Distribution Unlimited </div> <div style="text-align: center; font-size: 2em; font-weight: bold;">20040713 016</div> <div style="text-align: center; font-weight: bold;">BEST AVAILABLE COPY</div>				
14. SUBJECT TERMS			15. NUMBER OF PAGES 111	
			16. PRICE CODE	
17. SECURITY CLASSIFICATION OF REPORT		18. SECURITY CLASSIFICATION OF THIS PAGE	19. SECURITY CLASSIFICATION OF ABSTRACT	20. LIMITATION OF ABSTRACT

INTERCOMPARISON OF GLOBAL RESEARCH
AND OPERATIONAL FORECASTS

by

Jennifer C. Roman

A dissertation submitted to the faculty of
The University of Utah
in partial fulfillment of the requirements for the degree of

Doctor of Philosophy

Department of Meteorology

The University of Utah

August 2004

Copyright © Jennifer C. Roman 2004

All Rights Reserved

ABSTRACT

Current limitations of atmospheric predictive skill are investigated through comparison of correlation and error statistics of operational and research global models for two boreal winter seasons. In 1993, bias-corrected models produced anomaly correlations of 0.6 after 7 days, with relatively little forecast skill beyond that point. In 2003, the forecast skill of a more developed, higher-resolution operational model has been extended 36-48 h, while the skill of the unchanged, low-resolution research model has been extended 6-16 h. This implies more predictable patterns in 2003 or model and initial state improvements made since 1993. The relative importance of improved model resolution/physics and initial state to the lengthening of forecast skill is diagnosed through the evaluation of root mean square (rms) evolution of analyzed and forecast differences of 500-mb height and meridional wind. Results indicate that forecast sensitivity to initial data is less important than is the sensitivity to the model used. However, the sensitivity to model used (rms of model forecast differences) is comparable or smaller than the rms forecast error of the model, indicating model forecasts are more similar to each other than to reality. Correlations of model errors to each other quantify this similarity, with correlations exceeding the asymptotic value of 0.5 through the 14-day forecasts. Investigations of initial state error evolution by wavenumber show long waves generally account for more of the total uncertainty growth in 14-day research model integrations than do short waves, with the relative importance of each determined by initial state uncertainty and model resolution. Results indicate current predictive skill may be impacted by model sophistication,

but error pattern similarities suggest a common deficiency of models, perhaps in the initial state uncertainty.

TABLE OF CONTENTS

ABSTRACT.....	iv
ACKNOWLEDGMENTS.....	vii
1. INTRODUCTION.....	1
2. DATASETS AND MODELS.....	11
Datasets.....	11
Models.....	12
3. ANOMALY CORRELATIONS.....	15
4. GLOBAL ROOT-MEAN-SQUARE FORECAST AND ANALYZED EVOLUTION.....	28
5. INITIAL STATE ERROR EVOLUTION.....	36
6. RESOLUTION ENHANCEMENT IN UGM.....	53
Model.....	53
Initial States.....	54
Anomaly Correlation.....	54
Spectral Binning of Initial State Uncertainty.....	59
7. EULER MODEL.....	66
8. EULER CORRELATIONS AND BIAS.....	72
9. EULER ROOT-MEAN-SQUARE AND FORECAST EVOLUTION.....	82
10. SUMMARY AND CONCLUSIONS.....	86
Appendices	
A. EULER MODEL DESCRIPTION.....	96
B. ASYMPTOTIC LIMITS FOR CORRELATION COEFFICIENT.....	107
REFERENCES.....	109

ACKNOWLEDGMENTS

I would foremost like to thank my advisor, Dr. Jan Paegle, for his guidance, encouragement, support and humor. Through him, I learned much more than could ever fit in a dissertation. I would also like to thank Dr. Julia Nogues-Paegle, Dr. Gonzalo Miguez-Macho, Dr. Jay Mace and Dr. Jim Steenburgh for their invaluable inputs to this dissertation, and for taking the time to serve on my committee. Additionally, I would like to thank Dr. Jan Paegle and Dr. Julia Nogues-Paegle for the opportunity to travel to Bolivia as part of the South American Low-Level Jet Experiment, a once-in-a-lifetime experience I will never forget.

This dissertation is a direct outgrowth of the love and support of my mom and dad, who taught me that I can do anything if I put my mind to it. To my husband, I offer many, many thanks for his support and encouragement, and dedicate this dissertation to him, and to our two furry boys. They make it all worthwhile.

Finally, I would like to extend my thanks to all of my friends in Utah, and especially to Lee, Eleonora, Ken and Mario.

This research was supported by NSF Grants ATM0109241 and ATM0106776 to the University of Utah, and by the United States Air Force. The views expressed in this dissertation are those of the author and do not reflect the official policy or position of the United States Air Force, Department of Defense, or the U.S. Government.

CHAPTER 1

INTRODUCTION

A number of atmospheric forecast models have been developed and now display considerable skill in weather prediction. The underlying philosophy of these developments is that improved models and more accurate initial conditions should provide better forecasts. The importance of specific model improvements relative to specific observational enhancements may, nonetheless, still be inadequately understood. White et al. (1999) addressed some of these questions, and suggested the error spread among models of very different configuration and resolution is generally less than the magnitude of the error in any single relatively advanced model. Increased resolution in regional models does lead to some improvement in skill, particularly for heavier categories of precipitation that are not simulated at coarser resolution (White et al. 1999), and recent studies show improvement in wind forecasts due to enhanced model resolution (Hart 2004). This benefit, however, appears to be relatively small for other forecast variables, and is evident only for short-term forecasts in which point validations are made against observations, even in the most highly resolved and dynamically sophisticated approaches.

Various hypotheses have been proposed to explain this result. Some of these note current observing systems contain inadequate resolution of local regions of pronounced dynamic instability. Other explanations of the marginally superior performance of high-resolution models point to the evident difficulties in the validation of forecast features against coarsely spaced observations. All but one of the models studied by White et al. (1999) were limited area mod-

els and these are known to be strongly influenced by lateral boundary conditions supplied at their perimeter (Warner et al. 1997; Paegle et al. 1997). The Medium Range Forecast (MRF) model was the only global model evaluated by White et al. (1999) and that model also provided, or strongly influenced, the lateral boundary conditions of the tested limited area models.

The initial stages of the present research compared two global models [the Utah Global Model (UGM) and the MRF], and followed a hypothesis suggested by Miguez-Macho and Paegle (2000, henceforth MMP). This perspective, which is based upon downscale uncertainty growth, is supported by MMP and by Miguez-Macho and Paegle (2001), and is rooted in the early barotropic model predictability studies of Thompson (1957) and Lorenz (1969). Results obtained by MMP contrast with other recent literature emphasizing the importance of relatively smaller-scale instabilities (e.g., Palmer et al. 1998; Hartmann et al. 1995) of the initial state, and other local error sources (e.g., Rabier et al. 1996). These perspectives and contrasting theories are summarized by MMP, who presented preliminary work suggesting that the dominant source of short-term forecast errors may be the uncertainty of relatively large scales of the initial state.

The present research extends MMP's studies to sort out the relative roles of the modeling technique and initial state uncertainty and continues to probe the limitation to deterministic weather prediction due to inadequate observation of relatively large scales of the atmosphere. Other global model studies attempting to prioritize the relative contributions of initial errors, boundary errors, and model errors to total forecast error include work by Reynolds et al. (1994) and Hacker et al. (2003). Simmons and Hollingsworth (2002) show substantial improvement in forecast accuracy in global operational models over the past decade, and present an extensive list of forecast system changes that may have contributed to forecast improvement over the past two decades.

The first goal of the present research is to compare UGM and MRF forecasts in more detail. Our initial studies of this problem focused on a 17-case forecast sample during boreal winter 1993, and compared research model forecasts executed at horizontal wavenumber 42 triangular truncation with MRF forecasts at horizontal wavenumber 62 triangular truncation. Those results were consistent with the possibility that uncertainty of the initial state represented the greatest limitation to forecast accuracy and implied that details of the model formulation were not equally important. That suggestion is supported in Fig. 1.1, which displays bias-corrected anomaly correlations of the 500-mb height forecasts made by the UGM and MRF with analyses, and also correlations of UGM forecasts with MRF forecasts, averaged globally (Fig 1.1a), over the Southern Hemisphere (Fig1.1b), and over the Northern Hemisphere (Fig1.1c). Bias corrections are applied by extracting the average error of N cases from the individual forecasts:

$$\text{bias corrected forecast} = F^n - \frac{1}{N} \sum_{n=1}^N (F^n - O^n), \quad (1.1)$$

where F^n is the forecasted variable, O^n is the analyzed variable for run number n , and N is the total number of runs in the set of cases (for Fig. 1.1, N is 17). The model bias may also be calculated using a “training period” applied to subsequent independent cases. For example, the bias can be computed from the average error for the 30 days prior to a given date, and then applied to that date. This “a priori” method will be employed in Chapter 3 in order to make comparison of forecasts from models of very different sophistication more realistic.

The bottom three curves of each panel in Fig. 1.1, based on calculations performed by MMP, display bias-corrected anomaly correlations obtained with the two research model forecasts initialized separately with National Centers for Environmental Prediction-National

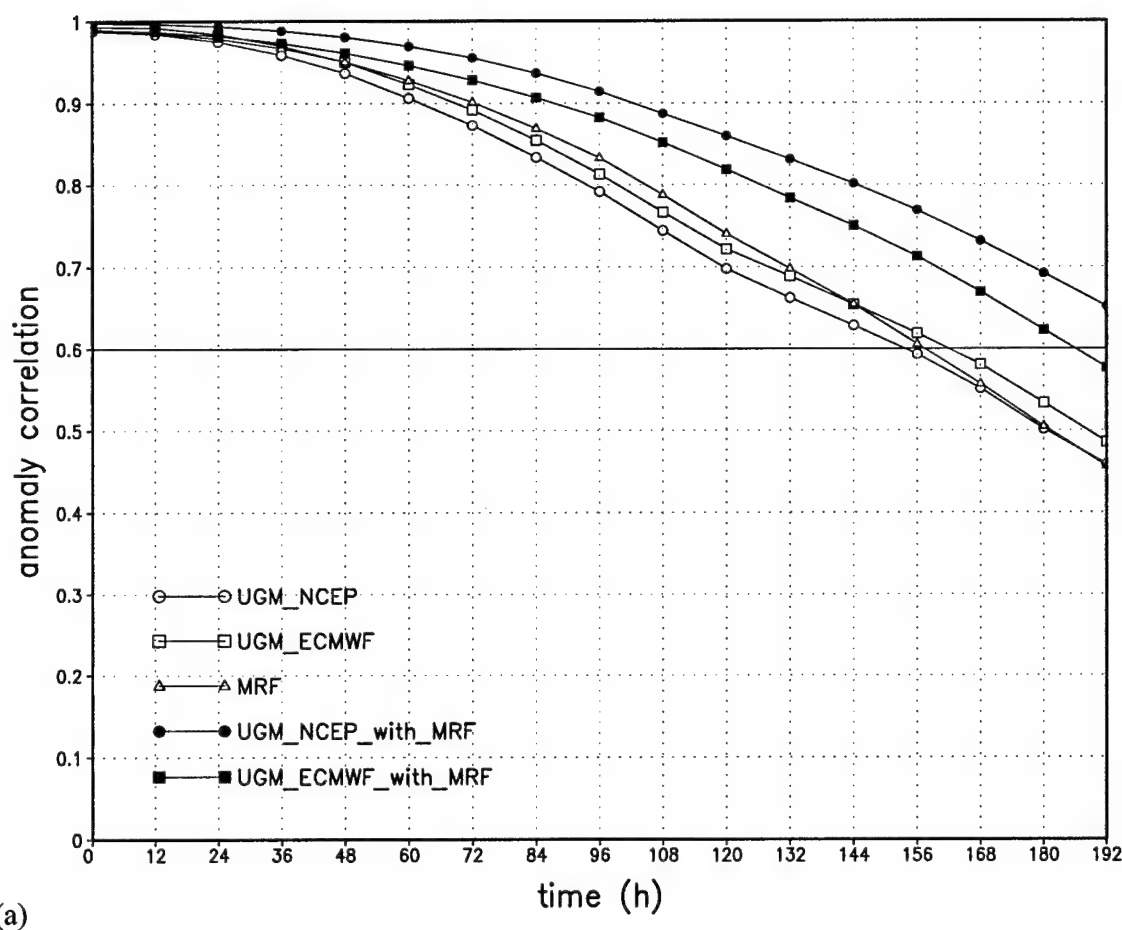
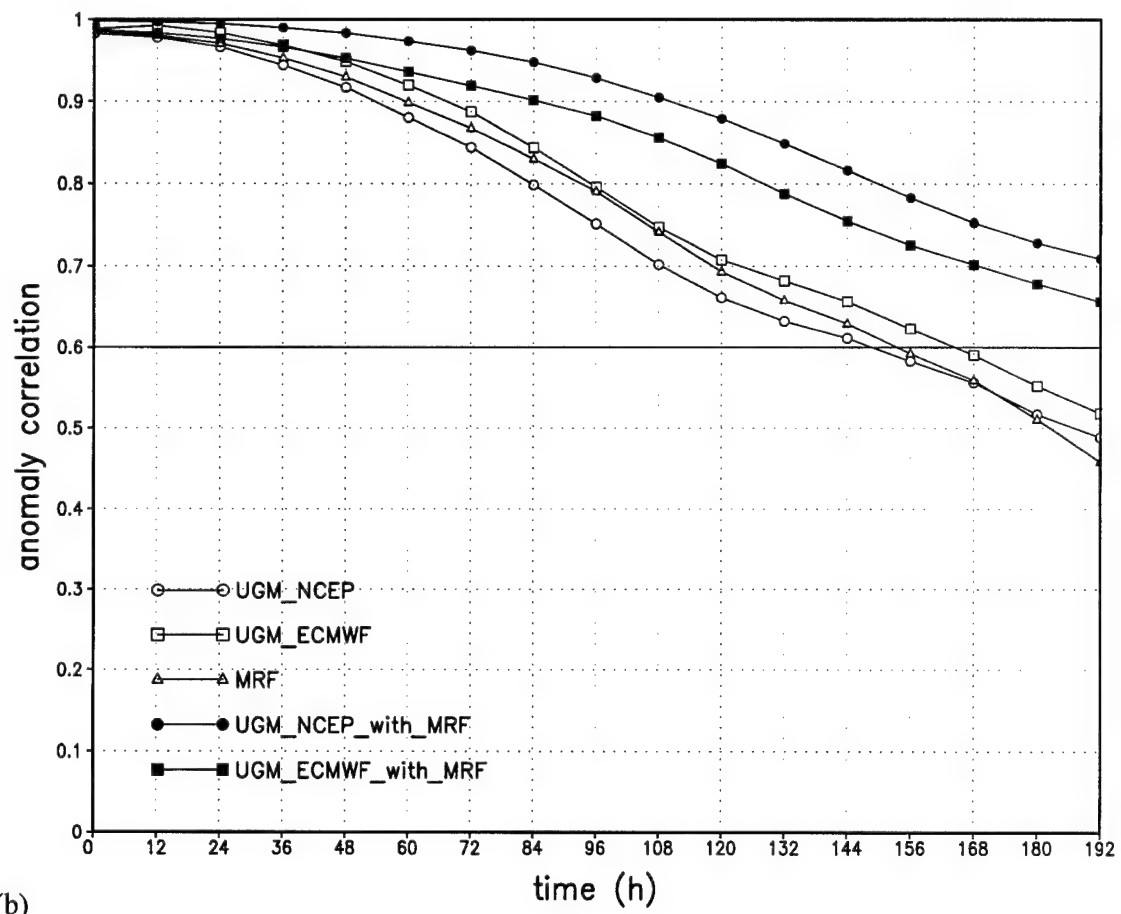
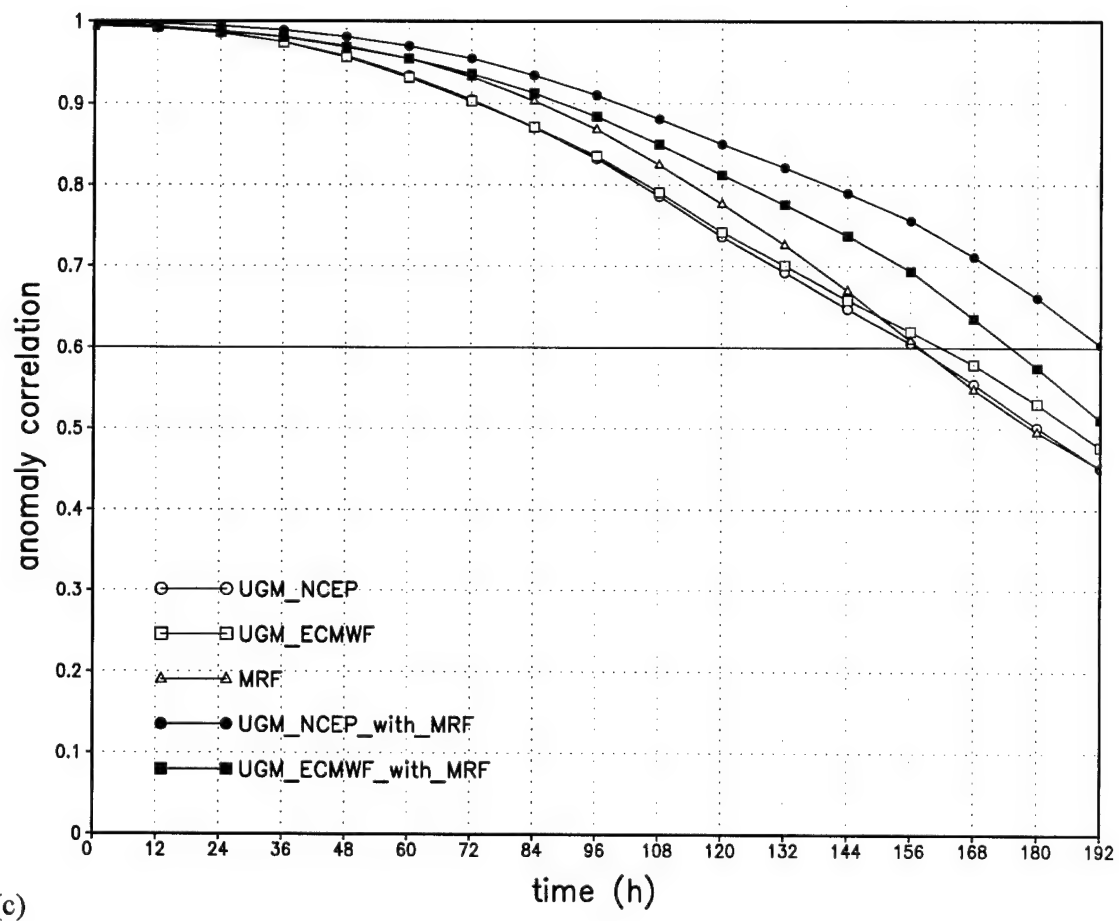


Fig. 1.1. Time evolution of case-averaged anomaly correlations of the 500-mb geopotential height, for the UGM initialized with NCEP-NCAR (open circles) and ECMWF (open squares) reanalyses and the MRF (triangles), each correlated with analyses, and for the UGM initialized with NCEP-NCAR (closed circles) and ECMWF (closed squares) reanalyses each correlated with the MRF. Correlations are averaged (a) globally, (b) over the latitude band from 90° to 20° S, and (c) over the latitude band from 20° to 90° N.



(b)

Fig. 1.1. (continued)



(c)

Fig. 1.1. (continued)

Center for Atmospheric Research (NCEP-NCAR) and European Centre for Medium-Range Weather Forecasts (ECMWF) reanalyses, and of the MRF model initialized with NCEP-NCAR reanalyses. As expected, the MRF model is more accurate than the research model globally and over the Northern Hemisphere, but only by a relatively small amount. The bias-corrected UGM lags the bias-corrected MRF model predictions by only about 12 h, and both show similar skill after seven days when the anomaly correlations drop below 0.6 for each model. In the Southern Hemisphere, the bias-corrected UGM initialized with ECMWF data slightly outperforms the bias-corrected MRF throughout the forecast period. When calculating model errors used for statistics, forecasts from each model were not truncated to the same resolution. Although this may have unfairly penalized the higher-resolution model (MRF), which has more finescale structure, the MRF still outperforms the UGM in nearly all comparisons, and without the bias correction, the MRF forecasts retain predictability skill 24 h longer than do the UGM forecasts. The top two curves of the panels in Fig. 1.1 display bias-corrected anomaly correlations of two UGM forecasts (initialized with NCEP-NCAR and ECMWF reanalyses) validated against the MRF model forecasts. It is noteworthy that the anomaly correlations of the UGM forecasts with the MRF model predictions are higher than the anomaly correlation of either model with the analysis, particularly when the UGM is initialized with NCEP-NCAR reanalyses. One interpretation of these results is that the research model forecast evolution is more similar to that of the MRF model than either model's forecast evolution is similar to the state of the atmosphere. At eight days, the research model anticipates the MRF model evolution about as well as either model anticipates the analyzed evolution at only six days. Another interpretation is that the error fields of the MRF and UGM exhibit strong correlation through eight days, implying a similar error source for both models.

The UGM retains lower horizontal resolution and fewer levels than the MRF model,

and has undergone much less extensive development and calibration. The fact that a relatively unsophisticated and more crudely resolved model possesses such high skill in anticipating the behavior of a much more sophisticated model implies that something other than model complexity provides the fundamental limitation in forecast accuracy for this set of 17 individual cases of the boreal winter of 1993. A possible inference is that both models suffer from the common deficiencies of imperfect initial state specification, and this may represent the primary forecast limitation for these cases. This inference carries important implications for deployment of observing systems and for forecast model development, and merits close scrutiny.

Operational model sophistication, resolution, and initial state specification have undergone substantial improvement in the past decade (Simmons and Hollingsworth 2002). The second goal of the current research is to evaluate this improvement using an up-to-date version of operational model products from NCEP and to compare these results to the research model. The comparison allows a crude estimate of value added by the improved observing system and data assimilation system since 1993, in comparison to model enhancements. Chapter 2 describes the datasets and models used in the prior 1993 comparisons, and more recent datasets and models in real-time comparisons. Chapter 3 presents updated diagrams similar to Fig. 1.1 and quantifies comparisons of recent research and operational products. These results suggest an extension of forecast skill by approximately 6 h in the low-resolution UGM initialized with boreal winter 2003 analyses, and a more substantial extension of approximately 36 h in a more developed, high-resolution version of the MRF model, due both to initial state and model improvements.

There is, therefore, evidence for the important positive role of both improved initial states as well as improved model resolution and formulation. Error diagnostics still suggest a

strong similarity of error structure, consistent with the possibility that initial state error is yet a strongly limiting element. Chapter 5 continues past studies by MMP of the rate of growth of the initial state uncertainty. MMP's experiments were limited by several factors. First, they were integrated for only five days, and it was not possible to establish the timescale on which the uncertainty saturates. Second, they did not demonstrate the relative sensitivity of the forecasts to imposed initial uncertainty in comparison to the sensitivity to model formulation. The integrations were also performed at a relatively coarse wavenumber 42 resolution, which could have limited error growth.

Therefore, a third goal of the present study is to perform a series of further predictability studies with the UGM and compare the results with those from the MRF, with experiments to address each of these issues. In particular, all wavenumber 42 UGM experiments performed by MMP are now extended from five-day to two-week duration; two sets of initial condition sensitivity experiments impose doubled horizontal resolution, and the sensitivity of forecast evolution to the model used is now compared with the sensitivity to the initial state uncertainty. Additionally, UGM cases from 1993 and 2003 were repeated at wavenumber 84 truncation to determine the influence of increased horizontal resolution upon forecast skill and sensitivity to initial state uncertainty.

A final goal of the study is to compare results obtained from the two primitive equation models (UGM and MRF) with those from a third model with a more general dynamical core. The third model contains an Euler dynamical core that retains nonhydrostatic effects as well as compressibility, and is, therefore, less restricted than the primitive equation models. Chapter 7 and Appendix A provide a description of the Euler model used for the comparison, and indicate that there should be no systematic differences between UGM and Euler model forecasts executed at present resolutions. Subsequent chapters will show, however, that inherent model

differences do exist and the choice of model dynamics may impact predictive skill.

The study is organized as follows. Chapter 2 presents brief overviews of the UGM, MRF model, and datasets. Discussion of the Euler model is deferred to later chapters. Chapter 3 describes anomaly correlations of the UGM predictions in comparison to predictions by the MRF model for a boreal winter period in 2002/03. Chapter 4 quantifies the sensitivity of global rms estimates of height and wind forecast changes produced by switching between available models and switching between available initial states, and compares both to analyzed and forecasted changes and to the errors of the changes. Chapter 5 studies the time evolution and correlations of anomaly correlations during boreal winter 2002/03, and sensitivity to initial state uncertainty for model runs at low resolution. Chapter 6 illustrates the impact of doubled horizontal resolution on predictive skill and sensitivity to initial state uncertainty for the UGM. Chapter 7 documents the Euler model used in the present study, and touches on possible inherent differences between that model and the UGM. Chapter 8 describes anomaly correlations of Euler model predictions, and compares bias fields between the two primitive equation models and the Euler model. Chapter 9 quantifies the sensitivity of global rms estimates of forecast changes produced by switching between models with differing dynamical cores, and Chapter 10 presents overall conclusions.

CHAPTER 2

DATASETS AND MODELS

Datasets

Both NCEP, in collaboration with NCAR (NCEP; Kalnay et al. 1996), and the ECMWF (Gibson et al. 1997) have performed gridded retrospective analyses, based upon all available observations, by a frozen state-of-the-art global data assimilation system. Present estimates of initial state uncertainty are obtained from the difference of these two equally credible analyses and are assumed to be reasonable for this study. However, it is likely that this method of characterizing initial state uncertainty underestimates actual values at all scales. In fact, NCEP-NCAR reanalyses have been truncated at wavenumber 36, and, to the degree that ECMWF and NCEP-NCAR use the same observations, the difference in their analyses will underestimate the total error. This limitation to the study is further discussed in Chapter 5.

The 17 cases previously used by MMP were selected for model initialization. These start on 1 January 1993, and continue at five-day intervals through March 1993. The particular dates are chosen because eight-day predictions by the version of the MRF used in the reanalyses are available within the NCEP-NCAR reanalysis archive. This allows comparison of the UGM research model with the MRF model, which is well documented within NCEP technical reports.

In addition to the earlier 1993 ensemble, a set of 52 cases was selected from boreal winter 2002/03 from operational NCEP Global Data Assimilation System (GDAS) analyses

that were available in near-real time. These analyses are archived at 2.5° resolution on 26 vertical levels and extend from 4 January 2003 to 26 February 2003 (two dates were excluded). The set of 52 cases was selected based upon continuous analysis data availability to compute bias statistics, allowing an a priori bias extraction based upon a training period of 30-day duration prior to each UGM and MRF prediction. All errors and anomaly correlations shown subsequently represent bias-corrected values for both the UGM and the MRF unless otherwise stated.

Within the 52-case sample from boreal winter 2002/03, a subset of 30 days was chosen to initialize the Euler model runs discussed in later chapters. Additionally, an even smaller, but still representative, subset of 15 cases (alternate days within the 30-case sample) was used for high-resolution UGM model initialization. Because the Euler model time step is generally one-tenth of that used in the UGM, and the high-resolution UGM time step is one-third that of the low-resolution UGM, larger sample sizes were not possible due to computational considerations.

Models

The UGM is based upon Galerkin approximations applied separately in each spatial dimension. Latitude and vertical structure are depicted by finite elements and longitude variability by Fourier series. The method retains the high accuracy and conservative properties of alternative Galerkin approximations, such as those used in the MRF that are based upon spherical harmonic expansions.

The dynamical core of the model uses a hydrostatic set of primitive equations in which vorticity, divergence, and thermal fields are predicted on pressure-based sigma coordinates.

This approach is similar to that used in global models in operational centers, with the exception of numerical methods outlined above. Model physical parameterizations of convective and stable precipitation are similar to those used by the NCAR Community Climate Model 1 (Bath et al. 1987) introduced in 1987, and parameterizations of radiative and surface processes are also relatively less advanced and follow methods that have been used by other models more than two decades ago. Vertical mixing coefficients are calculated from a low-order turbulent energy equation, and radiation processes include cloud radiation interactions, as described for another model by Nicolini et al. (1993). Moist convective processes use simple convective adjustment, and cloud fraction and condensation criteria are based upon local relative humidity without explicit treatment of cloud microphysics. Sea surface temperature is maintained at the initial value, and land surface evaporation is extracted from the daily analysis files. Each of these processes is treated in a more modern fashion within the MRF. Present applications retain 20 vertical levels and wavenumber 42 resolution. One set of experiments was repeated at wavenumber 84 resolution.

The UGM was originally designed by Paegle (1989) to address predictability questions. It has been used to study impact of wind data voids on objective analyses (Paegle and Horel 1991), for predictability work (Vukicevic and Paegle 1989; Paegle et al. 1997; Miguez-Macho and Paegle 2000, 2001), for idealized global simulations of tropical-extratropical interactions (Buchmann et al. 1995), to study orographically forced regional circulations (Nogues-Paegle et al. 1998; Byerle and Paegle 2003), and for initial data impact investigations of the 1993 "storm of the century" (Miguez-Macho and Paegle 1999a,b).

The MRF model used in the 1993 intercomparisons corresponds to the version used operationally at NCEP until about 1995 and is truncated (triangular) at horizontal wavenumber

62 on 27 vertical levels. The acronym for the MRF changed to GFS (Global Forecasting System) recently, but products from the real-time NCEP forecasts used for the boreal winter 2002/03 cases will continue to be referred to as MRF predictions in this study. These forecasts were executed at wavenumber T254 resolution for the first 3.5 days and subsequently at wavenumber T170 resolution with triangular truncation, on 64 vertical levels (S. J. Lord, 2003, personal communication). The MRF is a spectral model, based upon a set of primitive equations similar to those used in the UGM.

The version of the Euler model used in the present study is relatively new, and has not been previously documented. Therefore, detailed discussion of this model will be deferred to a separate chapter and appendix.

CHAPTER 3

ANOMALY CORRELATIONS

Figure 3.1 compares 500-mb geopotential height anomaly correlations for the recent 52-case real-time forecasts of boreal winter 2002/03 with those for the 1993 experiments, averaged globally (Fig. 3.1a) and over the boreal winter (northern) hemisphere (Fig. 3.1b). The anomaly correlations of forecasts calibrated against observations (in this case, analyses) are computed as

$$\text{anom corr} = \frac{\overline{(S - S_{cl})(S_{ob} - S_{cl})}}{[(S - S_{cl})^2 (S_{ob} - S_{cl})^2]^{1/2}}, \quad (3.1)$$

where S_{cl} represents the climatological value of S and S_{ob} is the analyzed value, in this case taken from GDAS analyses. Here $\overline{(\quad)}$ indicates a global or hemispheric average, and the 50-yr (1951-2000) monthly average derived from the NCEP-NCAR reanalyses is defined as the climatology for this purpose; S represents the forecasted variable from the UGM and MRF. An a priori bias correction is applied to forecast variables using biases calculated from the 30 daily forecasts available immediately prior to the day of interest. The anomaly correlations of UGM forecasts calibrated against MRF forecasts are given by a similar formula, with S replaced by the UGM prediction and S_{ob} by the MRF prediction. Anomaly correlations of the UGM forecasts with the MRF model predictions exceed anomaly correlations of UGM forecasts with

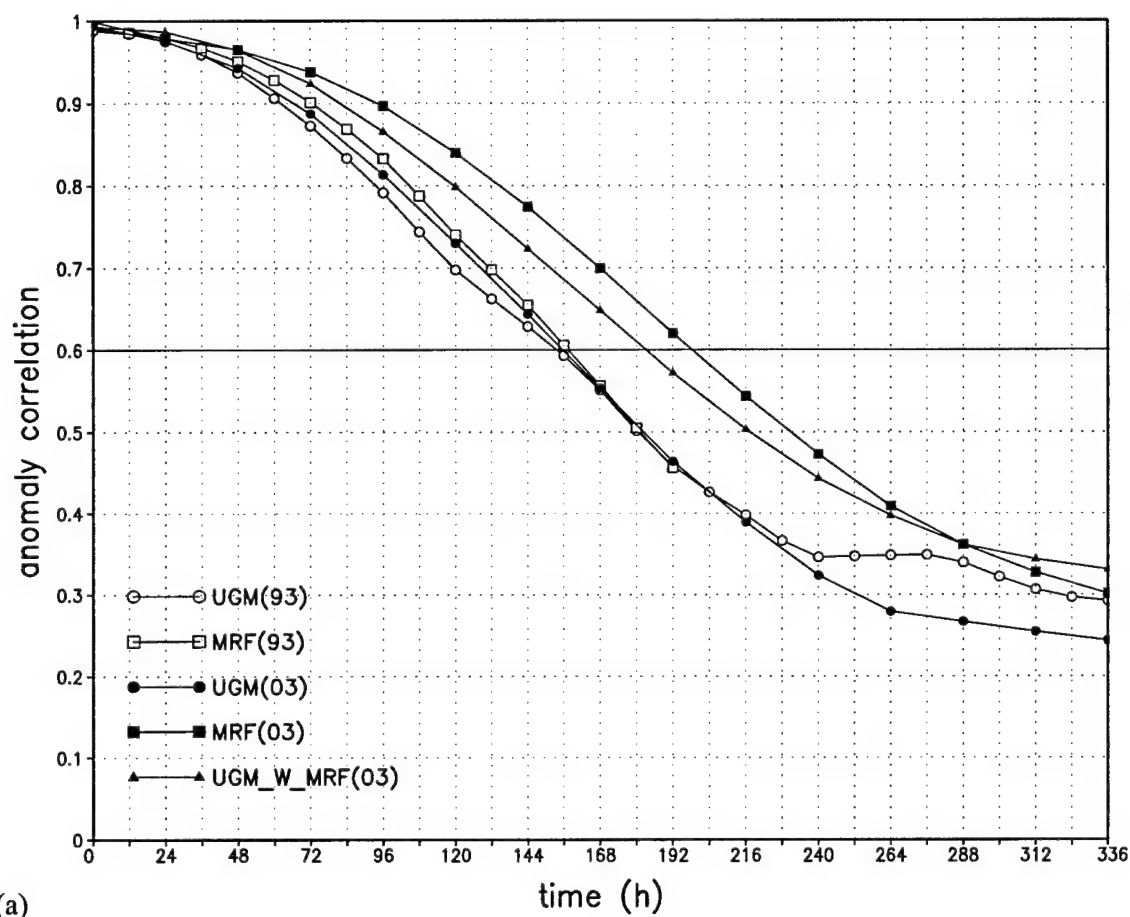


Fig. 3.1. Time evolution of case-averaged anomaly correlations of the 500-mb geopotential height, for the 1993 cases of the UGM (open circles) and the MRF (open squares), and for the boreal winter 2002/03 cases of the UGM (closed circles) and MRF (closed squares), each correlated with analyses; and for the boreal winter 2002/03 cases of the UGM correlated with the MRF (closed triangles. Curves are averaged (a) globally and (b) over the latitude band from 20° to 90° N.

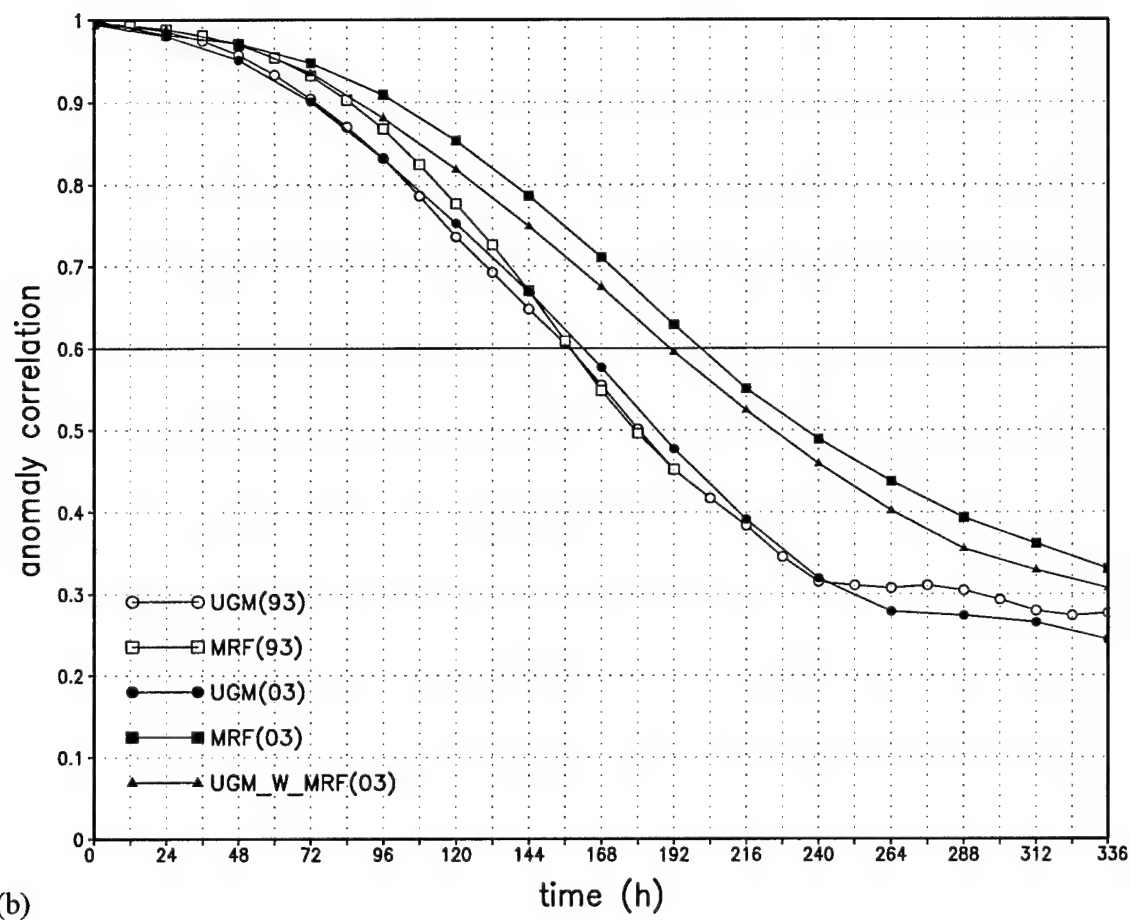


Fig. 3.1. (continued)

analyses when errors of the UGM possess similar structure to errors of the MRF.

The curves with solid squares in Fig. 3.1 represent anomaly correlations of MRF predictions with analyses for the 52 selected cases from boreal winter 2002/03. Substantial improvement is seen with respect to similar results for the 1993 ensemble (curves with open squares). Bias-corrected MRF anomaly correlations for boreal winter 2002/03 drop below 0.6 after approximately 192 h, compared to approximately 156 h for the 1993 cases, corresponding to a 36 h gain in predictive skill at this level by the MRF.

The UGM also produces more skillful forecasts in 2003 than it does in 1993. In the boreal winter hemisphere (Fig. 3.1b), UGM forecasts produce anomaly correlations of 0.6 out to approximately 162 h (curve with solid circles) and represent 6 h longer skill than do those for the 1993 ensemble (open circles).

The MRF has clearly benefited more from advances made at NCEP during the past decade than has the UGM. In the case of the MRF, these advances include substantially higher horizontal and vertical resolution in addition to improved initial state analyses. The only improvement in the UGM is the availability of more modern analyses of the initial state, since UGM resolution and physical formulation are frozen between the 1993 and more recent applications displayed in Fig. 3.1.

A superficial examination of Fig. 3.1 suggests that observation and/or analysis improvements have produced only a 6 h improvement in forecasts over the past decade, since the frozen UGM exhibits only a 6 h forecast improvement in that period. It is unclear, however, how much of the additional 30 h of forecast improvement in the MRF is due to initial state advances relative to model advances over the past decade, or a relationship between the two, since the first guess is such an important component of the data assimilation cycle. A substan-

tial portion of that model's improvement may be due to the improved specification of the initial state in addition to model advances. It is also possible that boreal winter 2003 was more predictable than boreal winter 1993 and this may improve recent skill scores in all models.

The curves with triangles in Fig. 3.1 represent anomaly correlations of the UGM forecasts with forecasts made by the MRF for the boreal winter 2002/03 cases. This curve is only slightly below the anomaly correlation of the MRF forecasts with respect to analyses (curve with solid squares) in the boreal winter hemisphere (Fig. 3.1b). Consequently, the low-resolution UGM forecasts have almost as much skill in anticipating the MRF forecasts as the latter have in anticipating the state of the atmosphere. This implies a correlation of error patterns of forecasts made by the UGM and by the operational model. The similarity of the error patterns of two very different models suggests common limitations, including limitations associated with use of the same initial state.

Figure 3.2 shows an example of the bias-corrected error fields for the 500-mb meridional wind for day 14 (336 h) of forecasts made by the UGM (Fig. 3.2a) and MRF (Fig. 3.2b). Accurate prediction of the meridional flow is important for accurate depiction of wave amplitude and phase, and this variable is more representative of synoptic-scale features than geopotential height, which carries the most amplitude on global scales. Error field structural similarities in the 500-mb meridional flow are particularly evident in northern Canada, over the Eurasian subcontinent, and the eastern coast of Asia in the Northern Hemisphere. In the Southern Hemisphere, two strong error field couplets exist off the southwestern coasts of Africa and Australia in both forecasts. Correlation coefficients (discussed below) for the bias-corrected error fields shown in Fig. 3.2 are 0.61 for global and Northern Hemisphere averages, and 0.62 for the Southern Hemisphere average. Similar agreement in error patterns of the two

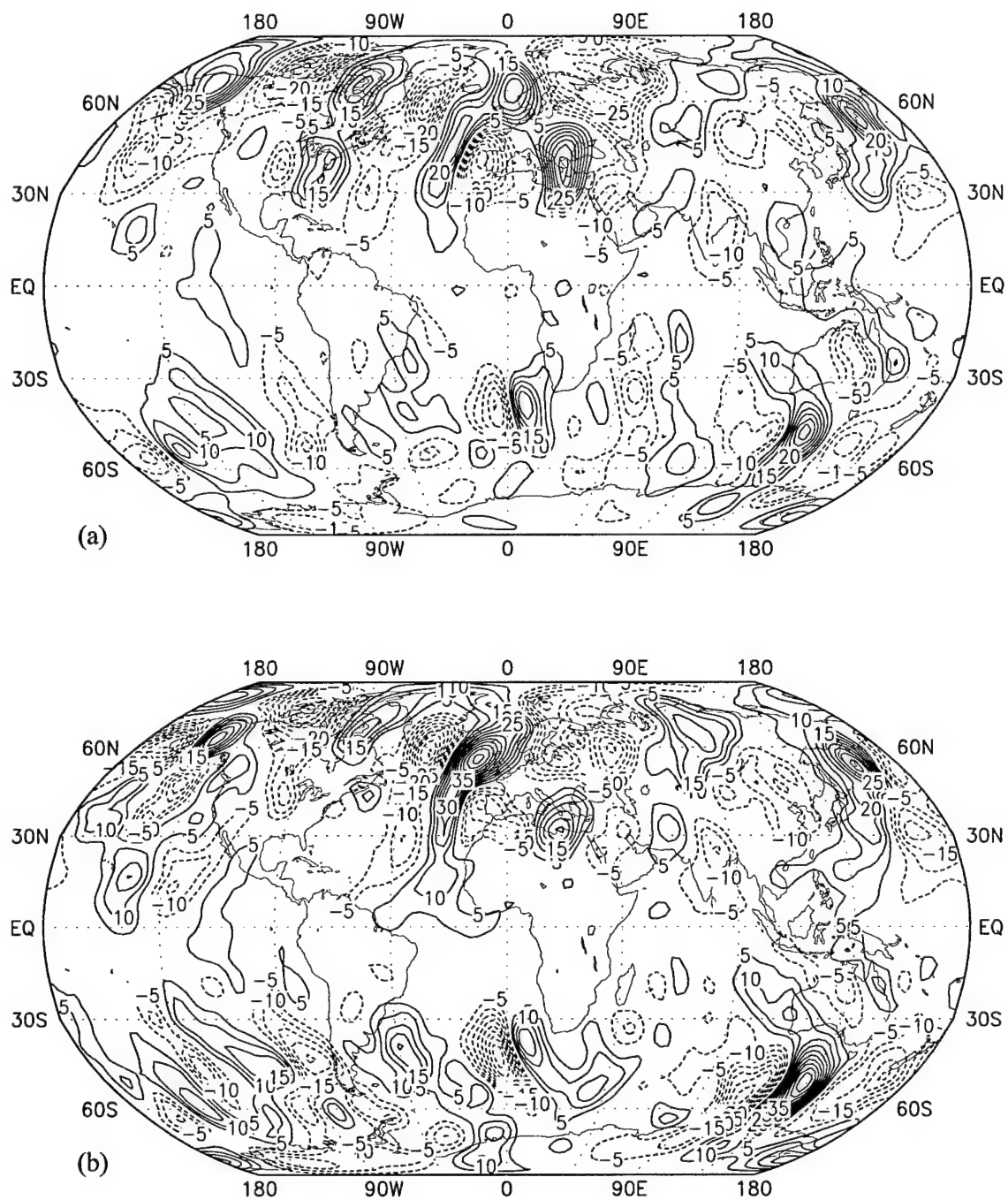


Fig. 3.2. Bias-corrected error fields for the 500-mb meridional wind forecast at hour 336, initialized at 0000 UTC on 26 Feb 2003, for the (a) UGM and (b) MRF model. Contour interval is 5 m s⁻¹.

model forecasts is evident on many other days.

These error fields are computed after removing from each model the bias calculated from the previous 30 days, shown in Fig. 3.3. The bias fields for the 500-mb meridional wind also display remarkable similarity between the UGM (Fig. 3.3a) and MRF (Fig. 3.3b) at day 14 (336 h), despite the difference in model complexity and resolution, implying some common deficiency. Correlation coefficients for the 30-day bias fields shown in Fig. 3.3 are 0.74, 0.72, and 0.81 for the global average, Northern Hemisphere, and Southern Hemisphere, respectively. These clearly exceed the asymptotic correlation limit of 0.5, discussed in appendix B. Furthermore, the overall magnitudes of the 30-day-average meridional flow biases from the models (Figs. 3.3) are comparable to the magnitude of the 30-day-average 500-mb analysis (Fig. 3.4) for meridional wind (Fig. 3.4a). The model biases, therefore, are not negligible.

A comparison of the departures from the zonal mean for the 30-day average 500-mb heights from the reanalysis (Fig. 3.4b) with the departures from the zonal mean of 30-day averages of 500-mb forecasted heights (Fig. 3.5) from the UGM (Fig. 3.5a) and MRF (Fig. 3.5b) also shows a stronger similarity between model forecasts than between either model and the GDAS analysis. Both the UGM (Fig. 3.5a) and MRF (Fig. 3.5b) tend to forecast a ridge over the northern Rockies, while the reanalysis (Fig. 3.4b) indicates that the actual ridge placement is off the western coast of the United States and Canada. Additionally, neither model forecasts the blocking pattern over Europe, and both models underforecast the amplitude of most of the wave structure in the 500-mb pattern.

To further quantify the similarities, Figs. 3.6 and 3.7 display correlation coefficients of the error and bias of the 500-mb meridional flow forecast by the UGM correlated with the error and bias of the same variable forecast by the MRF:

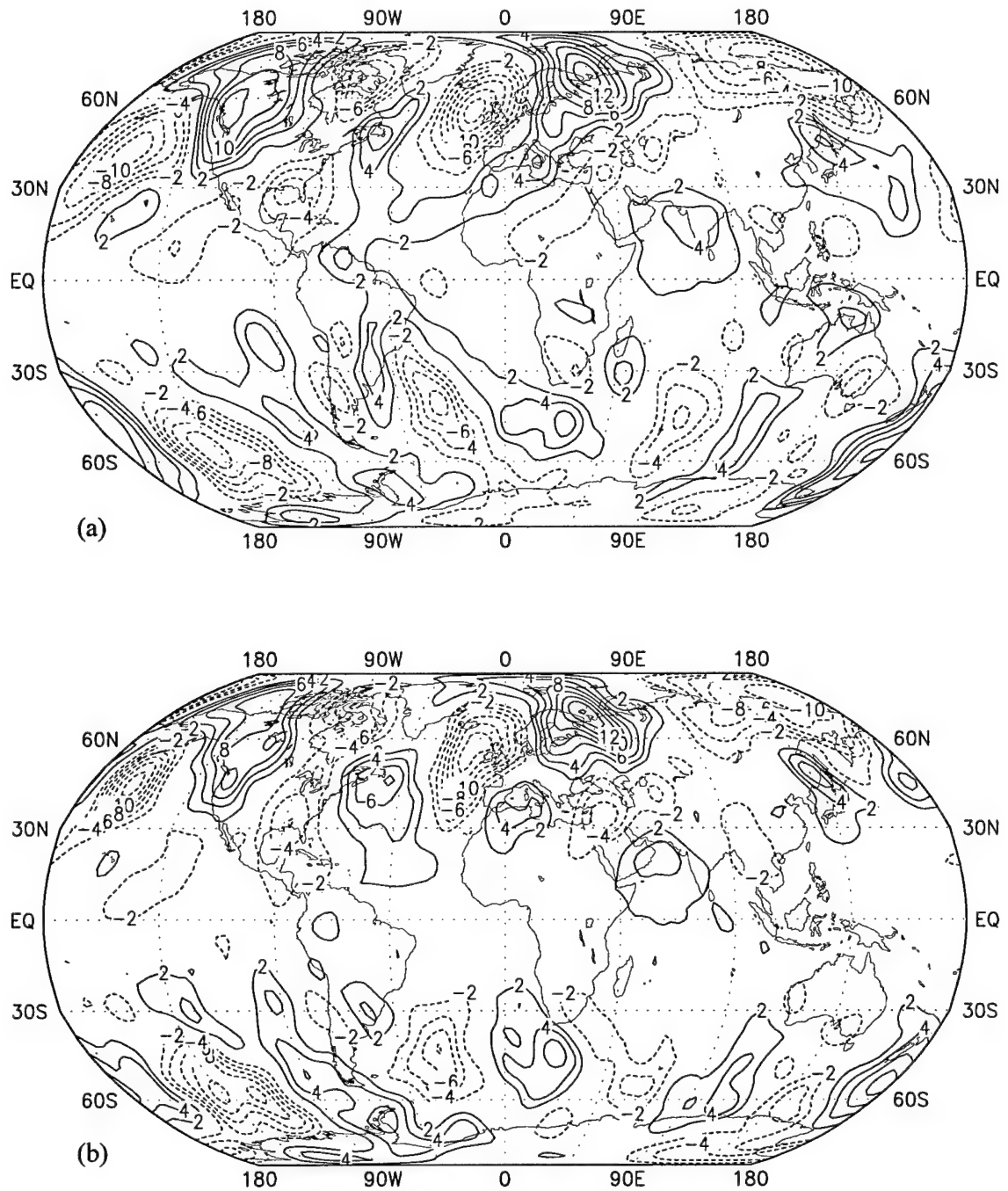


Fig. 3.3. Bias fields for the 500-mb meridional wind at forecast hour 336, calculated for the 30 days prior to 26 Feb 2003, for the (a) UGM and (b) MRF model. Contour interval is 2 m s^{-1} .

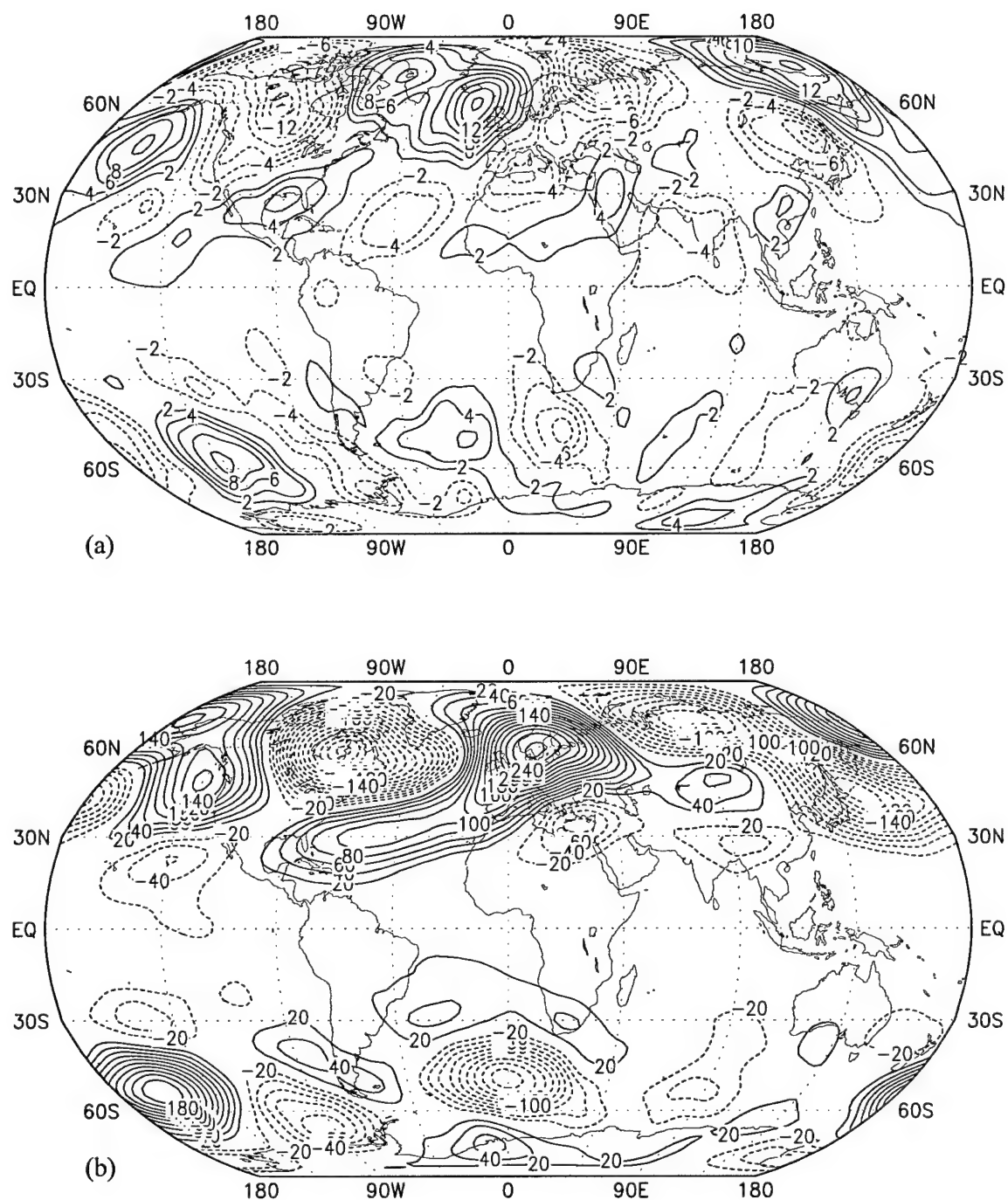


Fig. 3.4. The 500-mb analyses, averaged over 30 days prior to 26 Feb 2003. Contours show (a) meridional wind flow and (b) departure from the zonal mean height analyses. Contour interval is 2 m s^{-1} in (a) and 20 m in (b).

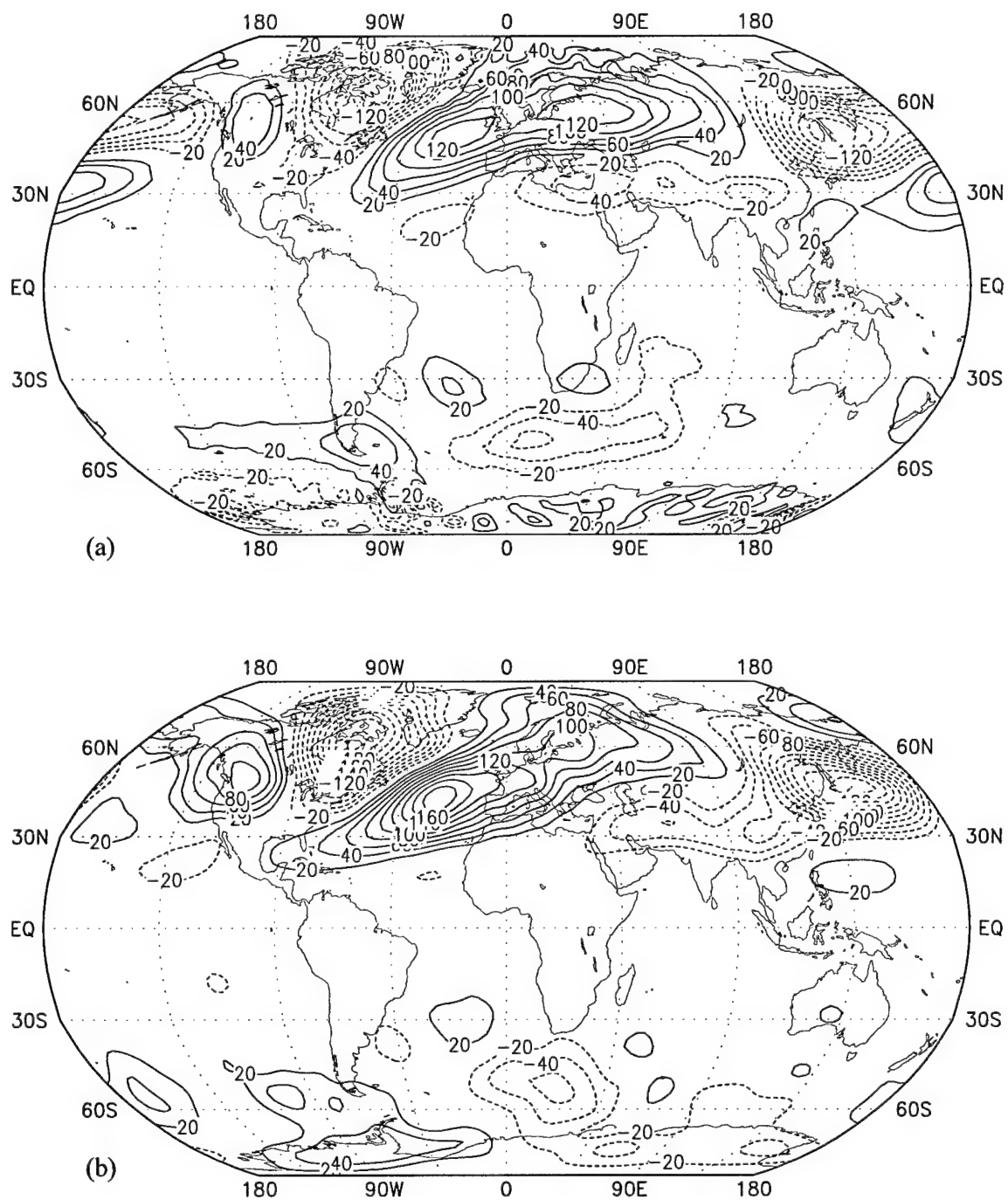


Fig. 3.5. Departures from zonal mean 500-mb height field at forecast hour 336, averaged over 30 model runs prior to 26 Feb 2003, for the (a) UGM and (b) MRF model. Contour interval is 20 m.

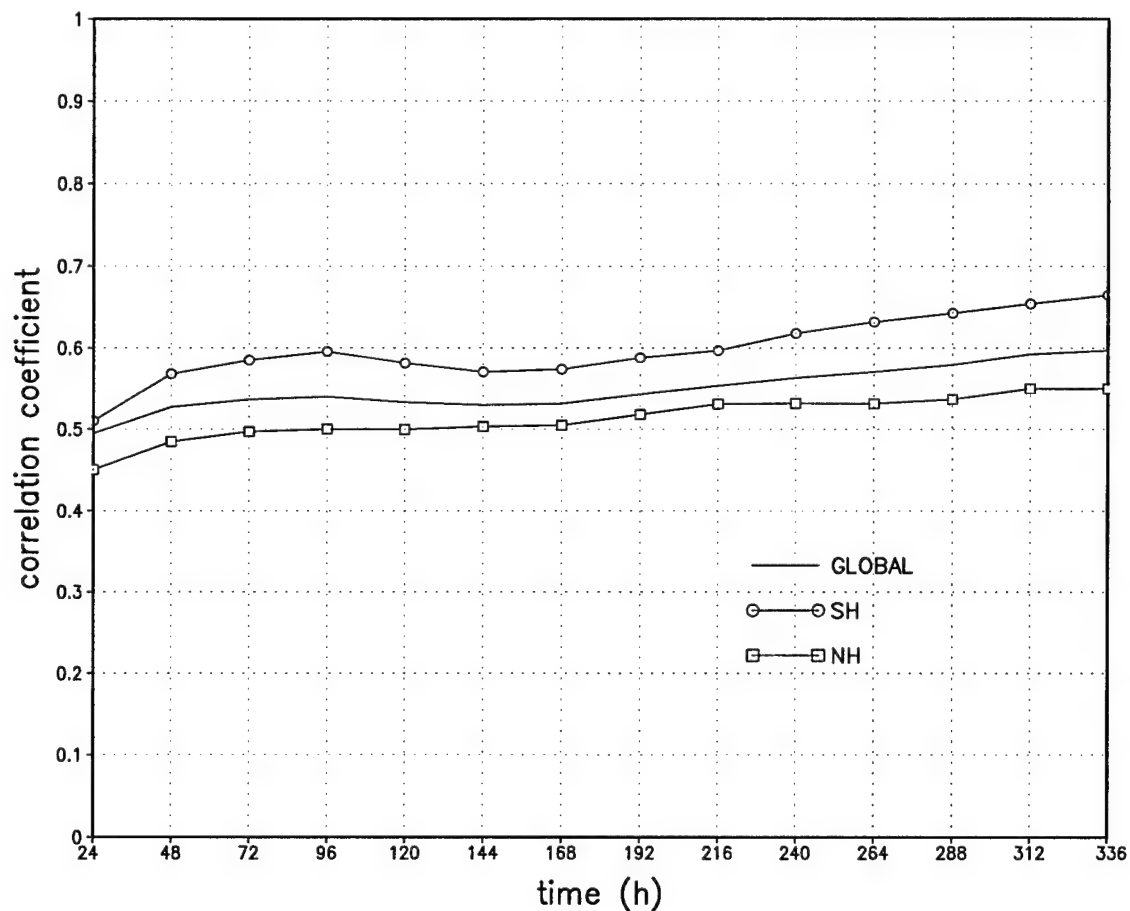


Fig. 3.6. Time evolution of case-averaged correlation coefficients (not bias corrected) of the 500-mb meridional wind error for 30 days preceding 26 Feb 2003, averaged globally (solid), averaged over the latitude band 90° - 20° S (open circles), and averaged over the latitude band 20° - 90° N (open squares).

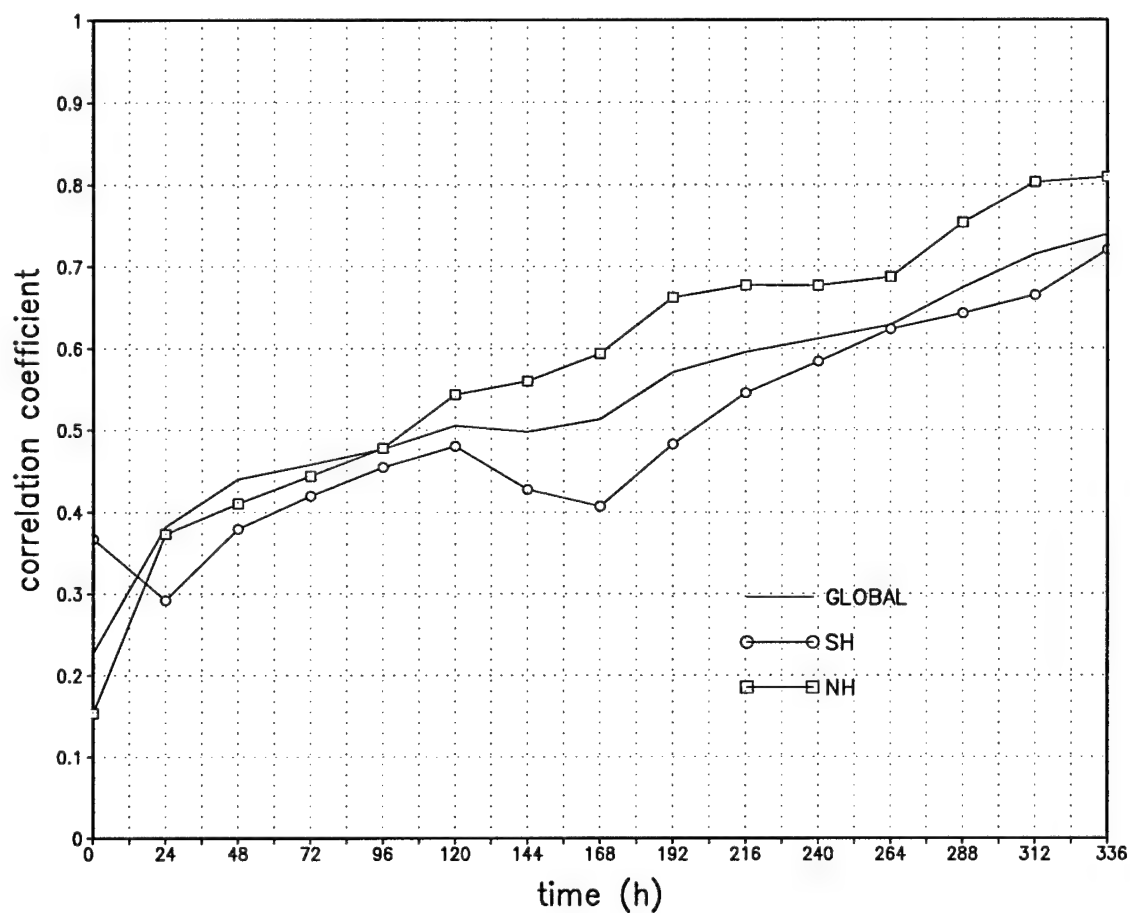


Fig. 3.7. Time evolution of correlation coefficients of the 500-mb meridional wind bias, computed over the 30 days preceding 26 Feb 2003, averaged globally (solid), averaged over the latitude band 90° - 20° S (open circles), and averaged over the latitude band 20° - 90° N (open squares).

$$\text{corr coeff} = \frac{\overline{(S_{UGM})(S_{MRF})}}{[\overline{(S_{UGM})^2} \overline{(S_{MRF})^2}]^{1/2}}, \quad (3.2)$$

where S_{UGM} represents either the error or bias of the 500-mb flow forecasted by the UGM, and S_{MRF} is either the error or bias of the 500-mb flow forecasted by the MRF. Again, $\overline{(\)}$ indicates a global or hemispheric average. This measure of correlation asymptotes to a nonzero value at long times (see appendix B), when predictability is lost due to initial state uncertainty and the chaotic nature of the atmosphere. The time evolution of the case-averaged error field correlation coefficients for a 30-case sample in boreal winter 2003 is shown in Fig. 3.6. The fact that the correlations of errors continue to rise throughout the 14-day forecasts despite initial data uncertainties and chaos may be explained by the growing similarities in 500-mb meridional wind model bias between the UGM and MRF, shown by the correlation coefficients in Fig. 3.7. As yet, however, it is unclear to what the similarity in the bias structure can be attributed.

Given the similarity of errors in models of highly differing complexity, it is tempting to speculate that a fundamental limitation of forecast accuracy is the uncertainty of the initial state, a problem common to all global models initialized with the same or similar data, or inherent errors in model physics or parameterizations common to the global models in question. The next section describes other measures of the forecast sensitivity to model and initial state changes.

CHAPTER 4

GLOBAL ROOT-MEAN-SQUARE FORECAST AND ANALYZED EVOLUTION

Although UGM and MRF model error fields display substantial correlation, the forecasts also exhibit differences and these are most easily summarized in terms of their global rms values:

$$\text{rms} = \overline{(\beta - \alpha)^2}^{1/2}, \quad (4.1)$$

where β and α are some time-specific variable (as described below) and $\overline{(\)}$ indicates a global average. Figure 4.1 displays global rms changes of the analyzed height/wind (β is the analyzed height/wind at time t ; α is the analyzed height/wind at initial time) as well as the global rms magnitude of the forecast change in height/wind (β is the forecast value at time t ; α is the analyzed value at initial time). It also displays the model forecast error for height/wind (β is the forecast value at time t ; α is the analyzed value at time t), and the sensitivity of the height/wind forecast to the model used (β is the UGM forecast value at time t ; α is the MRF forecast value at time t). Finally, the figure displays the sensitivity of height/wind forecasts to model initial condition changes (β is the NCEP-NCAR-initialized UGM forecast value at time t ; α is the ECMWF-initialized forecast value at time t).

The top (solid) curves of Fig. 4.1 depict the global rms evolution of the 1993 analyzed

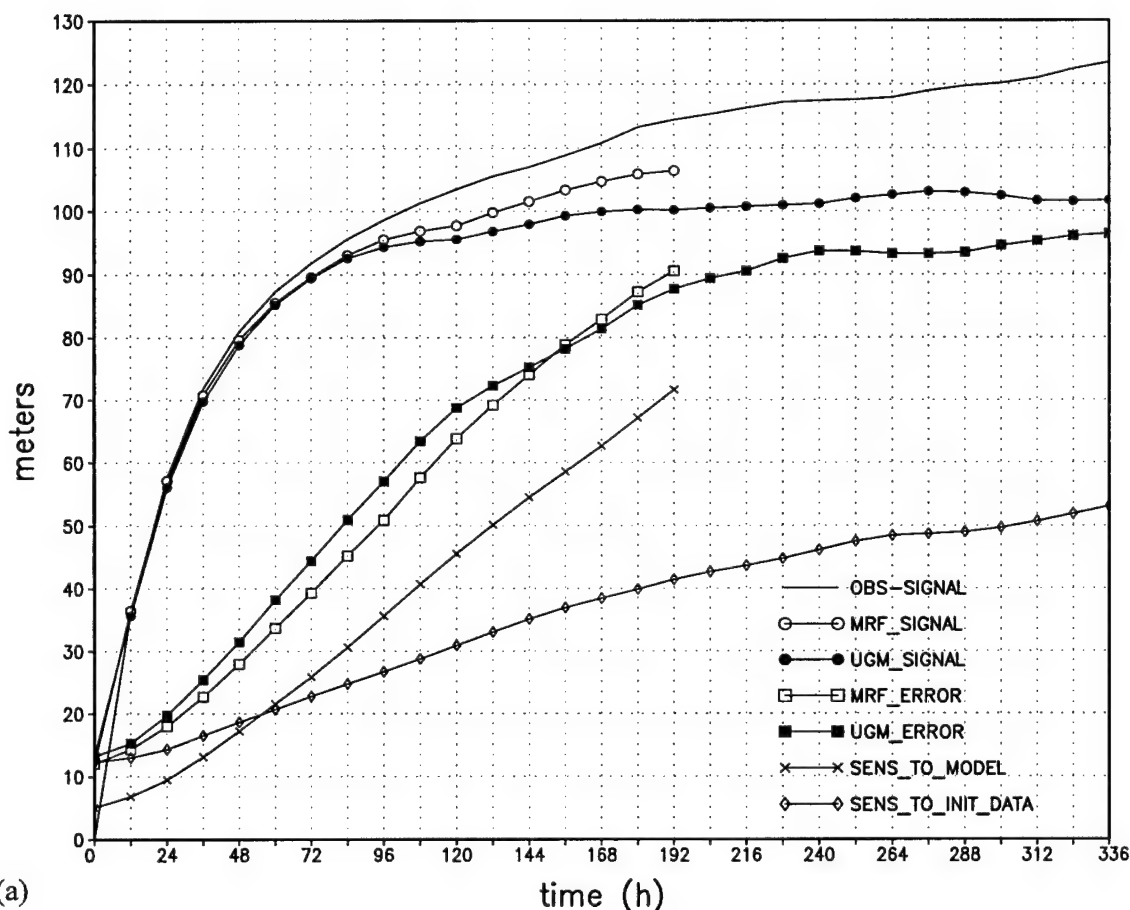
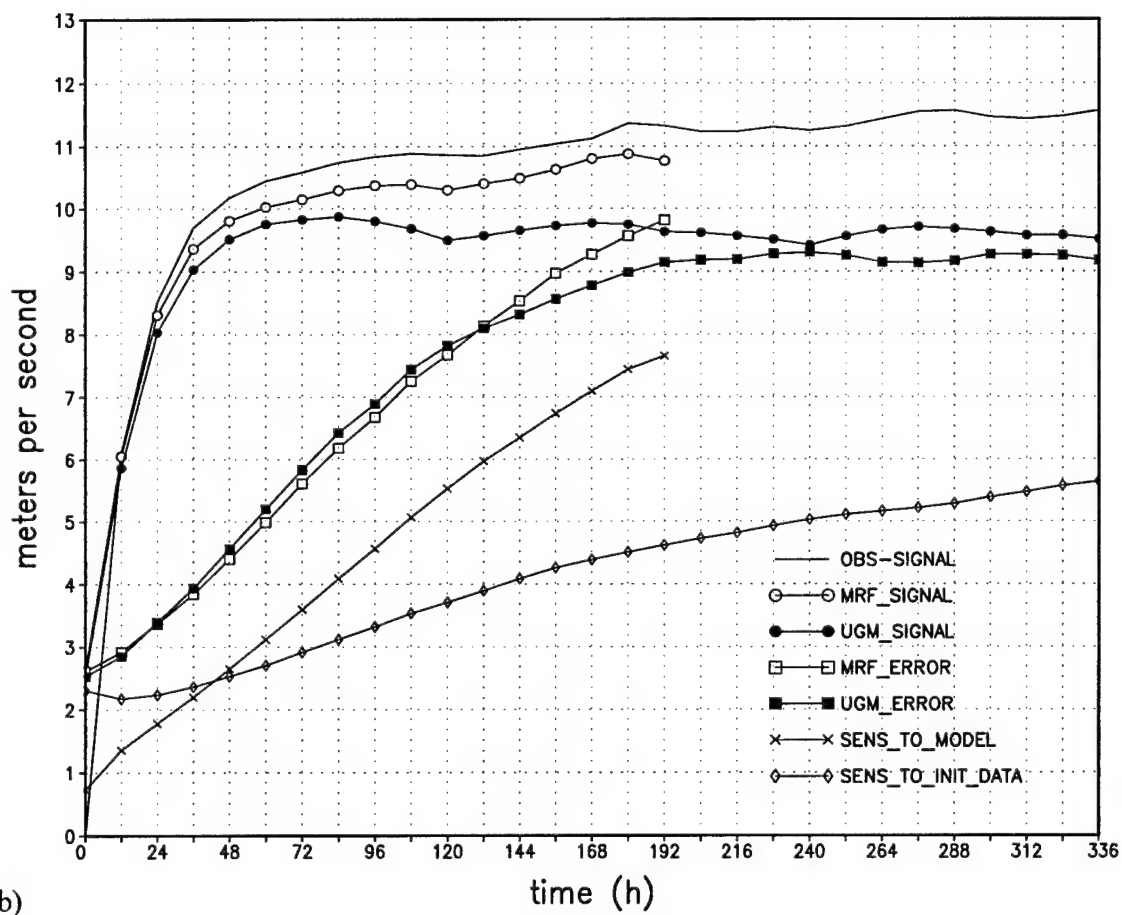


Fig. 4.1. Time evolution of selected global, case-averaged rms variables, for the 1993 cases. The top curve (solid) depicts the differences of the analyzed variable at the time indicated along the abscissa minus the value at 0 h. The second curve (open circles) depicts the differences of the MRF forecast variable at the indicated time minus the analysis at 0 h. The third curve (closed circles) depicts the differences of the UGM (initialized with NCEP-NCAR) variable at the indicated time minus the analysis at 0 h. The fourth curve (open squares) depicts the rms error of the variable forecast by the MRF. The fifth curve (closed squares) depicts the rms error of the variable forecast by the UGM (initialized with NCEP-NCAR). The sixth curve (xs) depicts the difference of the UGM (initialized with NCEP-NCAR) forecast variable minus the MRF forecast variable, and measures the sensitivity of the forecasts to the model used. The seventh and bottom curve (diamonds) depicts the difference of the UGM forecast variable initialized with NCEP-NCAR reanalyses minus that of the UGM initialized with ECMWF reanalyses, and measures the sensitivity of the forecasts to the initial dataset used. Selected variables are 500-mb (a) height and (b) meridional wind.



(b)

Fig. 4.1. (continued)

differences of the 500-mb height (Fig. 4.1a) and meridional wind (Fig. 4.1b) fields, respectively, at the time indicated along the abscissa minus the initial value. This curve is an approximate measure of the observed change in the "signal" associated with each field (i.e., the error of a persistence forecast) and represents the average for the 17 cases. The curve in each diagram immediately below this (open circles), and stopping at 192 h, displays the rms evolution of the respective field from initial to forecast time for the eight-day bias-corrected MRF forecasts. The fact that these curves are slightly lower than the topmost curves suggests that the MRF model maintains slightly less variability than is analyzed in the atmosphere.

This deficiency is even more pronounced in the low-resolution UGM, for which the bias-corrected forecast signal is displayed in the third curve from the top (closed circles) in Figs. 4.1a and 4.1b. The forecasted signal of the UGM is approximately 10%-20% weaker than the analyzed signal. The problem is particularly evident in the geopotential height evolution, for which the rms change from the initial state continues to grow past day 14 (336 h), while this measure of evolution grows very little past day seven (168 h) in the UGM (even though the UGM predicted fields continue to change after day seven).

The fourth curve from the top (open squares), stopping at 192 h depicts the globally computed rms error of the 500-mb geopotential height (Fig. 4.1a) and meridional wind (Fig. 4.1b), for the MRF. The fifth curve from the top (closed squares) depicts the globally computed rms error of the 500-mb geopotential height (Fig. 4.1a) and meridional wind (Fig. 4.1b), for the NCEP-NCAR initialized UGM. These curves asymptote toward the forecasted signal after day 8 and the relative error growth is slowest for the height field and faster for the meridional wind field, as expected.

The bottom two curves in Figs. 4.1a and 4.1b display the sensitivity of the forecast to

the model used (second from the bottom, xs) and to the initial dataset used (diamonds). The curves depicting the sensitivity to the model used are obtained by differencing the forecast produced by the MRF model from that produced by the low-resolution UGM and computing the globally averaged rms of the result for the 17 cases. Through the eight-day period for which this difference field can be calculated, this measure of sensitivity to the model is less than the forecast error of either the UGM or the MRF predictions in each of the displayed fields. This supports the conjecture that forecasts by different models begun with the same initial conditions sometimes resemble each other more closely than they resemble reality.

The bottom curves of Figs. 4.1a and 4.1b show sensitivity to a data switch from NCEP-NCAR to ECMWF reanalyses for initial data. The fact that this curve lies well below the two curves directly above it (forecast error and model sensitivity) may imply that initial data uncertainty is not a very important problem in the 1993 cases. This inference does not have strong support, since certain other features of the forecast evolution imply sensitivity to the initial data, as discussed in the previous section. It is also likely that the present estimate of initial uncertainty (from the difference of ECMWF and NCEP-NCAR analyses of essentially the same observations) underestimates the actual initial state errors. Additionally, the rate of increase of this curve is related to model resolution, and may be a function of model complexity as well. These aspects are discussed in more detail in Chapter 5.

Figures 4.2 displays the same data for the 52 selected cases of boreal winter 2002/03, with all forecasts initialized with GDAS analyses. In general, most of the discussion for the 1993 cases also applies here, although the model forecast error curves have smaller values in 2003 than in 1993 for both the UGM (closed squares) and the MRF (open squares), while the sensitivity to the model (xs) has increased slightly. For boreal winter 2002/03, the sensitivity of

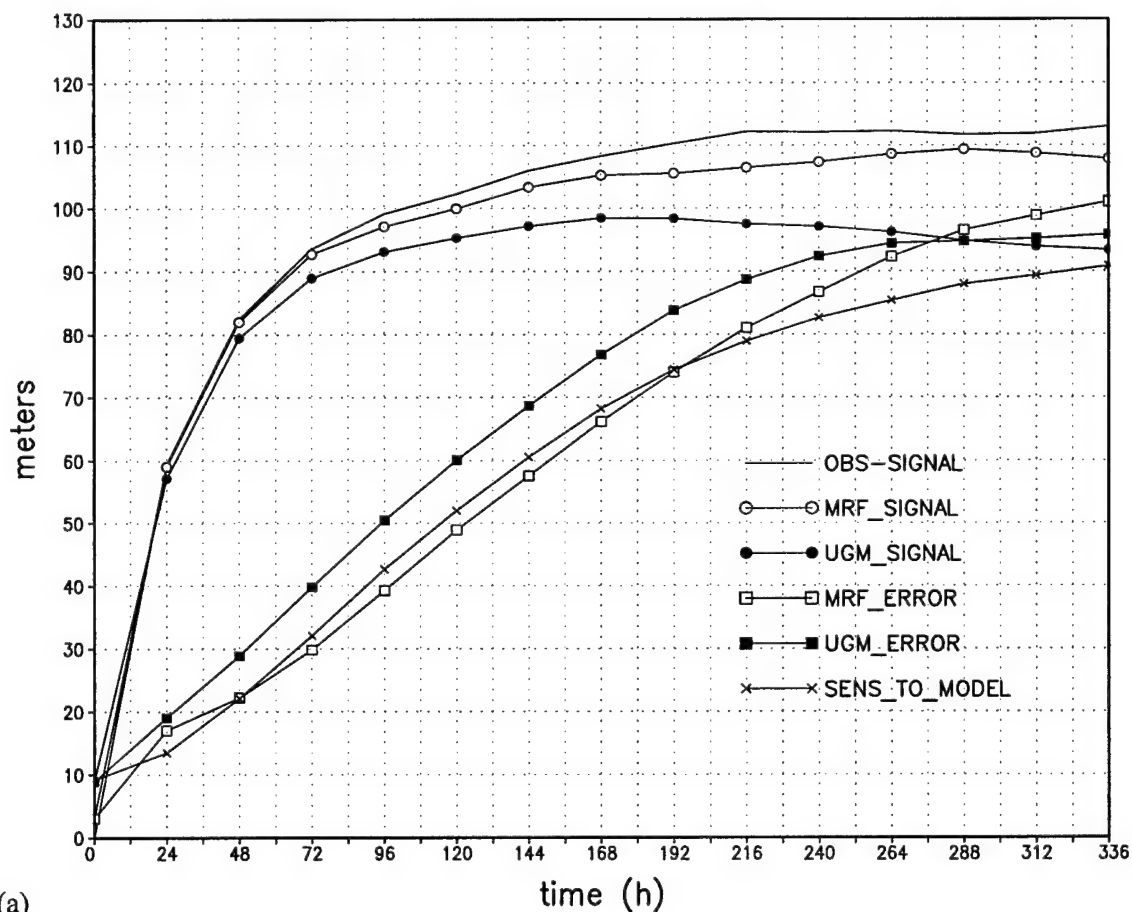
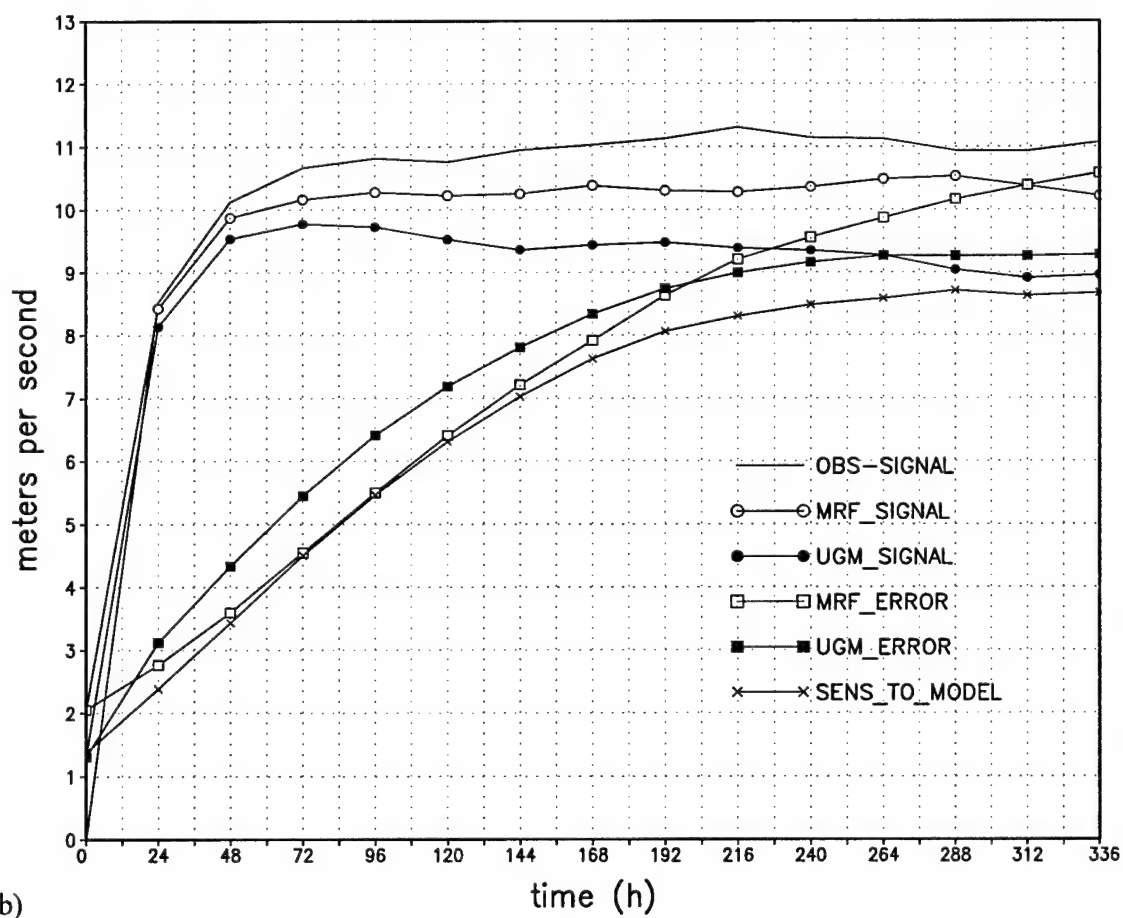


Fig. 4.2. Time evolution of selected global, case-averaged rms variables, for the 2003 cases. The top curve (solid) depicts the differences of the analyzed variable at the time indicated along the abscissa minus the value at 0 h. The second curve (open circles) depicts the differences of the MRF forecast variable at the indicated time minus the analysis at 0 h. The third curve (closed circles) depicts the differences of the UGM variable at the indicated time minus the analysis at 0 h. The fourth curve (open squares) depicts the rms error of the variable forecast by the MRF. The fifth curve (closed squares) depicts the rms error of the variable forecast by the UGM. The sixth curve (xs) depicts the difference of the UGM forecast variable minus the MRF forecast variable, and measures the sensitivity of the forecasts to the model used. Selected variables are 500-mb (a) height and (b) meridional wind.



(b)

Fig. 4.2. (continued)

the forecast to the selected model is about as great as the error of the MRF model, and only slightly smaller than the error of the UGM through the first week of prediction. This result and the substantial positive correlation between UGM- and MRF-predicted error fields discussed in the last section suggest that the two models produce errors that have similar patterns that differ in magnitude. This "distinct tendency for errors in each model to be highly correlated with one another," though remarkable, is not new and was noted in forecast intercomparisons over two decades ago (Baumhefner and Downey 1978).

CHAPTER 5

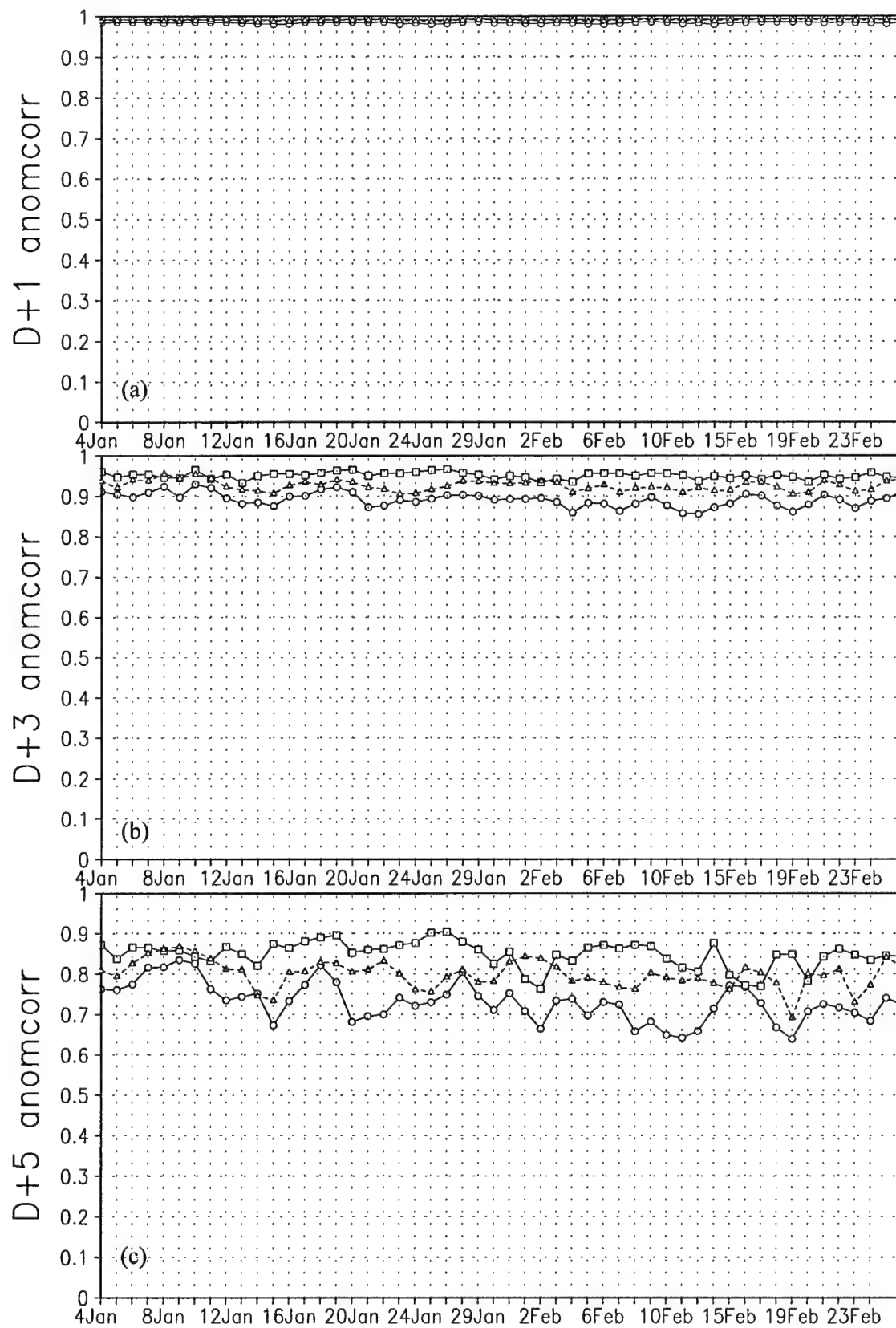
INITIAL STATE ERROR EVOLUTION

The similarity of forecast errors between the UGM and GFS is reflected in positive correlations in the skill scores of the two models. Figure 5.1 displays a 52-day time series from boreal winter 2002/03 of globally-averaged 500-mb height anomaly correlations of UGM (curves with circles) and MRF (curves with squares) forecasts, validated against NCEP's GDAS analyses, and the anomaly correlation of UGM forecasts validated against MRF forecasts (triangles). Results are shown separately for forecast days 1, 3, 5, 7, 9 and 11 (Figs. 5.1a, b, c, d, e, and f, respectively).

There is a tendency for the anomaly correlations of the UGM to show similar time variation to those of the MRF. Skill scores of the two models frequently increase and decrease in tandem, resulting in higher values of model-to-model correlations during these time periods. This trend is quantified in Fig. 5.2, which depicts the variation with forecast day of the correlation coefficient between the average of each of the two solid curves in Fig. 5.1. The correlation coefficient peaks on day one of the forecasts, reduces to a minimum after about four days, and then increases in the second week of the forecasts. Although actual correlation values are low, the qualitative behavior is consistent with the likelihood that both models are similarly limited by initial condition uncertainties early in their forecasts, and by similar bias evolutions at longer times.

Figure 5.1 suggests substantial episodic variability in predictive skill after one week of

Fig. 5.1. Time series of globally-averaged anomaly correlations of the 500-mb geopotential height, for the UGM initialized with GDAS analyses (circles), and the MRF (squares), each correlated with analyses; and for the UGM correlated with the MRF (triangles). Correlations are shown at (a) forecast hour 24, (b) forecast hour 72, (c) forecast hour 120, (d) forecast hour 168, (e) forecast hour 216, and (f) forecast hour 264.



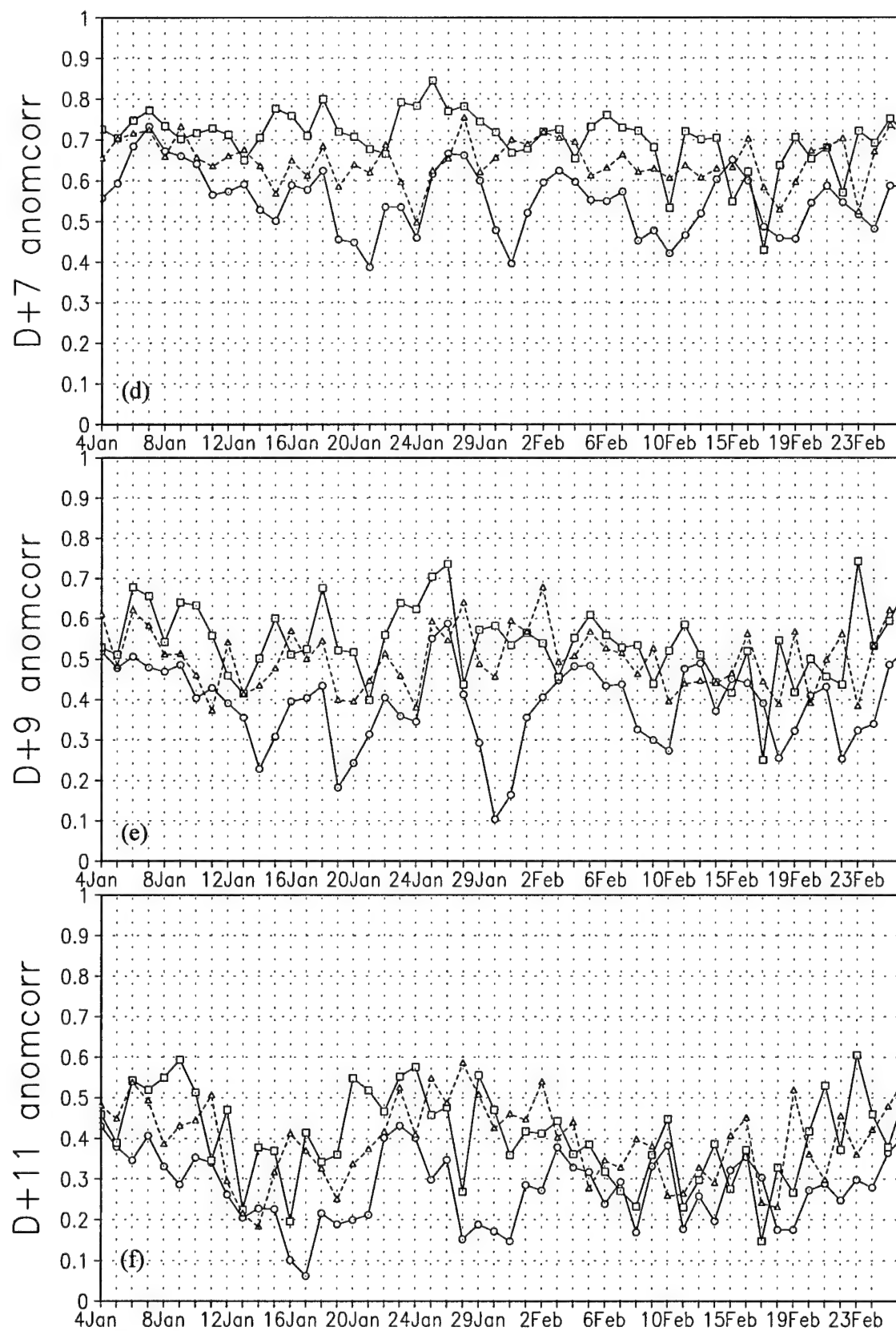


Fig. 5.1. (continued)

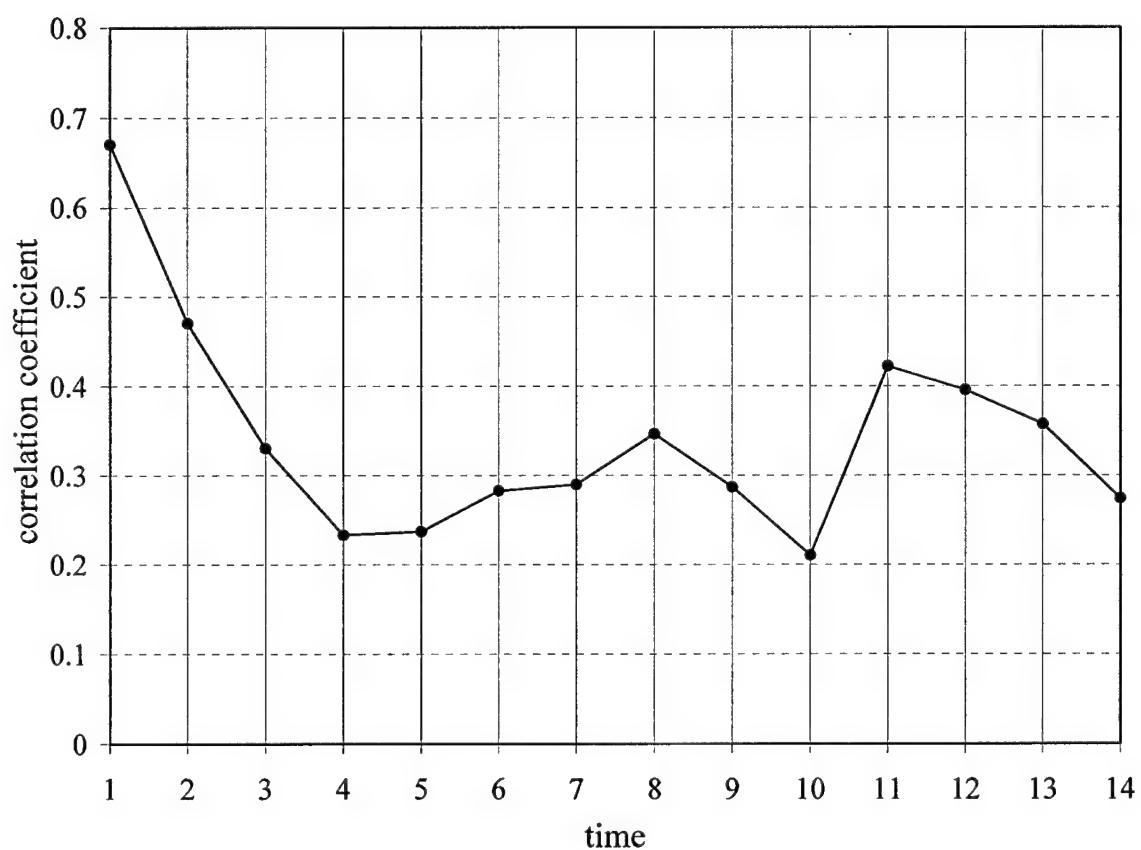


Fig. 5.2. Time evolution of correlation coefficient of boreal winter 2002/03 52-case average bias corrected 500-mb height UGM anomaly correlation to MRF anomaly correlation. Time scale on the x-axis is forecast day.

prediction. The MRF exhibits skill scores around 0.8 on several seven-day forecasts (Fig. 5.1d), and skill scores below 0.6 for seven-day forecasts during other periods. It would be useful to determine whether such highly variable behavior is due mostly to fluctuations in the accuracy of initial state specification, or due to the possibility that different atmospheric configurations are more difficult to predict than others. This important area of research lies outside the scope of the present study.

The curves with triangles in Fig 5.1 also reflect similarity of forecast errors between the two models. These curves represent the similarity of the UGM predictions to the evolution of the MRF. When the values of the model-to-model correlations (triangles) exceed those of the UGM (circles), the UGM and MRF forecasts are more similar to each other than the UGM forecast is similar to the atmosphere. This is almost always the case, as shown in Fig 5.1. On those occasions that the model-to-model correlations (triangles) lies above the MRF correlations (squares), the MRF predictions are more similar to the UGM predictions than to the atmosphere. This occurs 23 different times during the 52 forecasts available for day 11. These results suggest that the errors of the two models are similar, not only for the average of many forecasts as shown in Chapter 2, but also for many individual forecasts.

Once again, results are consistent with a common error source. One shared source of errors is the initial state, which is the same in all of the predictions reflected in Figs. 5.1 and 5.2. The question of which part of the initial state uncertainty may provoke the greatest forecast sensitivity is now discussed.

MMP demonstrated that the influence of initial state uncertainty is far from saturation after five days of simulation by the Utah model. They studied forecast sensitivity to initial state uncertainty due to different complementary wave groups in the total initial uncertainty. The

uncertainty was estimated from the difference of two equally credible analyses of the atmosphere, provided by NCEP-NCAR (T36 truncation) and ECMWF reanalyses of the same state during boreal winter 1993. These analyses, which use the same observations, are very similar over land areas of good observational coverage (see Fig. 5.3 for 500-mb height and wind analysis differences), but they differ more substantially in regions of poor observations, such as the southern oceans.

In qualitative terms, the spatial structures of analysis differences displayed in Fig. 5.3, represent the expected geographical distribution of the initial state uncertainty. In particular, the analysis differences are small over well-observed continents and larger over poorly observed regions of the globe. For this study, it is assumed this difference field provides a reasonable estimate of the actual observation uncertainty. The influence of this level of initial state uncertainty is determined by repeating separate forecasts made by the low-resolution UGM initialized with NCEP-NCAR and with ECMWF reanalyses, and studying the evolving difference fields of the predictions. Following MMP, sequences of experimental cases are performed in which separate spectral wave groups are modified in the initial data, and results are normalized by dividing by the variance of the predicted difference produced by initial state modifications of the entire spectrum. Present results emphasize the response in the meridional wind since this effectively represents the positioning and magnitude of synoptic-scale waves. This quantity also better represents the variability in the Tropics than does the height field.

The results are displayed in Fig. 5.4, which depicts normalized forecast responses to uncertainties retained in different portions of the global spectrum for the 1993 cases. If the forecasts were extended over a sufficiently long period, error growth would saturate, and all the curves of Figs. 5.4a and 5.4b would asymptote to 1.0, and the curves of Fig. 5.4c would

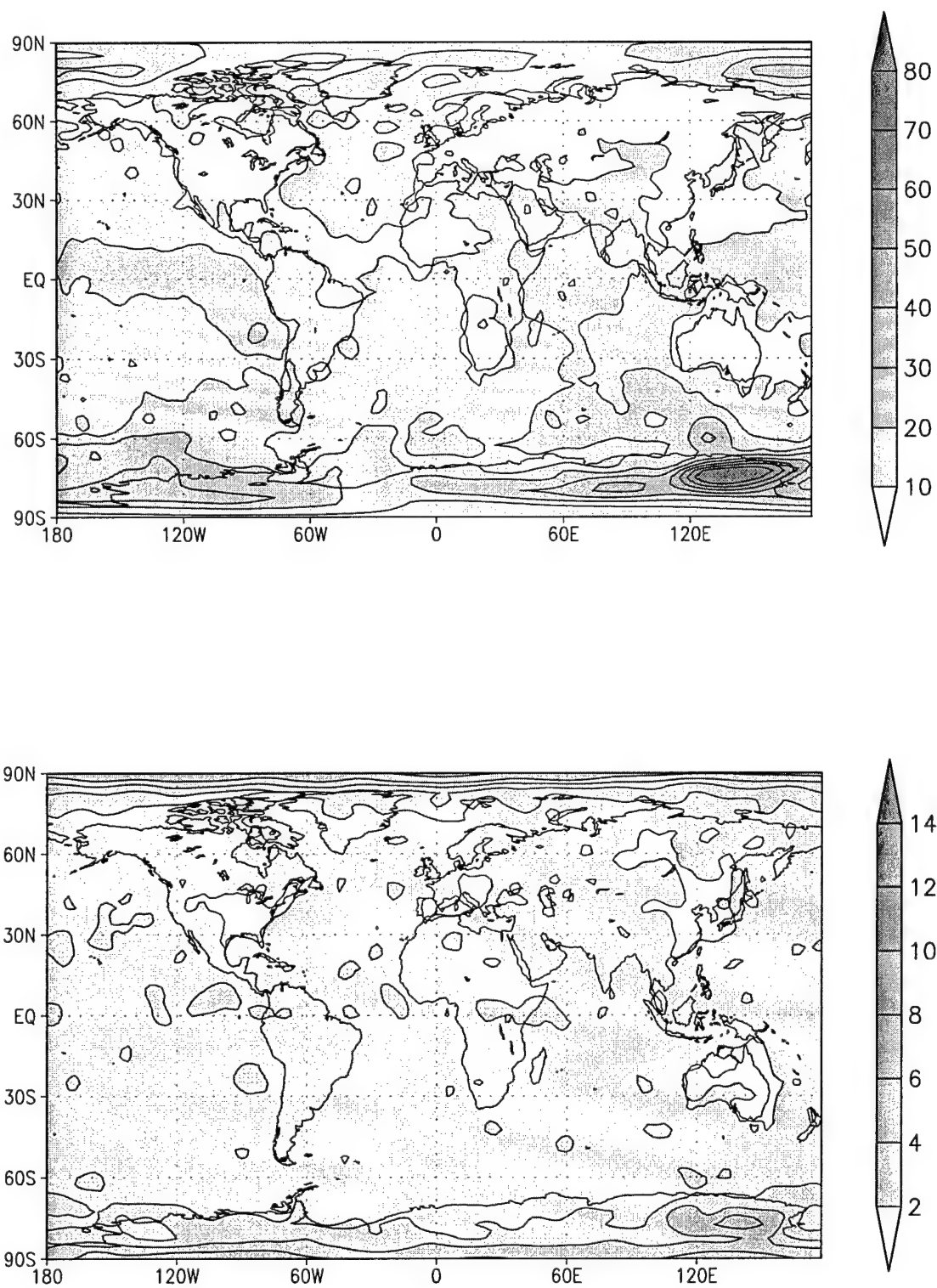


Fig. 5.3. Initial state 500-mb (top) geopotential height and (bottom) wind rms differences between NCEP-NCAR and ECMWF reanalyses for the 17 selected cases of 1993. The units are m in (top) and m s^{-1} in (bottom).

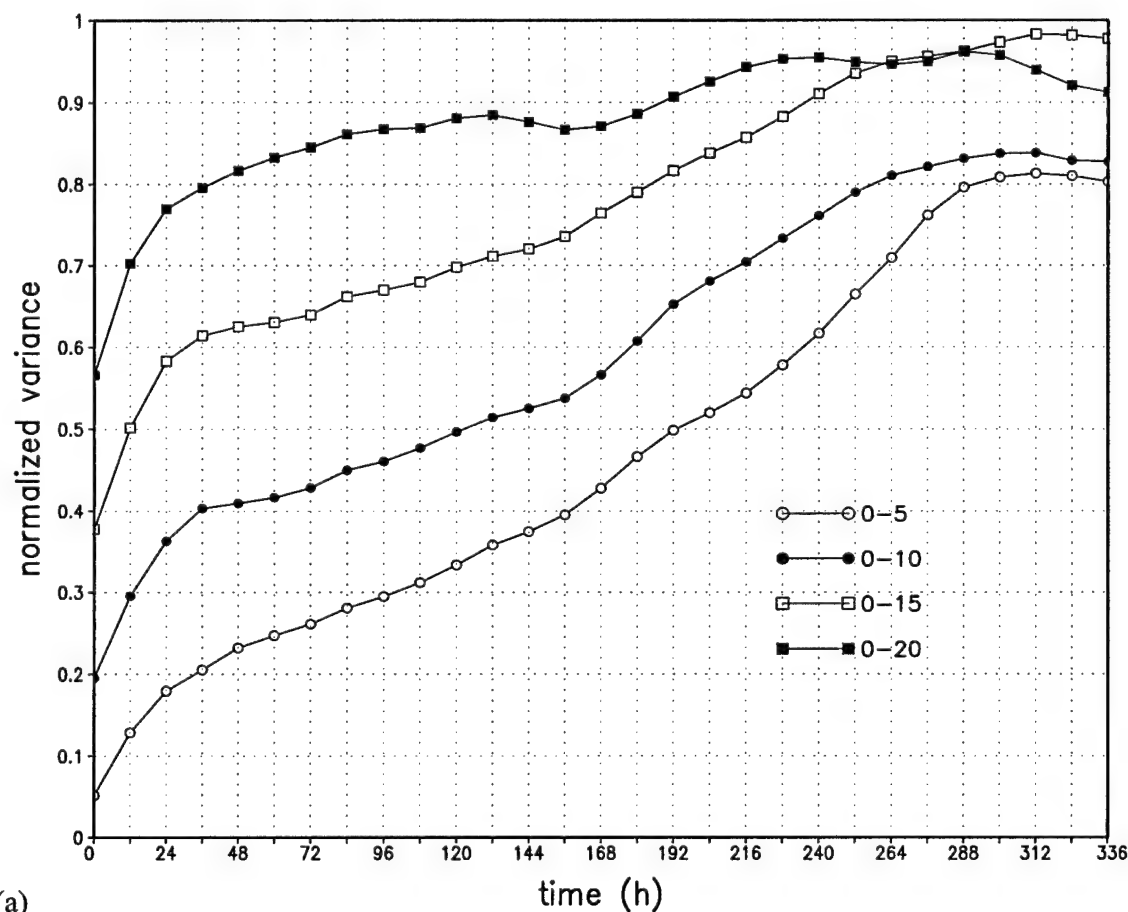
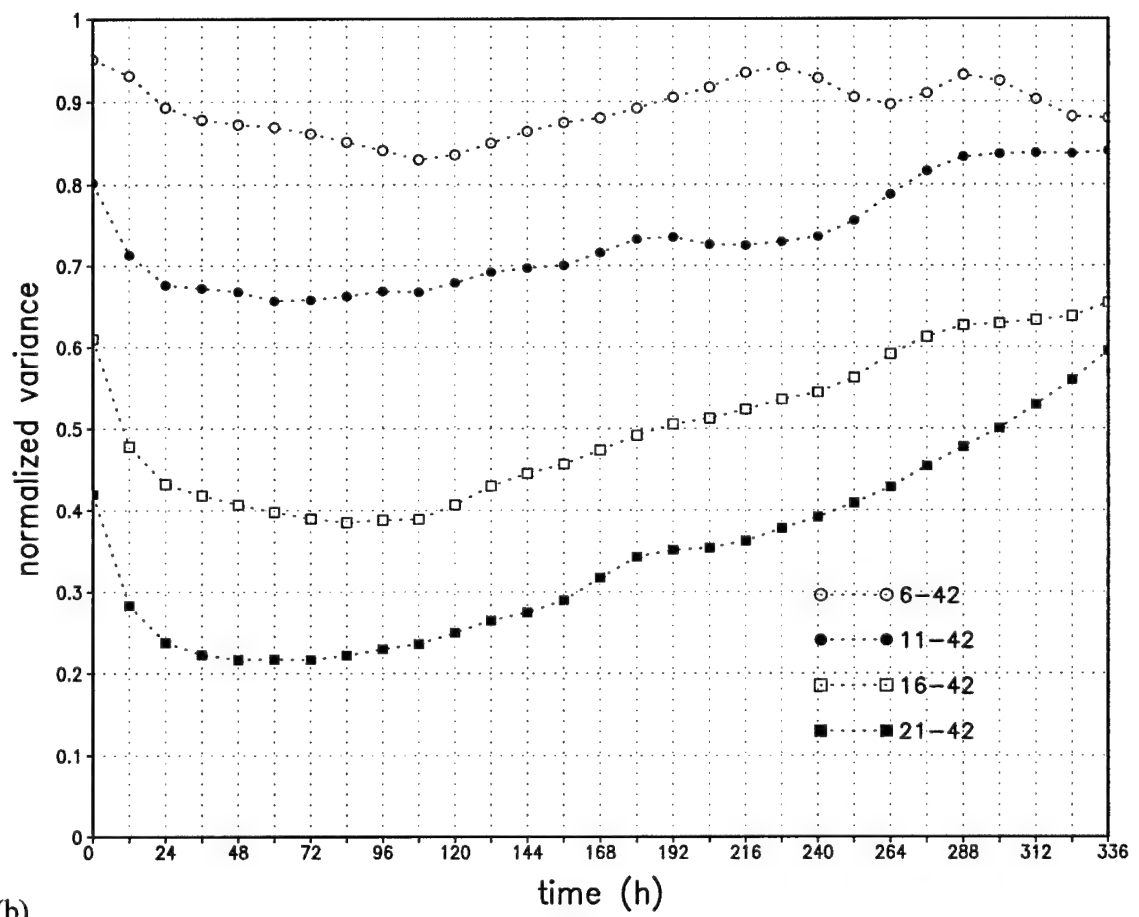


Fig. 5.4. Time evolution of global variances at $\sigma = 0.53$, of forecast meridional flow differences produced by initial data changes from NCEP-NCAR to ECMWF reanalyses for the 17 cases from boreal winter 1993. (a) Curves show the impact of changing the initial data only for global wavenumbers 0-5 (open circles), 0-10 (closed circles), 0-15 (open squares), and 0-20 (closed squares). (b) Curves display the impact of changing the initial data only for the complementary wavenumbers 6-42 (open circles), 11-42 (closed circles), 16-42 (open squares), and 21-42 (closed squares). Results in both (a) and (b) have been normalized by dividing by the variance of the forecast meridional flow differences produced by the initial state change of the entire spectrum. Sums of complementary wave groups in (a) and (b) are displayed in (c).



(b)

Fig. 5.4. (continued)

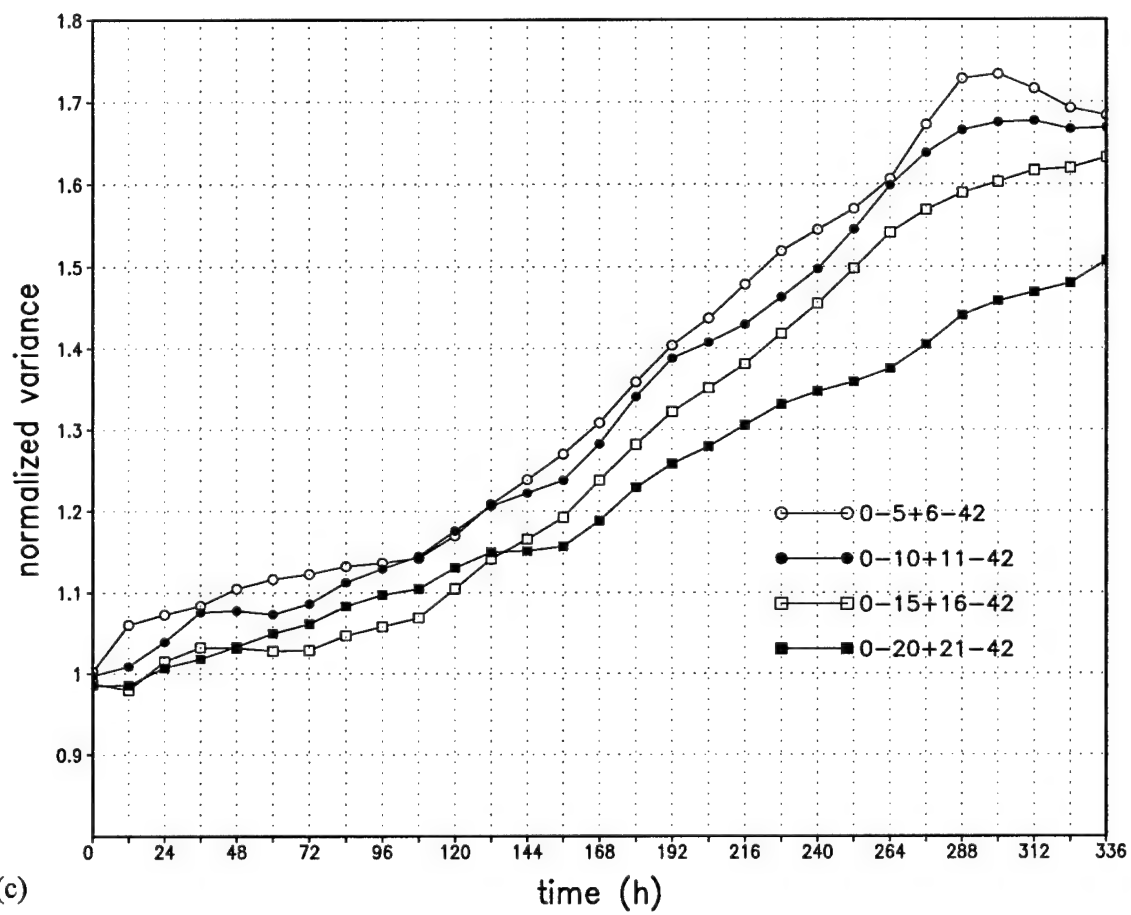


Fig. 5.4. (continued)

then asymptote to 2.0.

MMP produced the results of Figs. 5.4a and 5.4b out to five days (120 h), and noted that sums of normalized uncertainty growth for complementary wave groups approximately equal 1.0 rather than 2.0. They concluded that the first five days of prediction by the Utah model were characterized by slow, linear error growth, which is far from saturation through five days. Within this regime of unsaturated error growth, the effect of changing long-wave components of the uncertainty spectrum produces an error contribution that grows more rapidly in a relative sense than does the effect of changing shorter waves of the initial state. This can be deduced from the initial upward trends of the curves in Fig. 5.4a and the initial downward trends in the curves in Fig. 5.4b.

The present extension to 14-day predictions provides important modifications of these conclusions. In particular, pronounced growth of the sum of the normalized uncertainty contributions in Fig. 5.4c occurs after 120 h, when the sums are on the order of 1.1 or less. By 336 h, the sums exhibited in Fig. 5.4c range from 1.5 to nearly 1.7 suggesting that initial state errors have effectively spread across the full spectrum resolved in the present integrations. Even for this extended prediction the longer-wave uncertainty explains at least as much, or more, of the total error growth than does uncertainty in the shorter waves. Waves 0-15, for example, account for less than 40% of the initial uncertainty in the present experiments in Fig. 5.4a, but produce about 50% more sensitivity at 14 days (336 h) than do waves 16-42 (Fig. 5.4b).

The sums of the relative uncertainty in different spectral groups increase toward approximately 1.5-1.7 in Fig. 5.4c. These curves should asymptote to 2.0 in the limit when errors associated with the chaotic nature of the atmosphere would finally saturate. Simmons and Hollingsworth (2002) suggest that the ECMWF model is close to error saturation after

approximately 21 days. They base this conclusion upon the rate at which model solutions initialized on consecutive days diverge. The present experiments are integrated to only 14 days and use a different method to study error saturation, but an extrapolation of the curves in Fig. 5.4c from the second week shown toward 21 days appears to be consistent with Simmons and Hollingsworth's (2002) conclusion.

The most important limitations to the present conclusions are that they are made using a forecast model truncated at relatively low resolution, and that the differences of NCEP-NCAR and ECMWF analyses, which use the same observations, may not adequately reflect the actual uncertainty of the initial state. Higher-resolution models generally allow larger uncertainty growth because model diffusion coefficients need to increase with coarser resolution to control spectral blocking and to limit the accumulation of energy at the shortest resolvable scales due to nonlinear energy cascade.

It is likely that the present method of initial state uncertainty specification underestimates the actual uncertainty in both large and small scales. In particular, neither analysis contains much amplitude in higher-wavenumber, smaller scale components (wavelengths on the order of 1000 km) and their differences may systematically underestimate the impact of errors at these scales.

White et al. (1999) estimated "errors" of the MRF initial state over the intermountain west of the United States in a region of good radiosonde density. Table 2 of that study suggests that initial rms error values for the wind exceed 4 m s^{-1} in the mid troposphere in a region of reliable observations. These "uncertainties" are estimated from the fit of the initial analyses interpolated to radiosonde observation sites using a horizontal grid corresponding to approximately global wavenumber 100. Presumably, the uncertainties are even larger in regions of

sparse observations. The initial data uncertainties (Fig. 5.3) used in the present experiments are smaller than 4 m s^{-1} over most of the globe, and impose smaller initial state uncertainties than were found by White et al. (1999) in data-rich regions.

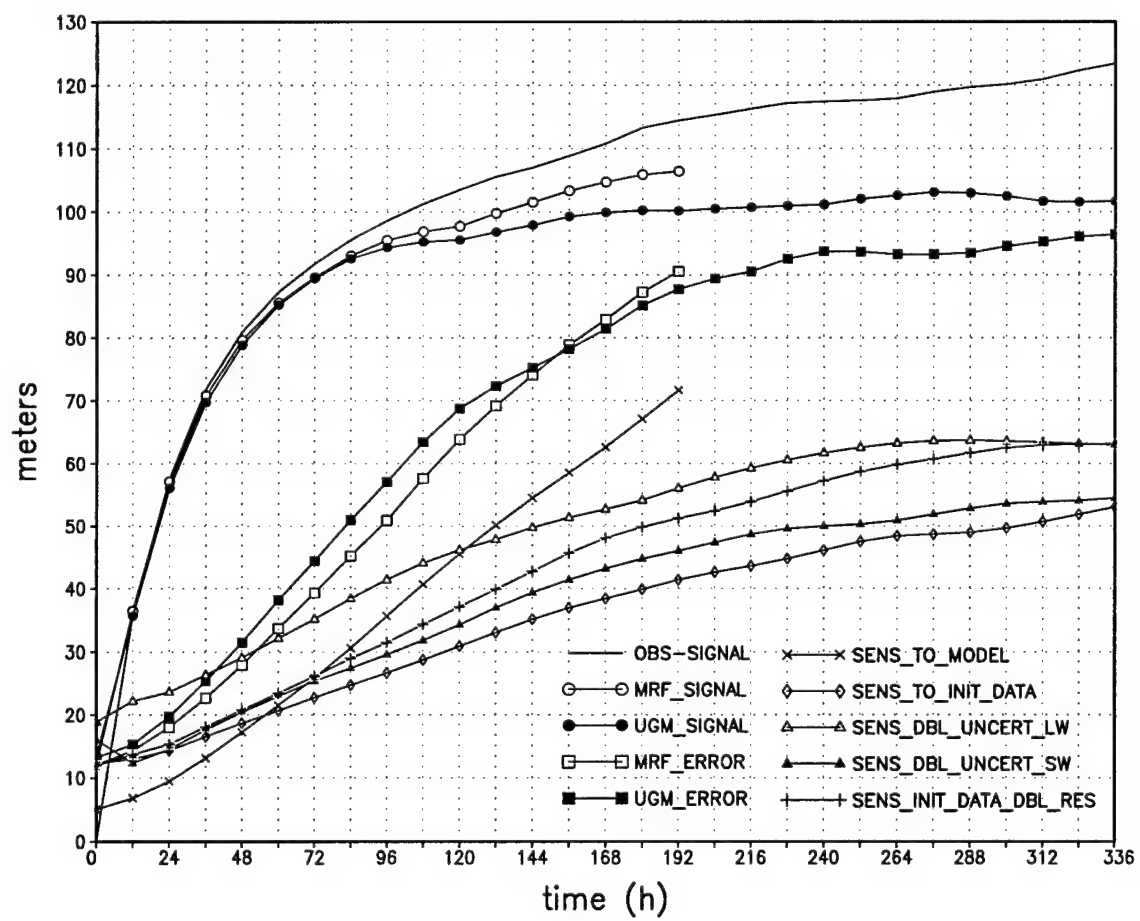
In order to address these issues, three other sets of experiments were conducted. In one, the initial state uncertainty estimated from the ECMWF - NCEP-NCAR forecast differences was retained only in wave groups 16-42, as in the earlier experiment sequence, but the amplitude of this difference field was arbitrarily doubled. A similar approach was taken by doubling the initial state uncertainty only in waves 0-15. Both experimental sequences were then repeated at low (wavenumber 42) resolution. A third experiment set was created by doubling the horizontal resolution in both latitude and longitude, and repeating the 17 forecasts for both the ECMWF and NCEP-NCAR initializations.

The results are summarized in Fig. 5.5, which is in the same format as Fig. 4.1a, and displays the relative contributions of various model/data configurations to the forecast discussed in Chapter 4. Each curve in Fig. 4.1a is repeated here, and three new curves are added: the sensitivity to the doubled initial uncertainty in waves 0-15 (open triangles), the sensitivity to the doubled initial uncertainty in waves 16-42 (closed triangles), and the sensitivity to the initial state for the doubled horizontal resolution (plus signs).

The most important change comes from doubling our prior estimate of uncertainty in waves 0-15. Doubling uncertainty in waves 16-42 is also important, but does not produce as much influence at longer forecast times as is found in modifications of the longer-wave group. Doubling the model resolution also enhances the error growth rates.

None of these experiments produces as much eight-day (192 h) forecast sensitivity to the initial state as the model selection (xs). As noted previously, the relative magnitude and

Fig. 5.5. Time evolution of global, case-averaged root-mean square 500-mb heights, for the 1993 cases. The top curve (solid) depicts the differences of the analyzed height at the time indicated on the abscissa minus the value at 0 hours. The second curve (open circles) depicts the differences of the MRF forecast height at the indicated time minus the analysis at 0 hours. The third curve (closed circles) depicts the differences of the UGM (initialized with NCEP) height at the indicated time minus the analysis at 0 hours. The fourth curve (open squares) depicts the rms error of the height field forecasted by the MRF. The fifth curve (closed squares) depicts the rms error of the height field forecasted by the UGM (initialized with NCEP). The sixth curve (xs) depicts the difference of the UGM (initialized with NCEP) forecast height minus the MRF forecast height, and measures the sensitivity of the forecasts to model used. The seventh curve (open triangles) depicts the NCEP-initialized UGM forecast difference due to doubled initial uncertainty in wavenumbers 0-15. The eighth curve (plus signs) depicts the difference of the high-resolution UGM forecast initialized with NCEP minus that of the high-resolution UGM initialized with ECMWF, and measures the sensitivity of the high-resolution forecasts to the initial dataset used. The ninth curve (closed triangles) depicts the NCEP-initialized UGM forecast difference due to doubled initial uncertainty in wavenumbers 16-42. The tenth and bottom curve (diamonds) depicts the difference of the low-resolution UGM forecast initialized with NCEP minus that of the low-resolution UGM initialized with ECMWF, and measures the sensitivity of the low-resolution forecasts to the initial dataset used.



structure of the errors of the MRF and Utah model appear to be similar through eight days, but their forecast differences are larger than the sensitivity to presently estimated measures of the initial state uncertainty. This conforms with the conclusion of Reynolds et al. (1994) for the Tropics, but conflicts with their findings for the extratropics. Sensitivity to initial state uncertainty may also be a function of model complexity and to be fair in the relative weighting of initial condition differences versus model differences, the initial condition sensitivity experiments should be done with a more complex, higher-resolution model.

CHAPTER 6

RESOLUTION ENHANCEMENT IN UGM

The UGM sensitivity to initial state uncertainty was shown to increase with resolution enhancement in the last chapter. The purposes of the present chapter are to first describe the sensitivity of UGM forecast accuracy to both model and initial state resolution, and second, to repeat at doubled horizontal resolution earlier experiments in which the initial state uncertainty was spectrally binned in short-wave and long-wave components.

Model

The higher-resolution UGM doubles east-west resolution to include 257 grid points. Fourier series depicting longitudinal variability are now truncated at wavenumber 84 to avoid aliasing instability, and in the north-south direction the number of model nodal points is increased from 82 to 164. The number and location of vertical levels is left unchanged with respect to the wavenumber 42 integrations. Ideally, resolution in all three dimensions should be at least doubled, but the presently enhanced resolution represents the largest model that could be executed for the required number of cases within the timeframe of the study. Even so, computer time limitations restricted the high resolution (wavenumber 84) experiments to a subset of cases reported in earlier sections. This subset includes 15 cases between 26 January and 24 February 2004.

Initial States

A series of experiments was performed using the NCAR-NCEP reanalyses as well as the GDAS analyses for the 15 selected cases. Enstrophy spectra for these two analyses are displayed in Fig. 6.1 for a particular day in the Northern Hemisphere winter 2002/03. Enstrophy is the square of the vorticity field, and its spectrum emphasizes shorter waves. The streamfunction is first computed globally from the wind field, and then projected onto spherical harmonics. Globally integrated enstrophy may be expressed as:

$$\int_A (\nabla^2 \Psi)^2 DA = \sum_{mn} (A_n^m)^2 [n(n+1)]^2 \quad (6.1)$$

where A is the global area, Ψ is the streamfunction, and A_n^m is the amplitude coefficient of the

spherical harmonic component of degree n and order m . The quantity $\left[\sum_m (A_n^m)^2 \right]^{1/2}$ is plotted

against global wavenumber n in Fig. 6.1, for 30 January 2003 at sigma level 0.3. The highest values are evident in the lowest wavenumbers, or in the longer waves of both analyses. The GDAS analysis (circles) clearly retains more amplitude in global wavenumbers on the order of, or exceeding 30, suggesting that it resolves much more of the subsynoptic structure than does the NCEP-NCAR reanalysis (solid).

Anomaly Correlations

A 15-case subset of experiments from boreal winter 2002/03 was repeated using the higher-resolution GDAS analyses to initialize the high-resolution (wavenumber 84) UGM, and results are compared to the MRF and the low-resolution (wavenumber 42) UGM anomaly correlations. Since this sample is too short to provide an adequate period for a priori bias removal,

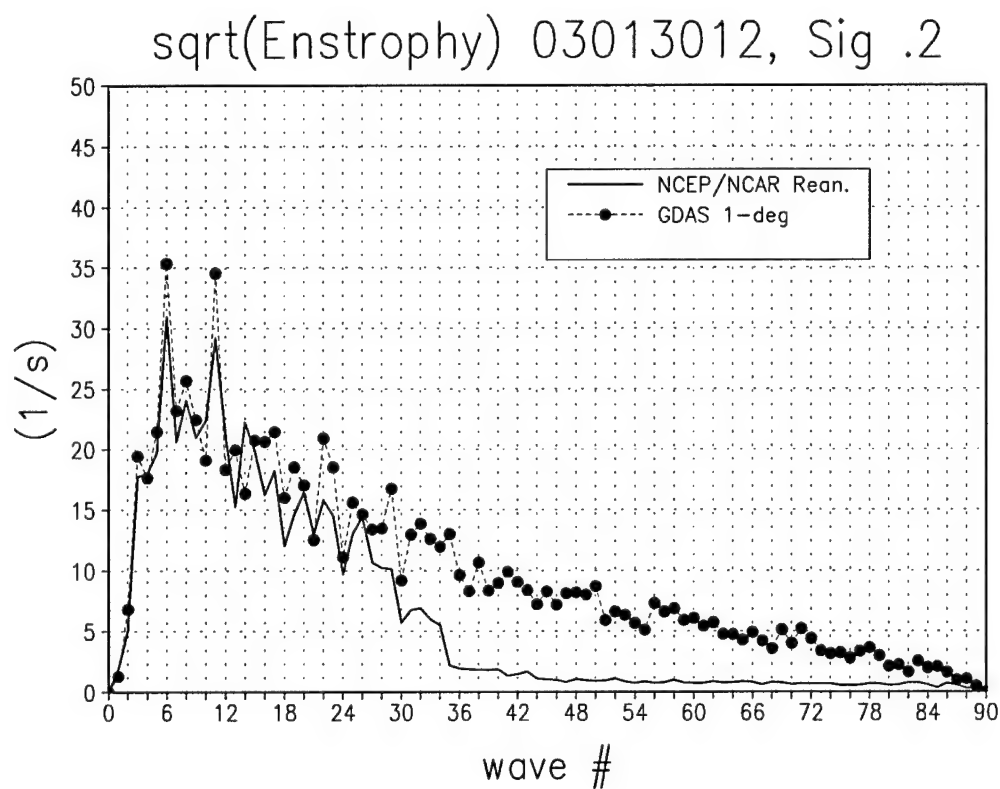


Fig. 6.1. The square root of the globally-averaged enstrophy spectrum as a function of wave-number, at 1200 UTC on 30 Jan 2003, for the NCEP-NCAR reanalysis (solid) and GDAS analysis (circles) at sigma level 0.2. Units are s^{-1} .

as was done in Chapter 3, the bias is removed from all model forecasts using the average error of the 15-case sample (a posteriori bias correction). This procedure does not allow a true measure of forecast accuracy, but may still be useful to determine how much relative benefit may be assigned to improved initial state analyses compared to model resolution enhancement.

Figure 6.2 displays the 500-mb height anomaly correlations obtained for the 15-case a posteriori bias-corrected MRF model forecasts for boreal winter 2002/03 (squares) and the a posteriori bias-corrected MRF forecasts obtained for the 17-case sample of 1993 MRF predictions (circles). Anomaly correlations of the 2003 MRF model dip to 0.6 after 204 h, while they drop to this amount approximately 48 h earlier for the 1993 cases. Note that the curve for 2003 anomaly correlations is different from that shown in Fig. 3.1 due to the different case sample size. The additional predictive skill for the 2003 MRF model shown in Fig 6.2 must be due to either better initial condition specification for the 15-case subset relative to the full 52-case sample, or the presence of large-scale atmospheric conditions better suited to predictability during the timeframe of the 15-case sample.

As suggested in Chapter 3, the overall MRF forecast enhancement from 1993 to 2003 may be due to a higher resolution model, to improved observations, or to a possibly more predictable situation in the 2003 cases. The latter explanation may be unlikely, because the amount of skill improvement (48 h) is more than might be expected from the episodic variability of skill suggested in Fig. 5.1 for the cases studied presently.

The relative roles of resolution enhancement and initial state enhancement can be better separated using the UGM. Figure 6.3 shows a posteriori bias-corrected anomaly correlations for 500-mb geopotential height for the 1993 low-resolution UGM runs (initialized with NCEP-NCAR reanalyses), and for the 2003 low- and high-resolution UGM runs (initialized with

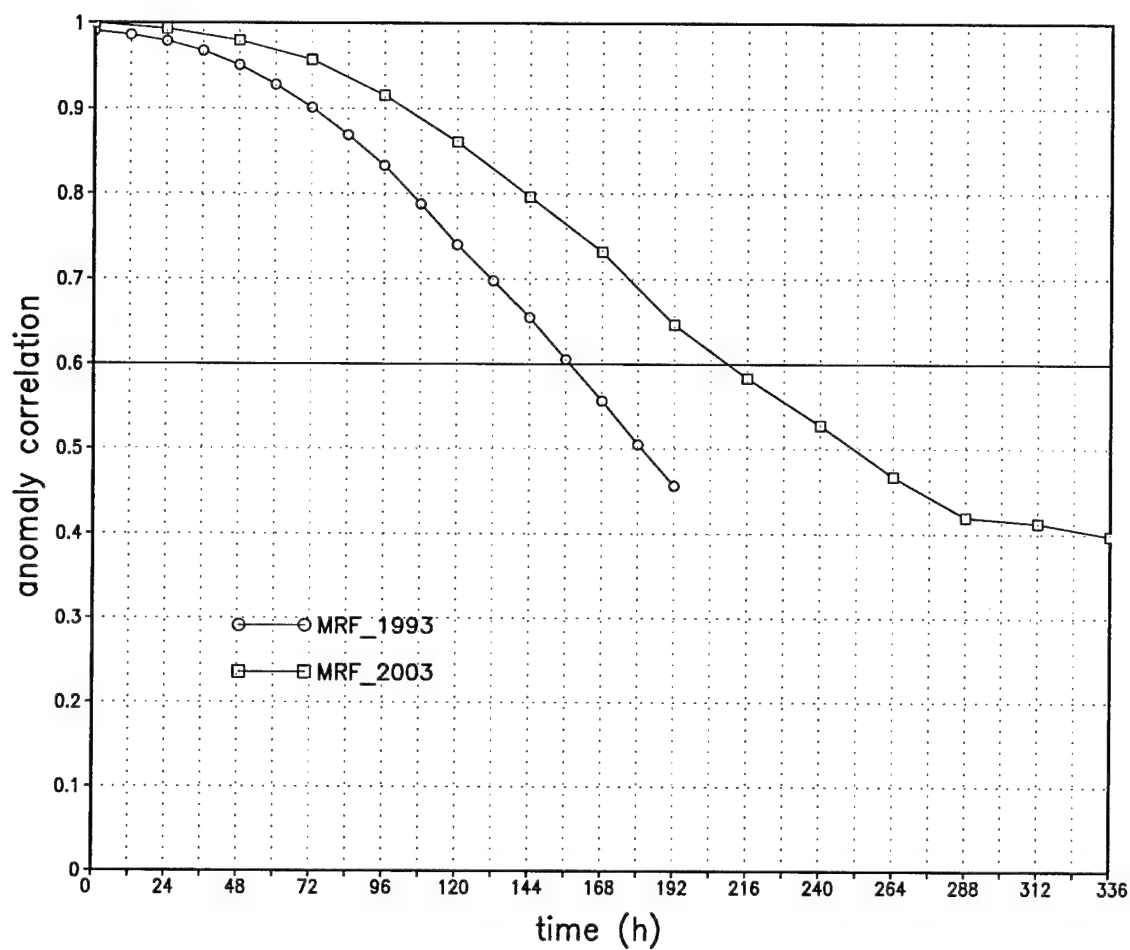


Fig. 6.2. Time evolution of global, case-averaged, bias-corrected anomaly correlations of the 500-mb geopotential height for the MRF, for the 1993 cases (circles) correlated with NCEP-NCAR reanalyses and 2003 cases (squares) correlated with GDAS analyses.

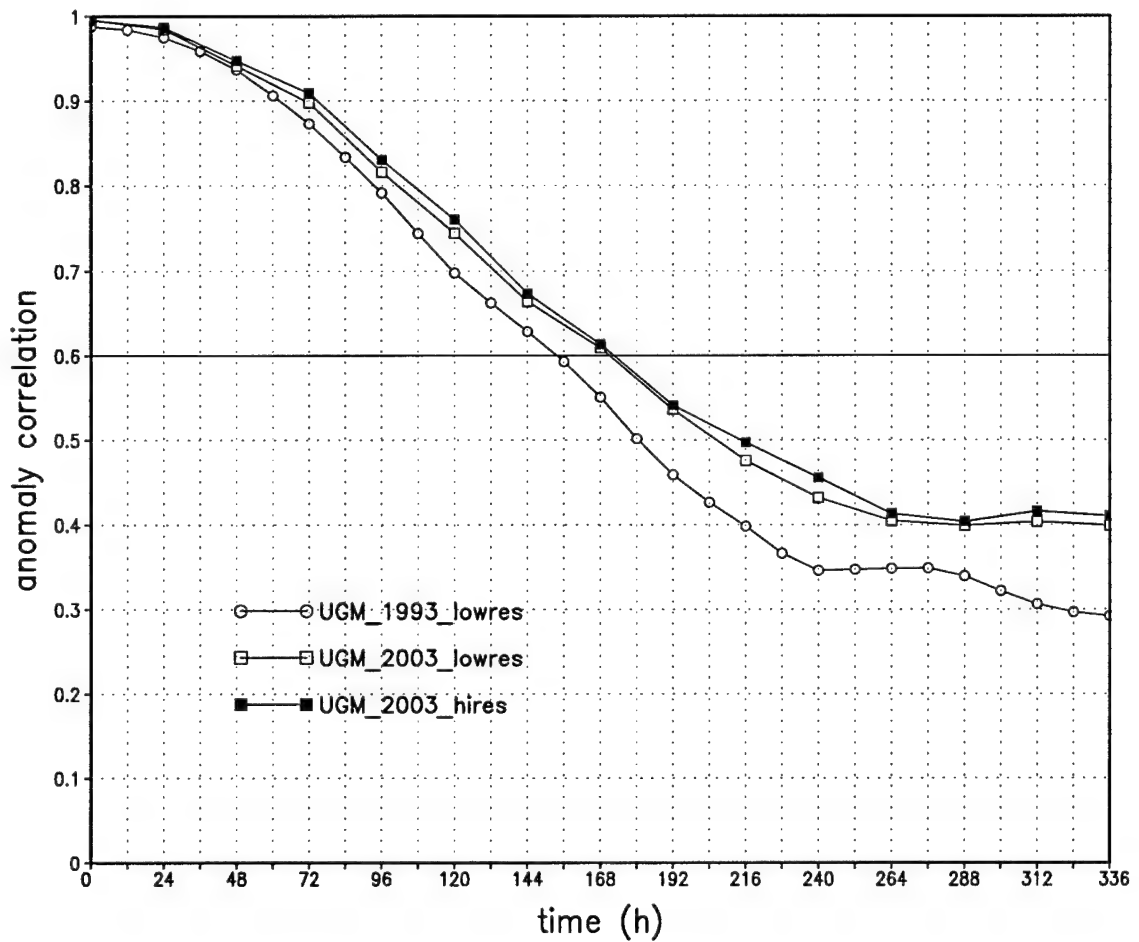


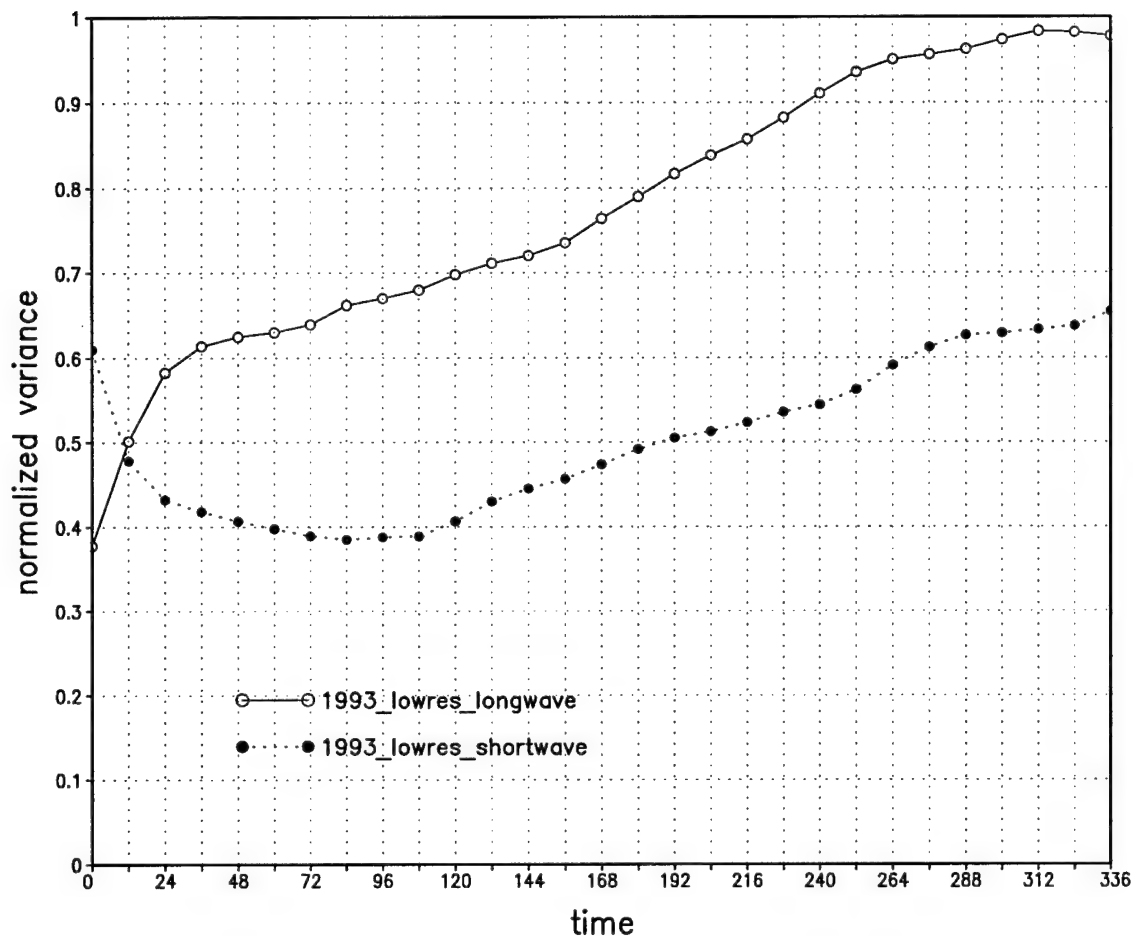
Fig. 6.3. Time evolution of global, case-averaged, bias-corrected anomaly correlations of the 500-mb geopotential height for the UGM, for the 1993 cases (circles) correlated with NCEP-NCAR reanalyses, and 2003 cases at wavenumber 42 resolution (open squares) and at wavenumber 84 resolution (closed squares), each correlated with GDAS analyses.

GDAS analyses). The UGM forecasts for the 17-case sample for 1993, executed at wavenumber 42 resolution (circles), produce anomaly correlations exceeding 0.6 for the first 154 h. UGM forecasts for the 15-case subset from boreal winter 2002/2003, run at the lower resolution (open squares), produce the same level of skill to approximately 170 h, and doubling model horizontal resolution (closed squares) for the 2003 cases extends the period of skillful forecasts by about another 3 h. Again, these values are different from those discussed in Chapter 3 due to the difference in low-resolution model sample size used for comparison with the limited number of high-resolution runs. Results for this smaller subset of cases suggest that enhancements in initial conditions from NCEP-NCAR reanalyses of 1993 to GDAS analyses of 2003 play a substantial role in predictive skill improvement over the past decade.

Spectral Binning of Initial State Uncertainty

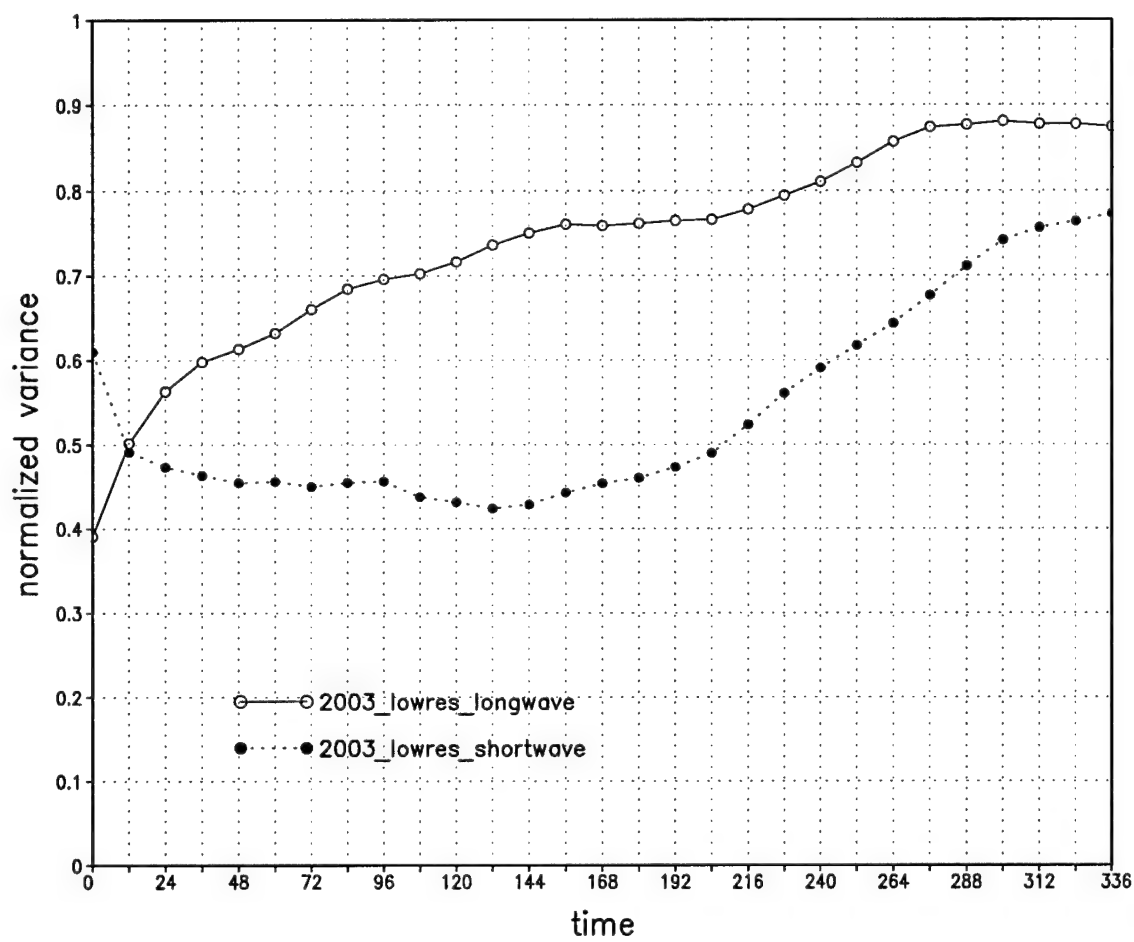
Initial state sensitivity experiments of Chapter 5 are now repeated using NCEP-NCAR reanalyses and the higher-resolution GDAS analyses as initial conditions for the wavenumber 84 UGM. In view of the computational expense of the wavenumber 84 model, the present section presents experiments in which the initial state uncertainty is retained only in waves 0-15, and in the complementary wavenumbers, 16-84, rather than all four spectral “bins” used for the low-resolution experiments.

The importance of higher resolution GDAS initialization to the wavenumber 42 UGM experiments is illustrated in Fig. 6.4, which shows the time evolution of $\sigma=0.53$ global variances of forecast meridional flow differences produced by initial data changes for the 1993 cases (Fig. 6.4a) and 2002/2003 cases (Fig. 6.4b). For comparison with 2003 results, Fig. 6.4a repeats the 1993 results displayed in Chapter 5, using initial analysis changes restricted in the complementary wave groups 0-15 (open circles) and 16-42 (closed circles), normalized by the



(a)

Fig. 6.4. Time evolution of normalized global variances at $\sigma=0.53$, of forecast meridional flow differences from the wavenumber 42 UGM, produced by initial data changes for global wave-numbers 0-15 (open circles) and for global wavenumbers 16-42 (closed circles). Initial data changes in (a) are from NCEP-NCAR to ECMWF reanalyses for the 1993 cases, and initial data changes in (b) are from NCEP-NCAR to GDAS analyses for the 2003 cases.



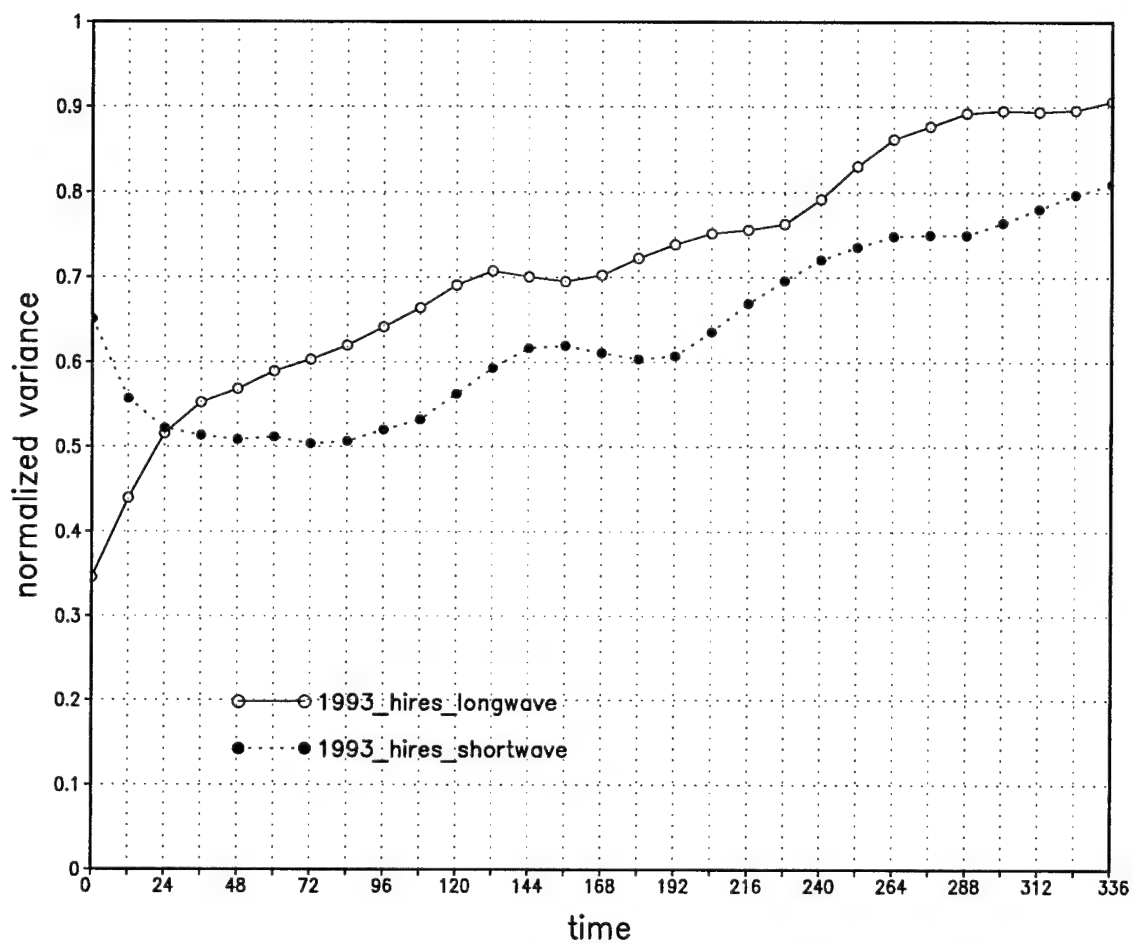
(b)

Fig. 6.4. (continued)

effect of changing the initial analysis in the completely resolved spectrum. Recall that the 1993 cases utilized NCEP-NCAR and ECMWF reanalyses. Fig. 6.4a demonstrates that the initial state meridional flow uncertainty is dominated by short waves, wavenumbers 16-42, but that the uncertainty of the longer waves, wavenumbers 0-15, becomes more important after 12 h, and remains more important for the 14-day (336 h) duration of the experiment. This is consistent with the findings of MMP.

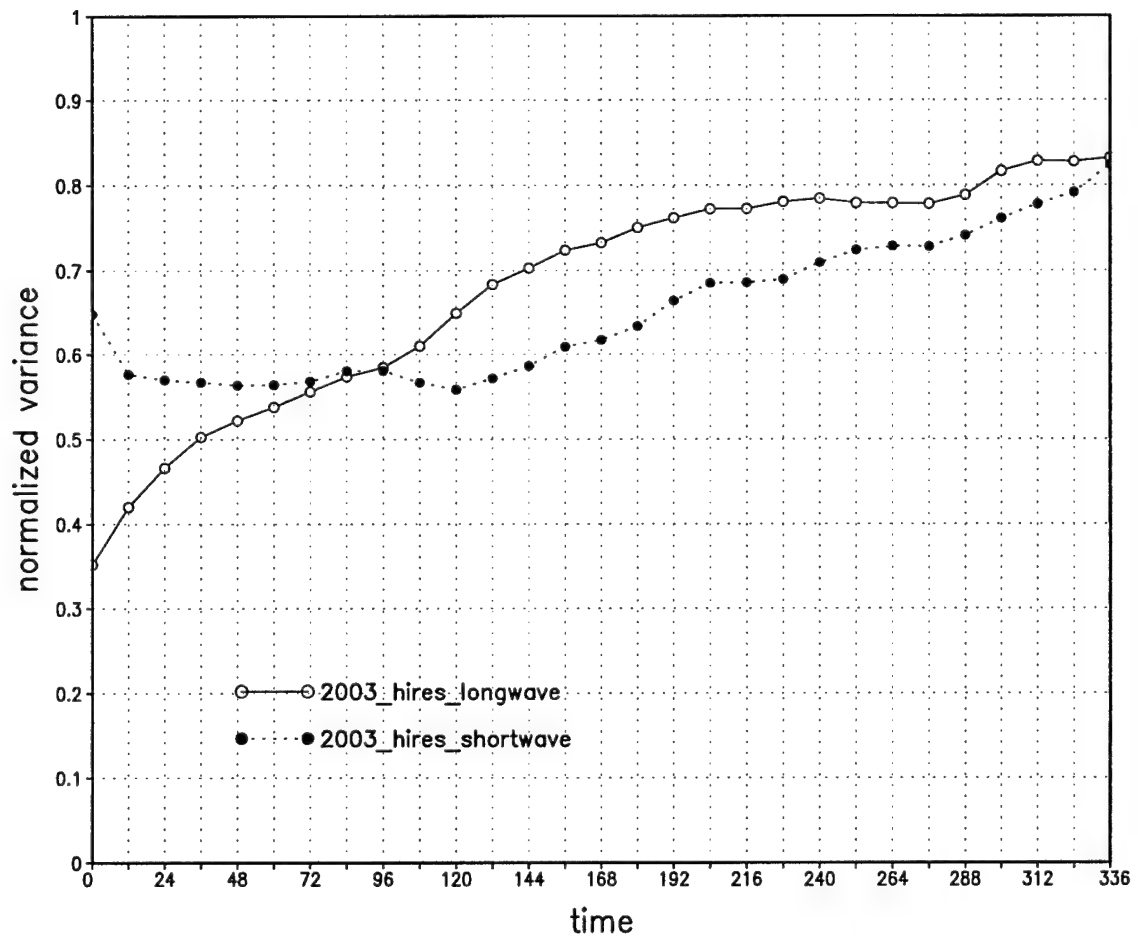
Figure 6.4b is based on the same model configuration (UGM, wavenumber 42), but presents results using the difference of NCEP-NCAR reanalyses with GDAS analyses for boreal winter 2002/03 to calculate the initial state uncertainty. The conclusions are rather similar to those of the 1993 cases shown in Fig. 6.4a, with the uncertainty of the longer waves becoming more important after 12 h, but the relative importance of short wave uncertainty begins to approach that of the longer waves towards the end of the 14-day forecast period.

Figure 6.5 shows the evolution of normalized global variances at $\sigma=0.53$ of forecast meridional flow differences produced by initial data changes for the high-resolution research model for 1993 and 2003 cases. Figure 6.5a is based on the 17-case sample of 1993 experiments that are identical to those in Fig. 6.4a, but the results are based on the wavenumber 84 UGM. An important modification of the results due to the increased model resolution in Fig 6.5a is that the short-wave uncertainty impact exceeds the long-wave impact for the first 24 h, compared with 12 h in Fig 6.4a, and although the role of long-wave uncertainty is most important after this in the wavenumber 84 experiments, it is not as dominant as in the wavenumber 42 experiments. Figure 6.5b, which repeats the 2002/03 experiments of Fig 6.4b but with wavenumber 84 model resolution, suggests that the influence of the shorter wave detail available in GDAS analyses is more important than longer wave detail for the first three days



(a)

Fig. 6.5. Time evolution of normalized global variances at $\sigma=0.53$, of forecast meridional flow differences from the wavenumber 84 UGM, produced by initial data changes for global wavenumbers 0-15 (open circles) and for global wavenumbers 16-84 (closed circles). Initial data changes in (a) are from NCEP-NCAR to ECMWF reanalyses for the 1993 cases, and initial data changes in (b) are from NCEP-NCAR to GDAS analyses for the 2003 cases.



(b)

Fig. 6.5. (continued)

of prediction, and the longer wave uncertainty is more important after this time, but only by a relatively small amount.

The high-resolution experiments indicate that the UGM executed at wavenumber 84, incorporating added detail available from the GDAS analyses, displays significantly more forecast sensitivity to smaller scales of the initial state, particularly in the first three days of prediction, but that error evolution is slightly more sensitive to uncertainties in the larger scales for medium- and long-range prediction. These results modify those suggested by MMP and by experiments described in Chapter 5.

Recent work reported by Tribbia and Baumhefner (2004) also highlights the need for continued research into the relationship between uncertainty scale and error growth. Their investigations of scale interactions and short-term predictability with the NCAR Community Climate Model Version 3 showed that error growth was not described by an inverse cascade, but that initial state uncertainty in the synoptic scales (wavenumbers 10-20) was most important for growth of errors. Although Tribbia and Baumhefner's experiments used a highly sophisticated climate model run at higher resolutions than the UGM, qualitatively the results match those reported here, and point to the importance of detailed broad spectrum analyses for global weather prediction.

CHAPTER 7

EULER MODEL

Virtually all global models that have been applied for long periods to real-time prediction or to climate simulations are based upon the primitive equations. These equations filter out sound waves and make the hydrostatic approximation. Such approximations are not made in so-called "Euler models" that are being developed experimentally in a number of limited area applications as well as in global versions (e.g., Semazzi et al. 1995; Dudhia and Bresch 2002). Although some comparisons have been made of results using the Euler equations relative to those produced by the primitive equations in case studies, systematic intercomparison of a series of forecasts by these different dynamical model cores has not yet been publicized. The present chapter describes the development of an Euler model that will be used in Chapter 8 to describe sensitivity to model dynamical core.

The Euler model used in present testing is relatively new, and has not been previously documented. Equations for the model dynamics are presented in Appendix A. Since the model physics is identical to that used in the UGM, and is documented elsewhere (e.g., Nicolini et al. 1993), its description is not repeated here.

Most global primitive equation models incorporate dynamical cores that predict vorticity, divergence, and temperature, and diagnose vertical motion and geopotential height (i.e., the mass distribution). Vorticity and divergence, rather than wind components, are predicted because the former variables are scalar quantities more suited for expansion in terms of spheri-

cal harmonics. Such expansions allow accurate “spectral” methods to be used in the approximation of horizontal derivatives. Spectral methods, in principle, compute horizontal derivatives without any truncation error, aside from the error which is implicit in the truncated representation of the expansion. The UGM applies spectral approximations to longitude derivatives and finite element approximations to latitude derivatives, while the MRF (GFS) uses spherical harmonic expansion for all variables involved in its dynamical core.

By contrast, most Euler models use dynamical cores that predict the horizontal wind components, u and v , as well as vertical velocity, w , the temperature or potential temperature, and the pressure or density fields (i.e., the mass distribution). The present Euler model predicts u , v , w , potential temperature, and pressure, as outlined in Appendix A. Since vector fields are not well-suited for expansion in spherical harmonics, Euler models typically use grid point, finite difference methods that retain some truncation error, even for resolved structures.

The present Euler model uses the “b-grid” described in Appendix A. This is similar to the approach of Dudhia and Bresch (2002), but differs from most other global Euler models, which use the “c-grid” (e.g., Semazzi et al. 1995). As pointed out by Dudhia (1993), the “b-grid” requires more horizontal averaging to calculate advection terms, but its use allows a larger time step than does the “c-grid” for a given horizontal grid size.

The version of the Euler model used in this study uses a spherical grid and finite element approximations for all flux terms in the horizontal and vertical directions. This approach is, in theory, more accurate than most other second- or fourth-order schemes, and expansion of nonlinear transports in terms of their finite element projections on piecewise linear functions guarantees conservation of certain one-dimensional quadratic norms. This may make the method more stable than some other finite difference methods that do not impose formal con-

servation constraints on second-order moments, and, therefore, do not contain built-in constraints to eliminate nonlinear aliasing instabilities in nonlinear advection terms.

For present grid sizes, there is no formal reason to expect substantially different forecasts in the Euler model than in the UGM, because effects of vertical acceleration and of compressibility are unimportant for the resolved scales. Some differences may be expected in individual forecasts at longer lead times because of the different paths along which chaotic components of the flow may evolve, but there is little reason to anticipate systematically different behaviors between the UGM and an Euler model executed at similar precision. Nevertheless, some systematic differences do emerge, as will be seen in subsequent sections. The following discussion outlines some inherent model differences that may help to explain differing results. There are three likely explanations: the Euler model and the UGM use different vertical resolution, initialization, and turbulent diffusion.

The Euler model requires about 30 above-ground vertical levels to produce stable two-week solutions, while the UGM can be run with fewer levels, using only 20 above-ground levels in present experiments. The Euler model treats vertical sound wave propagation implicitly, and slows down vertical sound wave propagation in the process. The resolution required for this process appears to demand a more detailed vertical treatment than needed in hydrostatic models such as the UGM, which filter vertically-propagating sound waves explicitly in the dynamical formulation.

Although higher vertical resolution places a greater computational burden on the Euler model than on the UGM, it also produces better resolution of vertical atmospheric variation for depiction of vertical wind shear, stratification, and vertical propagation of resolved phenomena. This extra vertical resolution should favor the Euler model in forecast accuracy, particu-

larly in the stratosphere, as outlined below.

It is also possible that the location of the levels makes a difference in forecast outcome, although this has not been demonstrated in the present study. The UGM uses a sigma coordinate in the vertical, with levels situated at $\sigma=0.99, 0.98, 0.96, 0.94, 0.91, 0.88, 0.84, 0.78, 0.72, 0.66, 0.59, 0.53, 0.47, 0.41, 0.34, 0.28, 0.22, 0.16, 0.09$, and 0.03 . The Euler model uses a height-based coordinate that carries information at the following levels (above oceans): $z=0, 100, 500, 1000, 2000, 3000, 4000, 5000, 6000, 7000, 8000, 9000, 10000, 11000, 12000, 13000, 14000, 15000, 16000, 17000, 18000, 19000, 20000, 21000, 22000, 23000, 24000, 26000, 28000$, and 30000 meters. The UGM devotes more levels (about six) to the atmospheric boundary layer, while the Euler model only carries three levels in the lowest kilometer. The UGM carries about 16 levels in the troposphere, and only about four levels in the stratosphere, while the Euler model carries a similar number of levels in the troposphere but has about 10 more levels than does the UGM in the stratosphere.

The second inherent difference between the UGM and Euler model which may explain inconsistencies in forecasts from the two models is model initialization. The UGM is initialized through a high-accuracy global interpolation scheme in which all variables available from the GDAS or reanalysis archive are first interpolated onto the UGM grid using spherical harmonic representation. This process is more consistent with the way dynamical variables are structured in the UGM, and the high-order interpolation procedure produces superior forecasts compared to simple linear interpolation from the GDAS or reanalysis grid to the UGM grid (preliminary results indicate the high-order interpolation provides a 6 h improvement in predictive skill over simple linear interpolation). The current version of the Euler model simply uses low-order, local linear interpolation to obtain the initial state, so initialization procedures

should favor the UGM.

The final difference between the UGM and Euler model to which dissimilarities in resulting forecasts may be attributed is the treatment of turbulent diffusion. The horizontal diffusion in the UGM is treated analytically in Fourier space on individual latitude circles. This allows implicit time-differencing for diffusion, but makes it difficult to specify diffusion in a way that depends locally upon predicted gradients. Consequently, the horizontal diffusion is simply proportional to the horizontal grid size. For the UGM model, the horizontal diffusivity for vorticity, temperature, and moisture prediction is $10^5 \text{ m}^2 \text{ s}^{-1}$, and diffusivity for divergence prediction is two orders of magnitude larger. The large divergence diffusivity is required because of the time splitting technique used to treat gravity waves separately from advective and Rossby wave dynamics. The time splitting provides much time savings in the calculation, and produces UGM predictions in about one-fifth the time required for Euler model predictions, but it typically requires added diffusion in the divergence prediction.

In contrast, the Euler model imposes horizontal diffusivity that is locally proportional to the wind field gradients, multiplied by the square of the grid size. The maximum value is constrained to be less than $1.6 \times 10^4 \text{ m}^2 \text{ s}^{-1}$ in present applications. An even smaller limit is imposed on moisture diffusion and thermal diffusion. The results of the model are almost independent of the value of diffusion in this range, signifying that the Euler solutions are very slightly affected by arbitrarily imposed mixing coefficients.

The selection of horizontal diffusion probably favors the Euler model relative to the UGM. The small values of diffusivity in the Euler model allow stronger gradients of moisture and stronger moisture convergence in Euler simulations than in UGM simulations. The result is different precipitation distributions, which are more realistic in their areal coverage than are

those for the UGM. Such differences in precipitation patterns imply differences in cloud coverage between the two models, with related differences in the models' radiation balances.

It is possible that some of the systematic forecast differences that are found between the Euler model and the UGM are due to these different precipitation and latent heating rates, partially explained by the different amounts of diffusive mixing. In view of the computational expense of the Euler model experiments, it was not possible to separate the effects of these different model characteristics in a set of controlled experiments. If the forecast differences are indeed produced by differences in rainfall rates associated with disparate treatments of model diffusivities, it would be appropriate to characterize them to be due to both dynamical core differences as well as physical processes. More work is required to determine the true source of forecast differences. The goal of the following results is merely to point out the degree of forecast divergence found in a systematic one-month intercomparison.

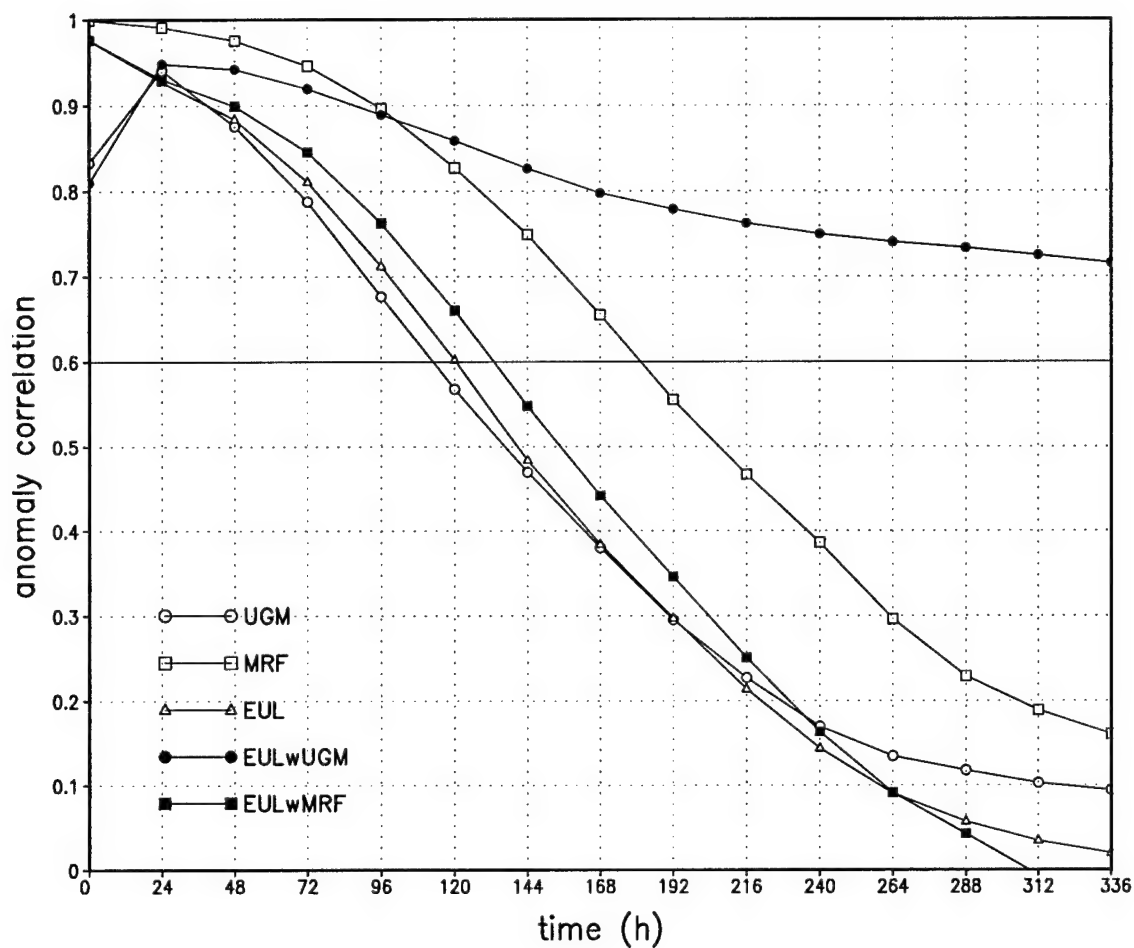
CHAPTER 8

EULER CORRELATIONS AND BIAS

Comparison of UGM and MRF statistics in previous chapters implied a correlation of error patterns and biases between the models, despite various differences in model configuration and resolution. To further investigate the implication of a common limitation to predictive skill in forecast models, a 30-case sample of Euler model forecasts for boreal winter 2002/03 is examined with respect to results shown in Chapter 3.

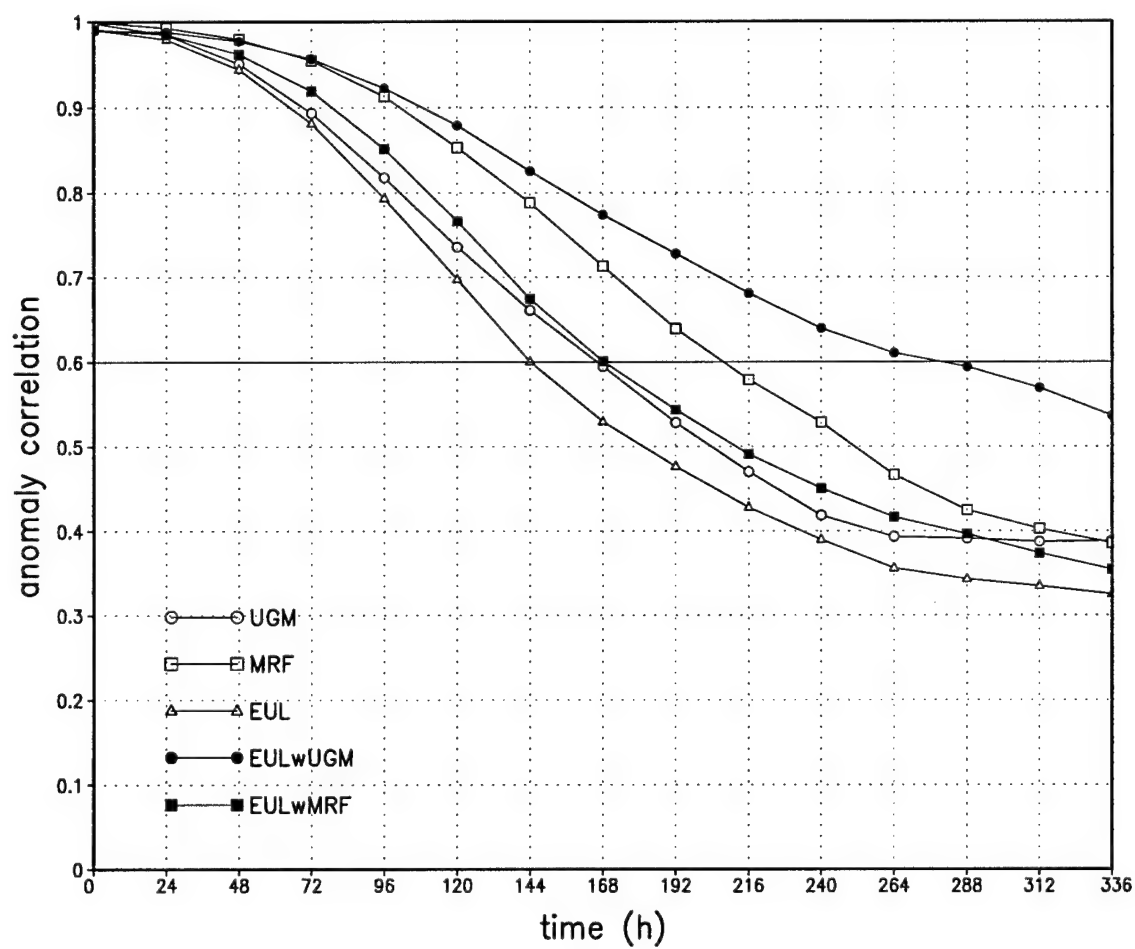
Figure 8.1 shows case-averaged, globally-averaged, 500-mb geopotential height anomaly correlations for the various models without (Fig 8.1a) and with (Fig 8.1b) an a posteriori bias correction. All curves shown are averages for the 30-cases prior to 26 February 2003. Figure 8.1a indicates that the Euler model (triangles) has approximately 6 h more predictive skill than the UGM (circles) during the first five days (120 h), and is more similar to the evolution of the MRF (closed squares) than the real atmosphere. Due to the similarities between the UGM and Euler model (same model physics and resolution), their model-to-model correlation is very high, and does not drop below 0.6 throughout the 14-day (336 h) forecast.

Because the Euler model is computationally expensive, the completion of a “training period” of cases used for an a priori bias correction was not possible. Bias corrections are, therefore, a posteriori, which does not allow a true measure of forecast accuracy, but is useful to determine relative accuracies between the models. Figure 8.1b shows the bias-corrected results for the anomaly correlations shown in Fig. 8.1a. The Euler model clearly does not ben-



(a)

Fig. 8.1. Time evolution of global, case-averaged anomaly correlations of the 500-mb geopotential height, for the 2003 cases of the UGM (open circles), MRF (open squares), and Euler model (triangles), each correlated with analyses; and for the Euler model correlated with the UGM (closed circles) and the Euler model correlated with the MRF (closed squares). Correlations are (a) not bias corrected and (b) a posteriori bias corrected.



(b)

Fig. 8.1. (continued)

efit as much from the bias correction as does the UGM. Euler model predictive skill (triangles) now lags that of the UGM (circles) by 24 h, and the bias-corrected Euler model is less able to forecast the bias-corrected UGM (closed circles) than in the uncorrected case (model-to-model anomaly correlations now drop below 0.6 at approximately 288 h).

This drop in model-to-model anomaly correlations after bias removal implies a similarity in bias fields between the UGM and Euler model. Figure 8.2 shows the 500-mb meridional wind bias field and departures from zonal mean height field at forecast hour 336 for the Euler model, for the same 30-day period used for the UGM and MRF fields in Chapter 3. Once again, remarkable similarities in the bias fields (Fig. 8.2a and Fig. 3.3a,b) are seen, although there are some differences, particularly centered over Japan, the Great Lakes, and between the southern extents of South America and Africa. Comparison of the departures from the zonal mean forecasted geopotential height for the three models (Fig. 8.2b and Fig. 3.5a,b) again shows a stronger similarity between model forecasts than between any of the models and the analysis for the same period (Fig. 3.4b). The Euler model, like the UGM and MRF, places a ridge over the northern Rockies rather than off the Pacific coast of the United States, and the Euler model also misses the blocking pattern evident over central Europe in the analysis.

To quantify the similarities in model bias and investigate the differences between Euler-to-UGM and Euler-to-MRF correlations, Fig. 8.3 displays the correlations coefficients of the error of the 500-mb meridional flow forecast by the Euler model correlated with the error of the same variable forecast by the MRF (Fig. 8.3a) and UGM (Fig. 8.3b). Comparing Fig. 8.3a with Fig. 3.6a shows that the UGM and Euler model error fields are very similar since correlations of both with the MRF result in nearly identical curves. In each case, correlations of errors continue to rise throughout the 14-day (336 h) forecasts despite initial data uncertainties and

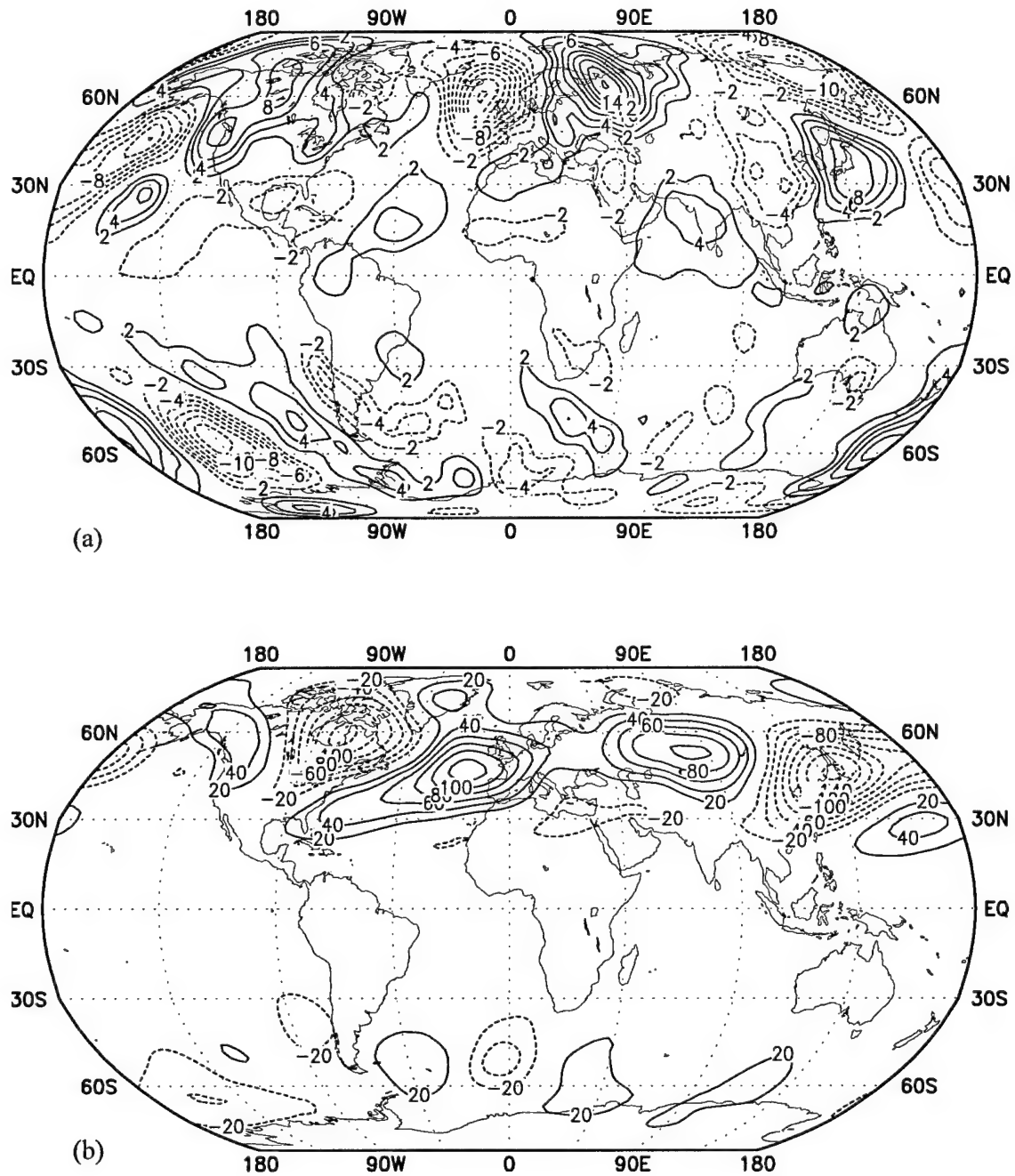
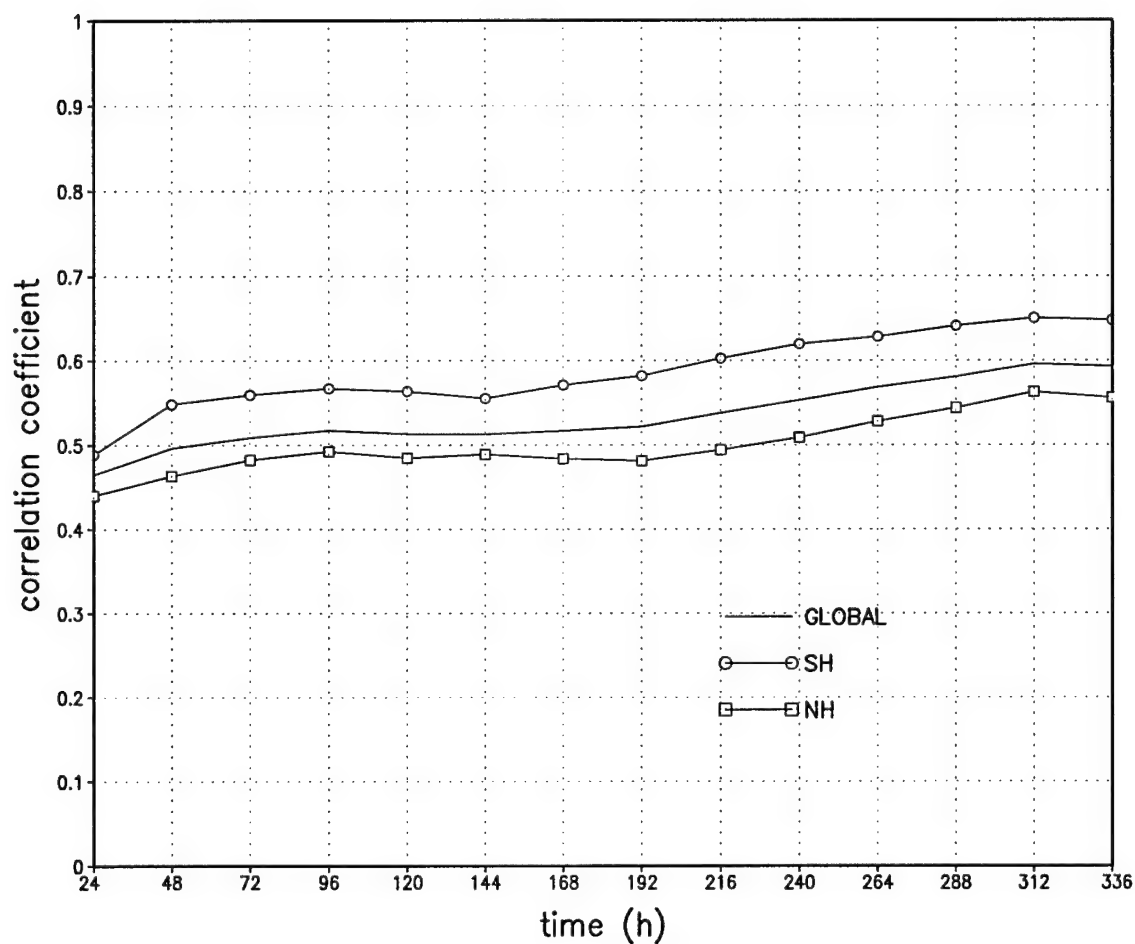
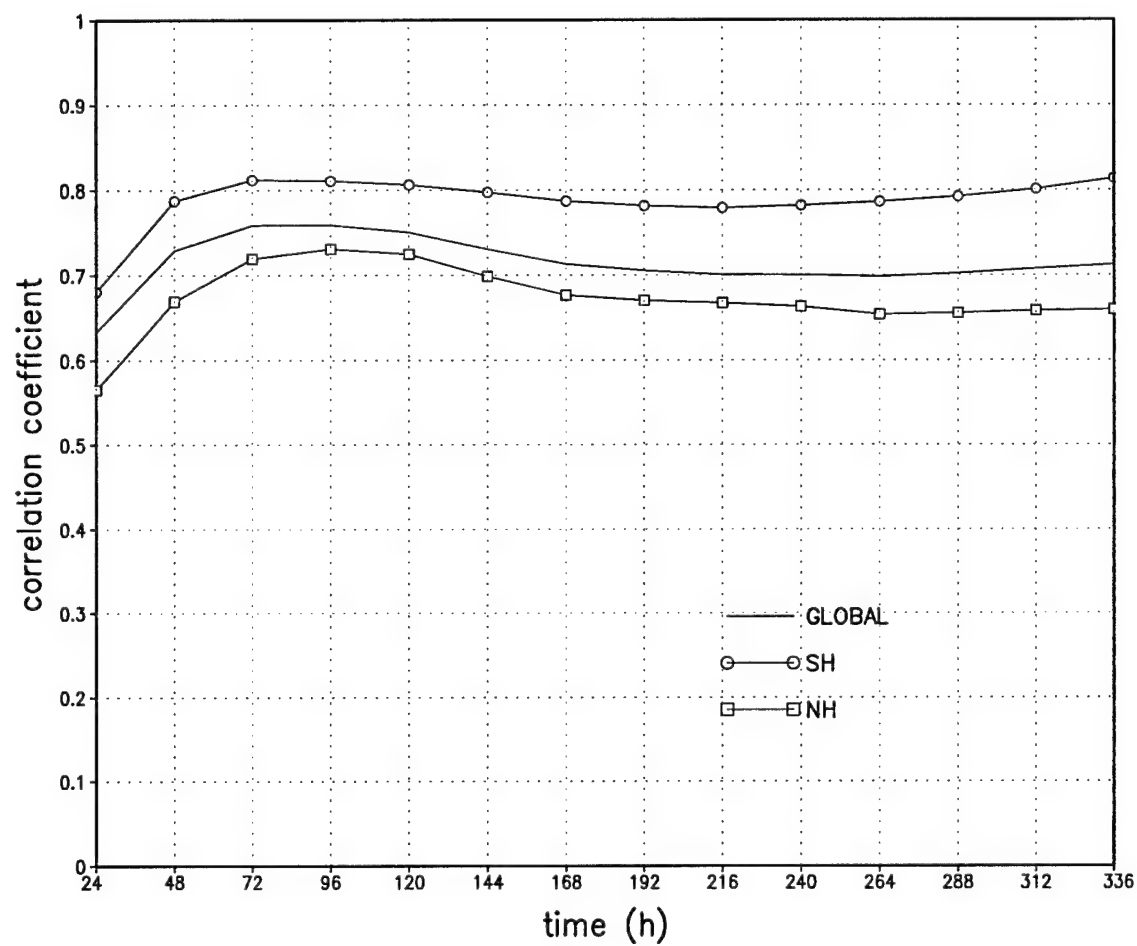


Fig. 8.2. Euler model bias and forecast fields at forecast hour 336, averaged over 30 model runs prior to 26 Feb 2003. Contours in (a) depict 500-mb meridional wind bias fields and contours in (b) depict departures from zonal mean 500-mb height field. Contour interval is 2 m s^{-1} in (a) and 20 m in (b).



(a)

Fig. 8.3. Time evolution of case-averaged correlation coefficients (not bias corrected) of the 500-mb meridional wind error for 30 days preceding 26 Feb 2003, averaged globally (solid), averaged over the latitude band 90° - 20° S (open circles), and averaged over the latitude band 20° - 90° N (open squares). Correlations are for the Euler model to the (a) MRF and (b) UGM.



(b)

Fig. 8.3. (continued)

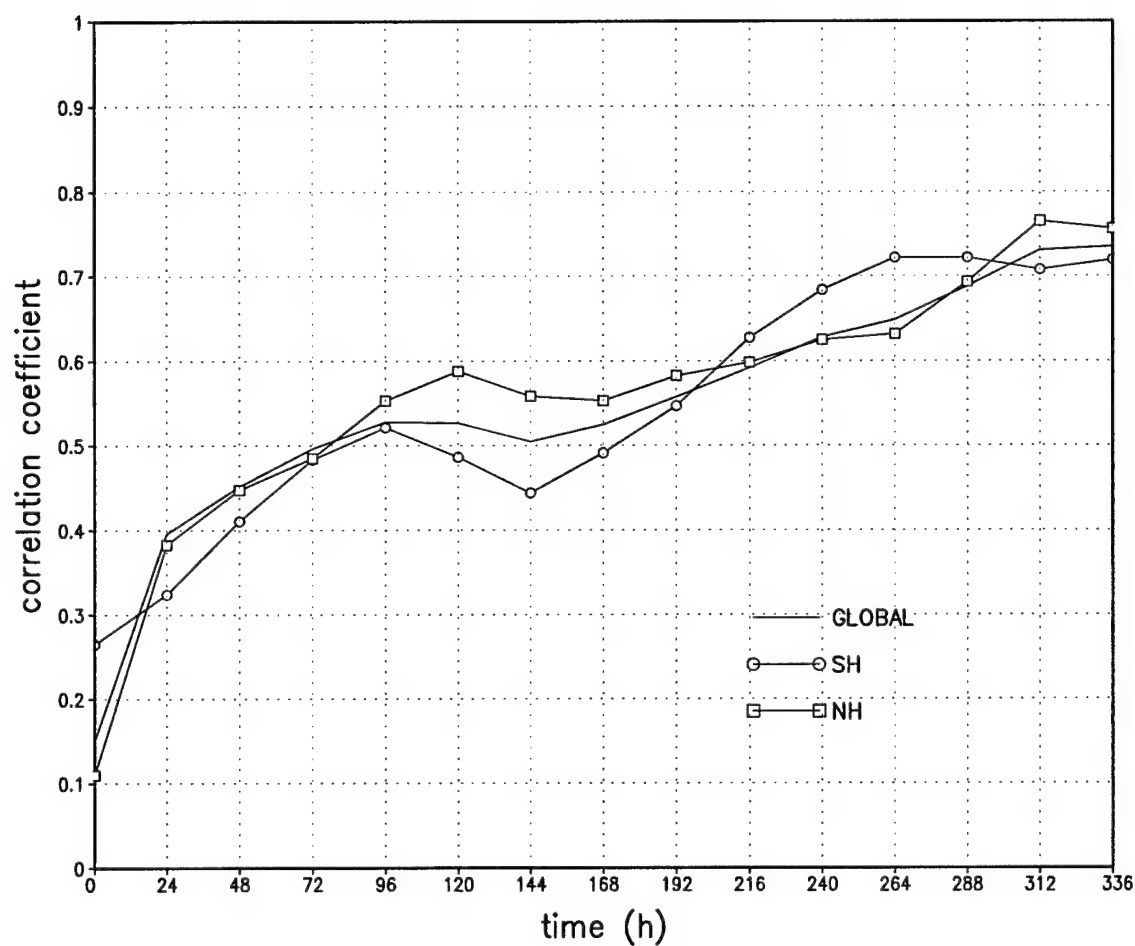
growing model chaos. As indicated in Chapter 3, this points to the growing similarities in model bias between the UGM/Euler model and the MRF.

Figure 8.3b reflects correlations of the Euler model with the UGM. The rapid rise in correlations during the first 48 h of the forecasts may be attributed to uncertainties in the initial conditions, which were the same for both models. Past this point, the correlations tend to flatten at high values, hinting that the similarity in bias between the UGM and Euler model is sustained throughout the 14-day integrations.

The conclusions regarding similarity in model bias are quantified in Fig. 8.4 which shows the correlation coefficients of the bias of the 500-mb meridional flow forecast by the Euler model with that forecasted by the MRF (Fig. 8.4a) and the UGM (Fig 8.4b). Comparison of Fig 8.4a (Euler to MRF correlations) with Fig. 3.6b (UGM to MRF correlations) indicates, again, that the Euler/UGM model biases continue to grow in similarity with the MRF bias throughout the forecast, and are most similar by day 14.

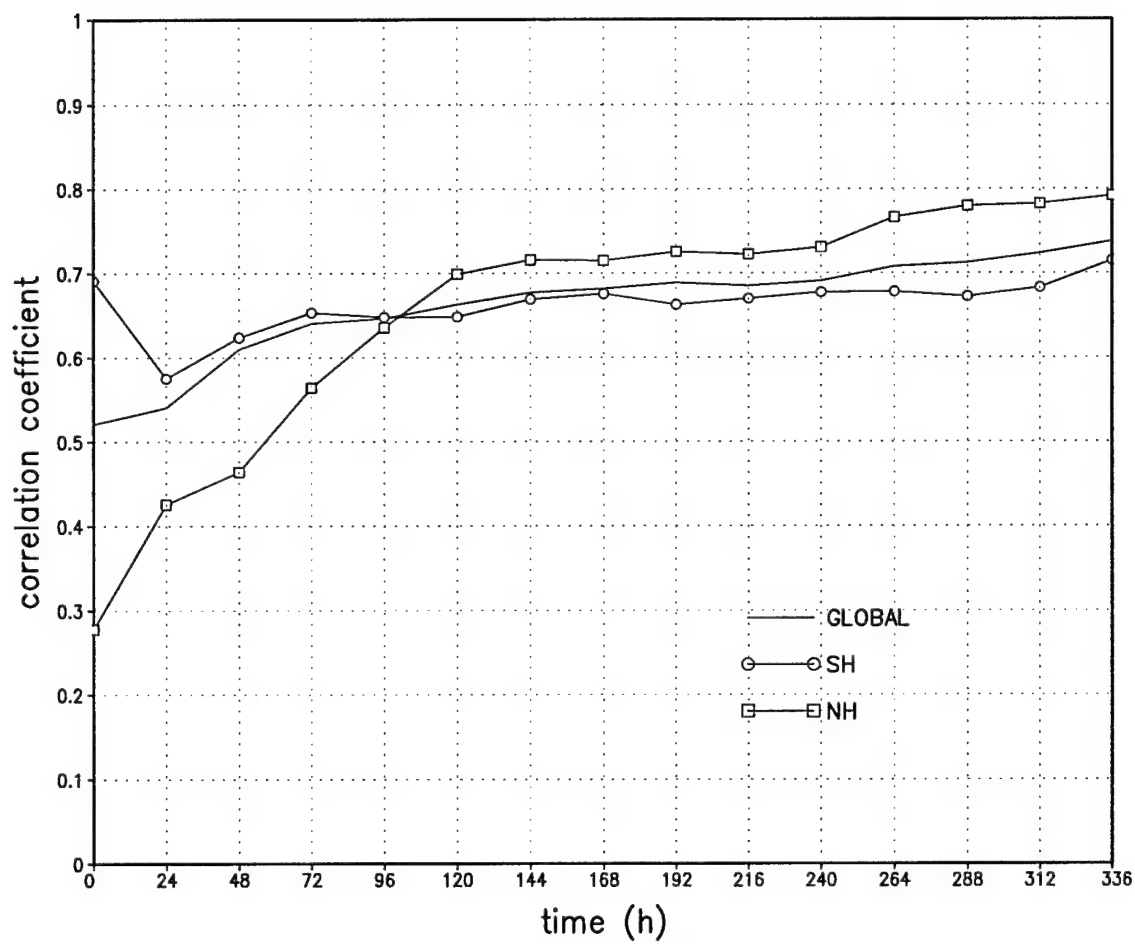
Figure 8.4b shows the Euler model bias correlations with the UGM bias. Although the model biases are most similar in the Southern Hemisphere early in the forecast, by day 5 (120 h) the model biases are highly correlated throughout the globe and continue to remain correlated during through the end of the forecast period.

The similarity of error between the three models continues to point to some fundamental limitation of forecast accuracy. Initial state uncertainty is common to all models, and may explain the agreement in error and bias behavior early in the integration period, but it is still unclear to what the subsequently growing similarities in bias structure between the three different models may be attributed.



(a)

Fig. 8.4. Time evolution of the correlation coefficients of the 500-mb meridional wind bias, computed over the 30 days preceding 26 Feb 2003, averaged globally (solid), averaged over the latitude band 90° - 20° S (open circles), and averaged over the latitude band 20° - 90° N (open squares). Correlations are for the Euler model to the (a) MRF and (b) UGM



(b)

Fig. 8.4. (continued)

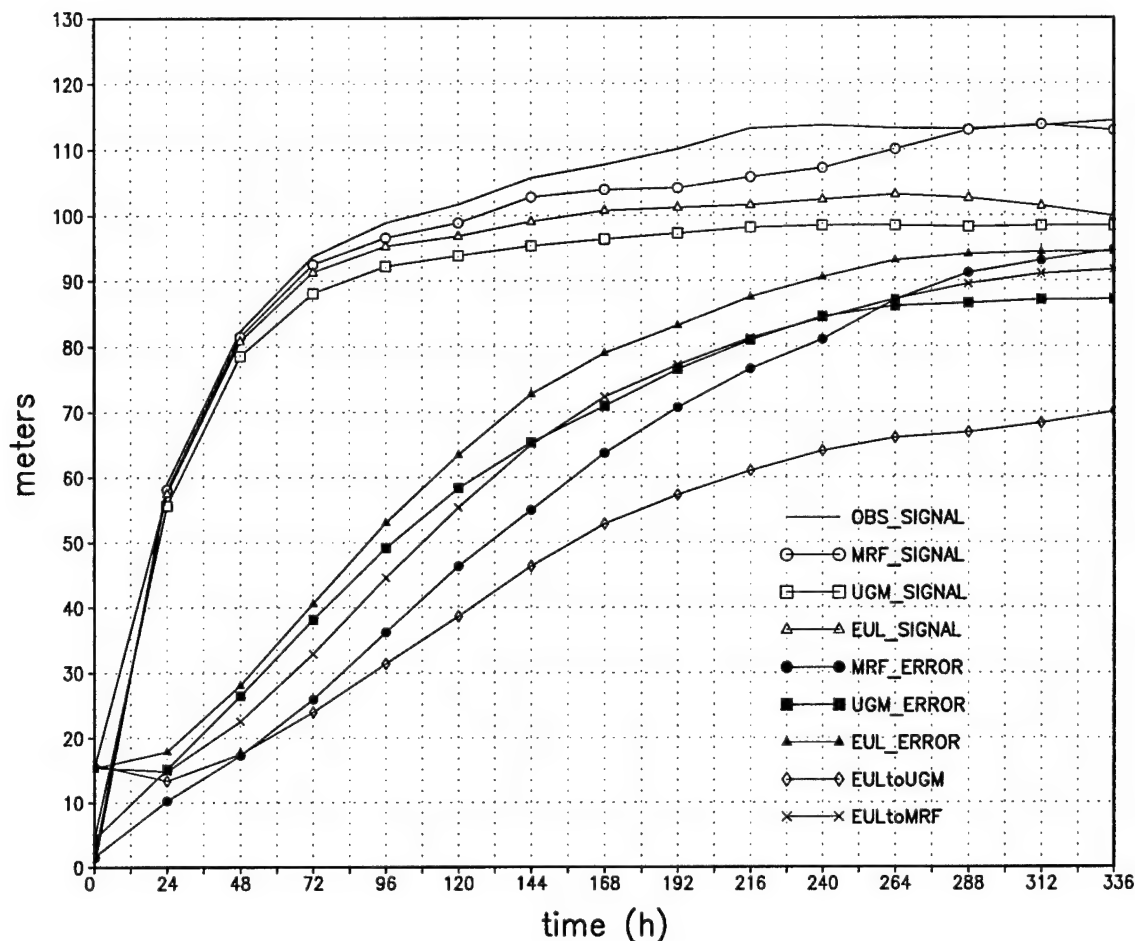
CHAPTER 9

EULER ROOT-MEAN-SQUARE AND FORECAST EVOLUTION

As indicated in Chapter 7, the forecast evolution of the UGM and Euler models is expected to be similar, and bias and error field correlations in Chapter 8 showed this to be the case. However, Chapter 7 also described at least three differences in Euler and UGM model formulation that may lead to systematic differences between the models. The purpose of this chapter is to further investigate these differences through global rms values, as described in Chapter 4.

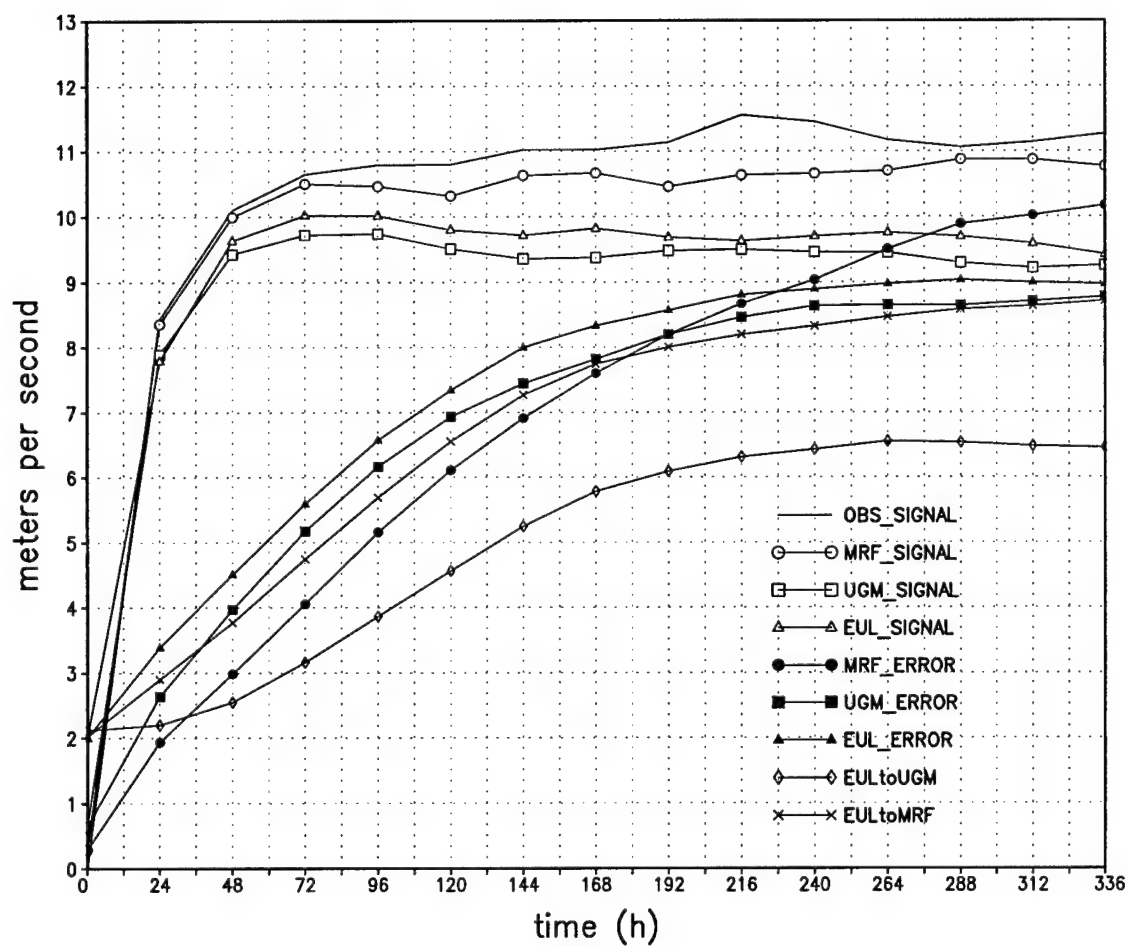
Figure 9.1 displays the time evolution of case-averaged, global rms changes of analyzed (using GDAS analyses) and forecast variables, as described in Chapter 4, for 30 cases from boreal winter 2002/03. Depicted are global rms changes of analyzed height (Fig. 9.1a) and wind (Fig. 9.1b) (solid) as well as the global rms magnitude of the forecast change for these variables for the MRF (open circles), UGM (open squares), and Euler model (open triangles). Additionally, Fig. 9.1 shows the forecast error for the height and wind for the MRF (closed circles), UGM (closed squares) and Euler model (closed triangles), as well as two measures of sensitivity of height and wind forecasts to model selection. Model sensitivity is measured for a change from the Euler model to the UGM (diamonds) and from the Euler model to the MRF (xs).

As described in Chapter 4, the top (solid) curves of Fig. 9.1a and Fig. 9.1b depict an approximate measure of the observed change in the signal associated with each field (i.e., the error of a persistence forecast). Below these curves are the rms evolution of each field from initial to forecast time (model signals) for each of the three models. For both the height and the wind



(a)

Fig. 9.1. Time evolution of global, case-averaged rms 500-mb heights and winds for the boreal winter 2002/03 30-case sample. The top curve (solid) depicts the differences of the analyzed variable at the time indicated along the abscissa minus the value at 0 h. The second curve (open circles) depicts the differences of the MRF forecast variable at the time indicated minus the analysis at 0 h. The third curve (open triangles) depicts the differences of the Euler model forecast variable at the time indicated minus the analysis at 0 h. The fourth curve (open squares) depicts the differences of the UGM forecast variable at the time indicated minus the analysis at 0 h. The fifth curve (closed triangles) depicts the rms error of the variable forecast by the Euler model. The sixth curve (closed squares) depicts the rms error of the variable forecast by the UGM. The seventh curve (xs) depicts the difference of the Euler forecast variable minus the MRF forecast variable, and measures the sensitivity of the forecasts to the model used. The eighth curve (closed circles) depicts the rms error of the variable forecast by the MRF. The ninth curve (diamonds) depicts the difference of the Euler forecast variable minus the UGM forecast variable, and also measures the sensitivity of the forecasts to the model used. Curves in (a) are for 500-mb heights, and curves in (b) are for 500-mb meridional wind.



(b)

Fig. 9.1. (continued)

field, the MRF (open circles) maintains slightly less variability than the atmosphere, except for the height field at long lead times (after 288 h). The Euler model (open triangles) and UGM (open squares) both retain even less variability than does the MRF, although the Euler model signal is slightly stronger than that of the UGM for both variables at all forecast times. This is consistent with the weaker diffusion used in the Euler model compared to the UGM, described in Chapter 7 as one of the inherent differences between the two models.

Below the model signal curves are the rms errors for the height and wind for the MRF (closed squares), UGM (closed circles) and Euler model (closed triangles). As seen in Chapter 4, these curves asymptote toward the respective model forecasted signals after day eight for the winds, with slower relative error growth for the height field.

The final two curves of Fig. 9.1 measure the sensitivity of the height and wind forecasts to the model used. For the 30-case sample, this measure of sensitivity for a change from the Euler model to the UGM (diamonds) is less than the forecast error of the three models. This supports the idea that the Euler model and UGM, started from the same initial conditions, resemble each other more than either resembles reality. The sensitivity for a change from the Euler model to the MRF (xs) surpasses (for the height) or approaches (for the wind) the forecast error curves for the three models. Therefore, the Euler model's ability to anticipate the evolution of a more sophisticated, higher-resolution model is approximately as good as the ability of each of the models to predict the atmosphere. The fact that the sensitivity for a switch from the Euler model to the UGM is nearly two-thirds the value of the sensitivity for a switch from the Euler model to the MRF is evidence that, although the Euler model and UGM have similar bias and error fields, there are systematic differences between the two models that results in disparate forecast evolution. Determining the relative contributions of the three inherent differences in Euler model and UGM formulation detailed in Chapter 7 is beyond the scope of the current study.

CHAPTER 10

SUMMARY AND CONCLUSIONS

This study has investigated predictability using four different global forecast models, and three different estimates of the initial state selected from reanalyses for 1993 and operational data for boreal winter 2002/03. Our approach has been to compare the different model forecasts and errors, and the sensitivity of forecasts to the model, to model resolution, and to the initial state. One of the models (the experimental UGM) was applied with all three analyses (ECMWF and NCEP-NCAR reanalyses for 1993/2003 and GDAS analyses for 2003). The Euler model was initialized only with the GDAS analyses for 2003, and the other models are different versions of formerly and currently operational MRF models initialized with NCEP analyses.

The comparison of results of experimental models with operational models allows more predictability inferences than would the use of a single operational model. The strategy has been to maintain substantially lower resolution and a simplified physical parameterization in the UGM and Euler model than is available in the MRF. This allows for the assessment of the roles of resolution and of model sophistication relative to the improvements of the initial state specification. The relative contributions of these separate improvements cannot be determined from a single forecast system in which model initialization as well as sophistication are changing simultaneously. The first guess is such an important component of the data assimilation cycle that model advances will lead to initial state advances. Consequently, the value of

individual contributions is not entirely clear even in the present approach, but the strategy does help sharpen the questions and diagnostic methods.

Earlier low-resolution experiments by MMP were expanded from 5 to 14 days. Additionally, some experiments were performed with doubled resolution, and modified estimates of initial state uncertainty. The relative magnitude of the forecast uncertainty associated with model changes was compared to the role of the initial state uncertainty estimates. The main results are summarized below.

The results of the 1993 reanalysis cases suggest that model bias extraction produces more benefit to 14 days than do other tested modifications of the model, including changes to the model heating. Bias-corrected anomaly correlations produced by the UGM lag MRF bias-corrected anomaly correlations by about 12 h to day 6 (144 h), and become very similar to the MRF bias-corrected anomaly correlations by day 7 (168 h). Bias corrected anomaly correlations fall below 0.6 after 6.5 days for the UGM initialized with the NCEP-NCAR reanalyses and fall below 0.6 after 7 days for the UGM initialized with ECMWF reanalyses. These results suggest that the bias-corrected forecasts of a relatively simple research model such as the UGM have almost as much value in predicting large-scale features as those obtained from a more highly developed model such as the MRF that was used operationally until approximately 1995.

The results for the 2003 real-time sample suggest that the operational MRF has gained approximately 36-48 h of forecast value (depending on sample size) since the earlier experiments, and exhibits bias-corrected anomaly correlations of approximately 0.6 past 8 days for the presently studied samples. Meanwhile the UGM executed with the more recent data has increased the period of useful predictability by only approximately 6-16 h (depending on sam-

ple size) relative to the 1993 data, and gains only 3 h predictive skill when executed at doubled horizontal resolution. It is possible that the extra 30-h gain made by the MRF is due to the model advances at NCEP rather than improvements of the initial state. Although this possibility cannot be discounted, the error patterns of the low-resolution UGM, low-resolution Euler model, and high-resolution MRF show strong positive correlation through the prediction, suggesting that much of the remaining error may be explained by some common deficiency of all three models.

The MRF contains certain inherent advantages in the balance of initial fields, since the same model is incorporated to provide the initial guess fields for the analyses. The UGM interpolates the reanalyses values to UGM grid points using spherical harmonic representation, and the Euler model uses local linear interpolation. Since the short-term evolution includes a spinup time for both models to adjust to small local imbalances, initialization procedures will favor the more sophisticated MRF model. In view of these simplifications for the UGM and Euler models it is somewhat surprising that the length of skillful forecasts does not differ by more than roughly 12 h for the 1993 sample. This result is consistent with the possibility that those predictions were not strongly limited by differences in model sophistication, but were more limited by uncertainty in the initial state.

To better understand the sensitivity to model heating, all UGM experiments presently shown were repeated by substituting climatological values obtained from reanalysis archives for model-generated values of radiative heating of the atmosphere. All statistics matching those displayed in this paper, as well as individual forecasts, were remarkably similar to the UGM forecasts in which internally consistent physical parameterizations were computed rather than prespecified, and are not shown. Similar experiments were made with changes to

the UGM values of diffusion for divergence and moisture, will little resulting differences in large-scale flow predictions.

The spectrally binned experiments performed by MMP, and extended here to 14 days, were also performed with the UGM at doubled horizontal resolution using both 1993 and 2003 data. These experiments resulted in modifications of previous hypotheses regarding the importance to forecast evolution of the uncertainty of long waves relative to the uncertainty of short waves in the initial state. Doubled model resolution incorporated more detail from the GDAS analyses at shorter wavelengths, allowing significantly more forecast sensitivity to the smaller scales of the initial state, particularly in the first few days of prediction. However, uncertainty in the larger scales of the initial state still plays an important role in medium- and long-range forecasts. Such results point to the importance of detailed analyses at all scales for improved global weather prediction.

Our experiments indirectly suggest that a major benefit enjoyed by the current version of the MRF is the extra resolution of that model (T254 and T170) relative to the other models tested in the present experiments (highest resolution of T84). As previously discussed, higher resolution also produces more sensitivity to the initial state, possibly allowing for a more complete accounting for the many initial state improvements that have been incorporated into the analyses since 1993.

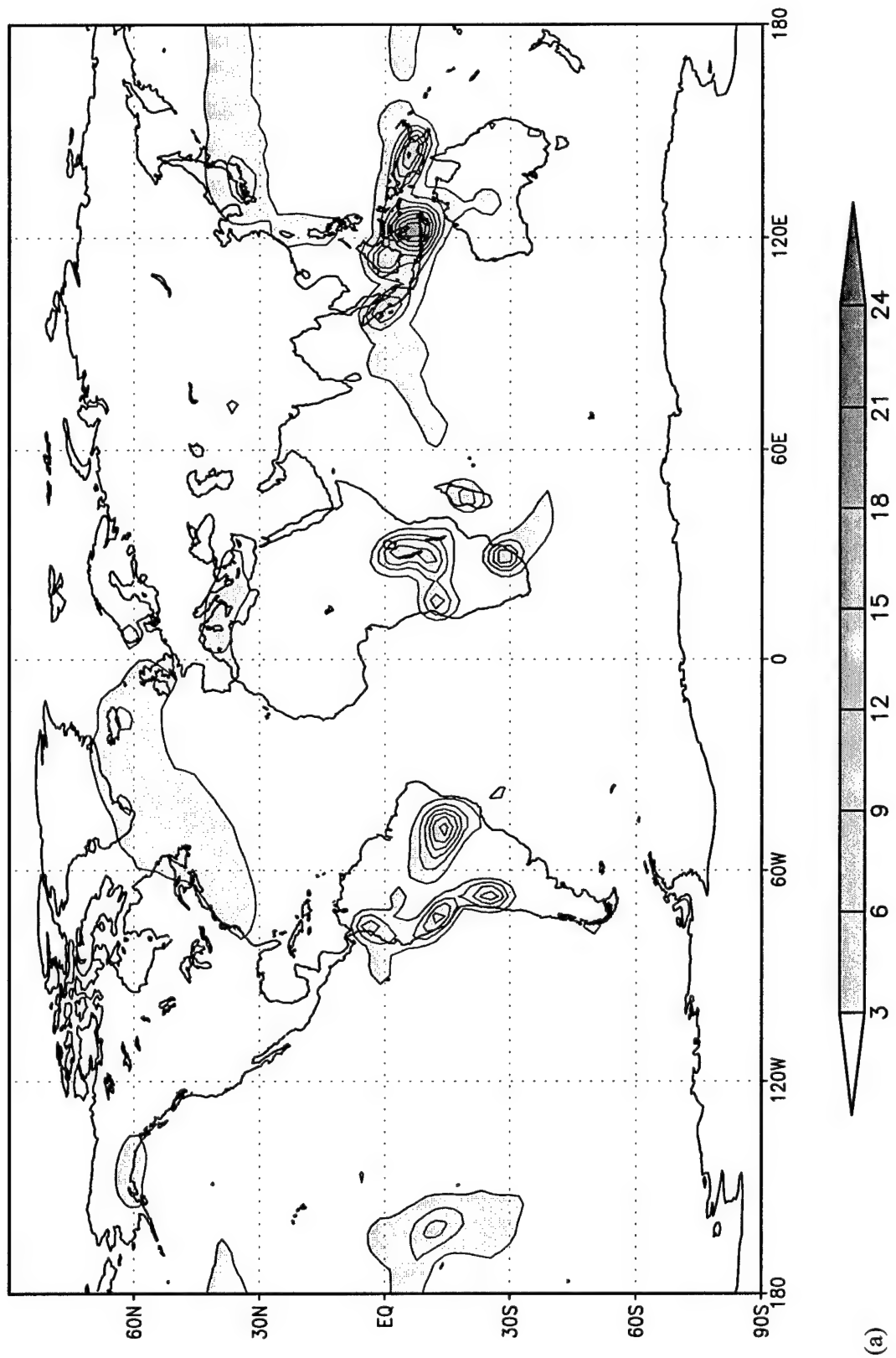
The importance of model physics to predictive skill was not explicitly tested in the present study. The UGM and Euler models have very simple physical parameterizations compared to those used in both versions of the MRF utilized here. Still, despite the fact that Euler model's large-scale predictive skill was comparable to (not bias corrected) or less than (bias corrected) that of the UGM, the Euler model appears to evolve more realistic smaller-scale

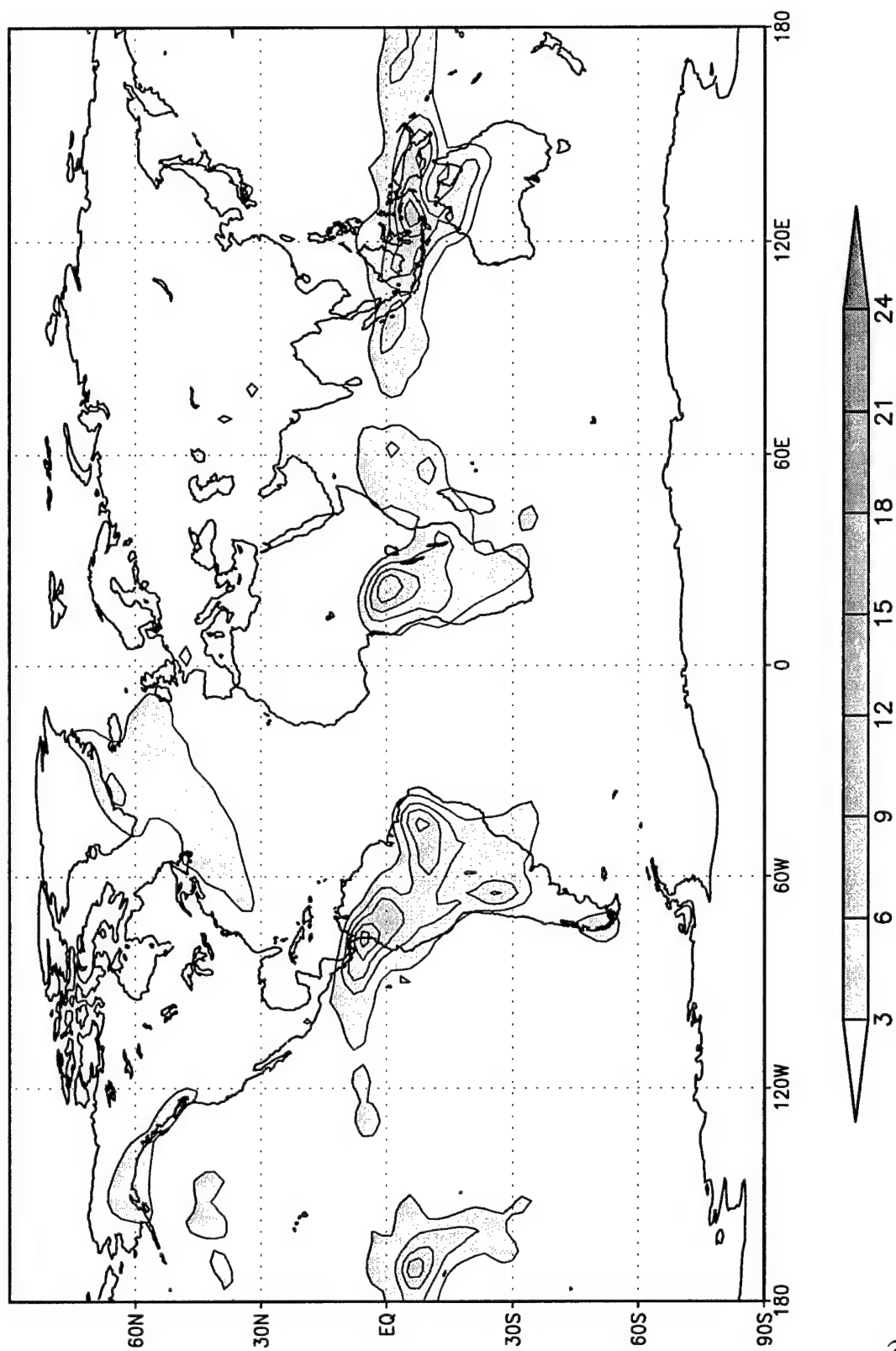
physical processes, such as precipitation. Figure 10.1 is a comparison of the average of 14 consecutive days from boreal winter 2003 for the accumulated precipitation at day 11 for the UGM (Fig. 10.1a), Euler model (Fig. 10.1b), and the MRF (Fig. 10.1c). UGM precipitation is unrealistically tied to the orography (i.e., the Andes) as a result of frictional effects and the use of sigma coordinates, and although the UGM rains more than the Euler model, the precipitation from the UGM tends to be concentrated in “bulls-eyes” throughout the globe. The areal coverage of the Euler model precipitation forecast is more realistic and more closely approaches that of the MRF. Still, neither the UGM nor the Euler model is close to producing the type of precipitation features evident in the more sophisticated MRF model, and none of the models accurately reflects observed precipitation values for the period of interest, shown for South America in Fig. 10.2.

Although the models do exhibit forecast differences and have varying complexities, resolutions and dynamical core, all three produced striking similarities in 500-mb meridional wind biases by day 14. These similarities hint at some common deficiency in these models which, if present in all numerical models, would have important implications for ensemble forecasting. If all models tended to diverge from reality in similar ways, ensemble methods may not add value to the long-range forecast process.

All speculations could be checked by repeating the experiments displayed here using a much higher resolution, more sophisticated model for experimental forecasts and systematically modifying its input, resolution, and model parameterizations to quantify the role of model resolution and sophistication on predictive skill. Comparison of the forecast, bias and error fields from a fourth, independent model with those from the UGM, Euler and MRF models would also allow further assessment of the role of improvements in initial state specification.

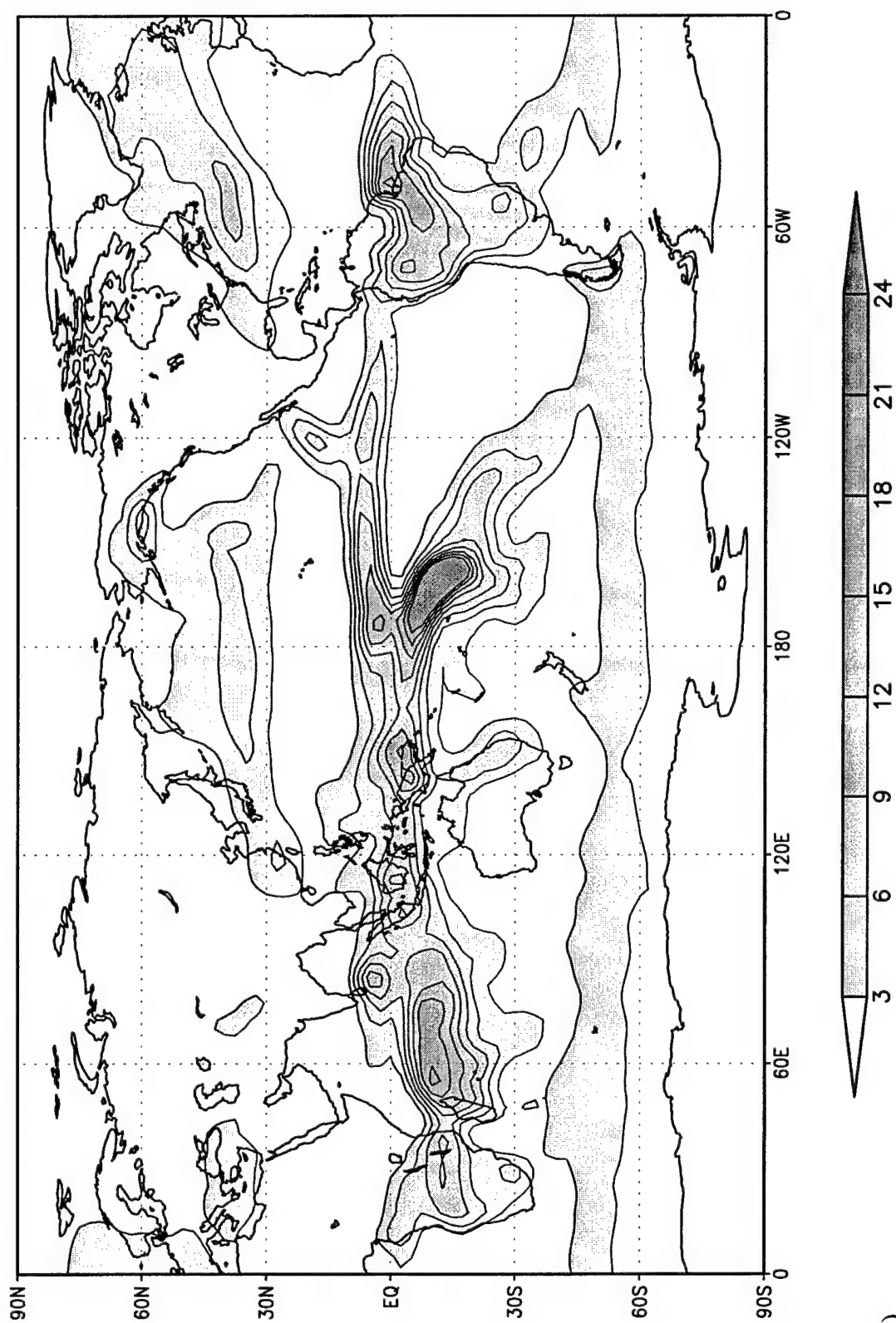
Fig. 10.1. Total accumulated precipitation at forecast day 11, averaged over 14 consecutive days from 28 Jan 2003 through 10 Feb 2003. Totals are shown for the (a) UGM, (b) Euler model, and (c) MRF models. Units are in centimeters.





(b)

Fig. 10.1. (continued)



(c)

Fig. 10.1 (continued)

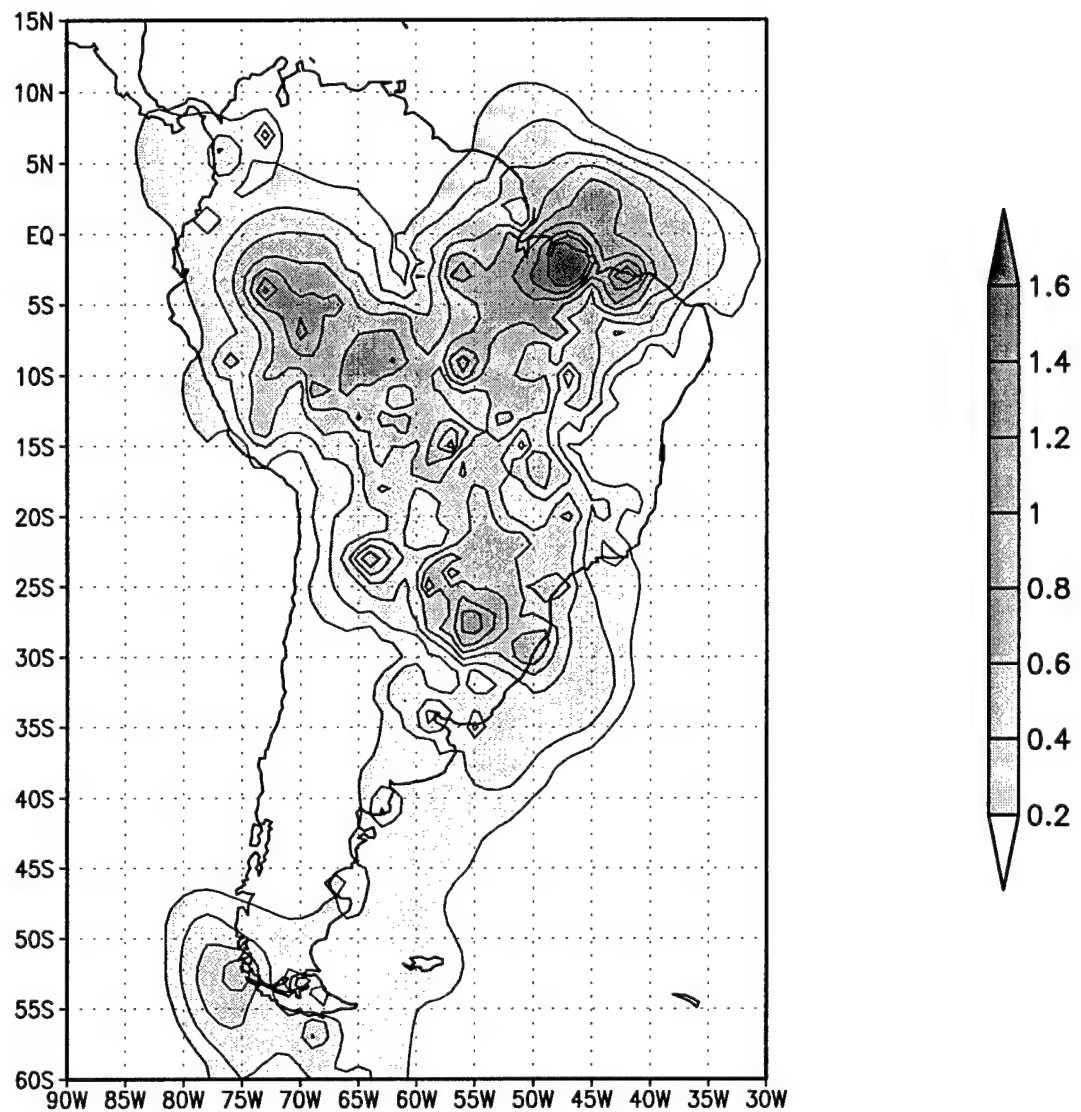


Fig. 10.2. Total accumulated daily precipitation from the Climate Prediction Center, averaged over 14 consecutive days from 8 Feb 2003 through 21 Feb 2003. Units are in centimeters.

APPENDIX A

EULER MODEL DESCRIPTION

The governing equations for zonal, meridional, and vertical flows (u , v , and w) and for pressure, potential temperature, and specific humidity (p , θ , and q) are

$$\begin{aligned} \frac{\partial u}{\partial t} + \vec{V} \cdot \nabla u - f v - \frac{uv}{r} \tan \varphi - 2\Omega v \sin \varphi = \\ - \frac{1}{\rho r \cos \varphi} \left[\frac{\partial}{\partial \lambda} p' + \frac{\partial}{\partial z} p' \left(\frac{\bar{s}}{s - z_G} \right) \left(\frac{z^* - \bar{s}}{\bar{s}} \frac{\partial z_G}{\partial \lambda} - \frac{z^*}{\bar{s}} \frac{\partial s}{\partial \lambda} \right) \right] + F_u \end{aligned} \quad (\text{A.1})$$

$$\begin{aligned} \frac{\partial v}{\partial t} + \vec{V} \cdot \nabla v + f u + \frac{u^2}{r} \tan \varphi = \\ - \frac{1}{\rho r} \left[\frac{\partial}{\partial \varphi} p' + \frac{\partial}{\partial z} p' \left(\frac{\bar{s}}{s - z_G} \right) \left(\frac{z^* - \bar{s}}{\bar{s}} \frac{\partial z_G}{\partial \varphi} - \frac{z^*}{\bar{s}} \frac{\partial s}{\partial \varphi} \right) \right] + F_v \end{aligned} \quad (\text{A.2})$$

$$\begin{aligned} \frac{\partial w}{\partial t} + \vec{V} \cdot \nabla w - \frac{u^2 + v^2}{r} - 2\Omega u \cos \varphi = \\ \alpha \left[-\frac{1}{\rho} \frac{\partial}{\partial z^*} p' \left(\frac{\bar{s}}{s - z_G} \right) - \frac{p'}{\rho} g \right] + F_w \end{aligned} \quad (\text{A.3})$$

$$\begin{aligned} \frac{\partial}{\partial t} p' + \vec{V} \cdot \nabla p' - \rho_s g w = \\ \delta \left(-\gamma p \left\{ \frac{1}{r \cos \varphi} \left[\frac{\partial u}{\partial \lambda} + \left(\frac{\partial u}{\partial z^*} \right) \left(\frac{\partial z_G}{\partial \lambda} \right) \left(\frac{z^* - \bar{s}}{s - z_G} \right) \right] + \frac{1}{r} \left[\frac{\partial v}{\partial \varphi} + \left(\frac{\partial v}{\partial z^*} \right) \left(\frac{\partial z_G}{\partial \varphi} \right) \left(\frac{z^* - \bar{s}}{s - z_G} \right) \right] + \right. \right. \\ \left. \left. \frac{\partial w}{\partial z^*} \left(\frac{\bar{s}}{s - z_G} \right) \right\} \right) + \frac{\gamma p}{\theta} (Q + F_\theta) \end{aligned} \quad (\text{A.4})$$

$$\frac{\partial \theta}{\partial t} + \vec{V} \cdot \nabla \theta = Q + F_\theta \quad (\text{A.5})$$

$$\frac{\partial q}{\partial t} + \vec{V} \cdot \nabla q = E - P - F_q . \quad (\text{A.6})$$

Here λ , φ , and r are longitude, latitude, and the earth's radius, \vec{V} is the velocity vector, f is the Coriolis parameter, Ω is the angular speed of the earth's rotation, ρ is the density of air, s is the material surface top of the model, \bar{s} is the initial height of the material surface, z^* is the terrain-following vertical coordinate, z_G is the ground elevation, g is gravity, Q is the diabatic heating, E is evaporation, P is precipitation, and F_X (where X is u , v , w , θ , or q) is turbulent mixing. The terrain slope angle is neglected for radiation calculations in present applications. The parameters α and δ are artificial parameters used to slow down horizontal and vertical sound wave propagation, and are set equal to 1.0. The ratio of specific heats, γ , is 1.4.

Turbulent mixing is defined as

$$F_X = \nabla_H \cdot (K_H \nabla_H X) + \frac{\partial}{\partial z} \left(\hat{K} \frac{\partial X}{\partial z} \right) = \nabla_H \cdot [K_H \nabla_H X] + \left(\frac{\bar{s}}{s - z_G} \right)^2 \left[\frac{\partial}{\partial z^*} \left(\hat{K} \frac{\partial X}{\partial z^*} \right) \right] \quad (\text{A.7})$$

where K_H , the horizontal exchange coefficient, is equal to $0.36(r \times \Delta\varphi)^2 \sqrt{(\nabla \cdot \vec{K} \times \vec{V})^2}$, and is bounded by $(2r\Delta\varphi)^2 / 10^7 \approx 2.4 \times 10^4 \text{ m}^2 \text{ s}^{-1}$. The vertical exchange coefficient, \hat{K} , is given by a level 2.5 prognostic turbulence treatment, as in Nicolini et al. (1993).

The diabatic heating, Q , includes radiative and latent heating, as described by Nicolini et al. (1993), and the thermodynamic equation includes surface heat balance and subsurface temperature prediction on five levels below the soil, as described by Paegle and McLawhorn (1983).

Advection is computed as

$$\vec{V} \cdot \nabla \Gamma = \frac{u}{r \cos \varphi} \frac{\partial \Gamma}{\partial \lambda} + \frac{v}{r} \frac{\partial \Gamma}{\partial \varphi} + w^* \frac{\partial \Gamma}{\partial z^*} \quad (\text{A.8})$$

The vertical coordinate, z^* , follows the topography and is defined by

$$z^* = \frac{\bar{s}(z - z_G)}{(s - z_G)} \quad (\text{A.9})$$

as in Mahrer and Pielke (1977) (see Figure A.1). If s equals \bar{s} =altitude of the top of the model atmosphere (constant), then

$$w^* = \frac{\bar{s}}{s - z_G} w - \frac{\bar{s} - z^*}{s - z_G} (\vec{V} \cdot \nabla z_G) \quad (\text{A.10})$$

Additionally, the pressure perturbation, p' , is introduced in order to minimize truncation error in the vicinity of steep terrain in the calculation of pressure gradient forces. The total pressure is $p = p_s + p'$, and the reference state pressure, p_s , depends only on z .

The dependent variables are vertically staggered, as in Figure A.2. The equations governing p' and w are coupled into a single equation for the forecasted w at time step $n+1$. The time and vertically discretized equation for p'^{n+1}_k is

$$\begin{aligned} \frac{p'^{n+1}_k - p'^{n-1}_k}{2\Delta t} + (\vec{V} \cdot \nabla p')^n_k - \left\{ \frac{\rho_{s,k} g}{2} \left[\frac{(1+\beta)}{2} w^{n+1}_{k-1} + \frac{(1-\beta)}{2} w^{n-1}_{k-1} + \right. \right. \\ \left. \left. \frac{(1+\beta)}{2} w^{n+1}_k + \frac{(1-\beta)}{2} w^{n-1}_k \right] \right\} = \delta \left\{ -\gamma p_k \left[\frac{1}{r \cos \varphi} \left(\frac{\partial \bar{u}^n_k}{\partial \lambda} + \frac{\partial \bar{u}^n_k}{\partial z^*} \left(\frac{\partial z_G}{\partial \lambda} \right) \left(\frac{z^* - \bar{s}}{s - z_G} \right) \right) + \right. \right. \\ \left. \left. \frac{1}{r} \left(\frac{\partial \bar{v}^n_k}{\partial \varphi} + \frac{\partial \bar{v}^n_k}{\partial z^*} \left(\frac{\partial z_G}{\partial \varphi} \right) \left(\frac{z^* - \bar{s}}{s - z_G} \right) \right) + \left(\frac{\bar{s}}{s - z_G} \right) \left[\left(\frac{(1+\beta)}{2} w^{n+1}_k + \frac{(1-\beta)}{2} w^{n-1}_k \right) - \right. \right. \right. \\ \left. \left. \left. \left(\frac{(1+\beta)}{2} w^{n+1}_{k-1} + \frac{(1-\beta)}{2} w^{n-1}_{k-1} \right) \right] \right] \right\} / (z'_k - z'_{k-1}) \quad (\text{A.11}) \end{aligned}$$

where $\bar{(\quad)}_k = [(\quad)_k + (\quad)_{k+1}]/2$ and $\beta=1$ is used to produce a fully implicit backward

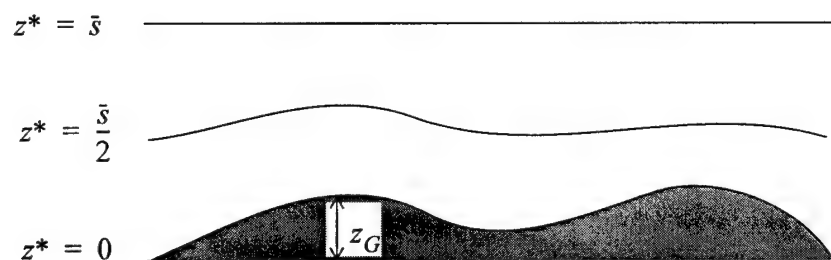


Fig. A.1. Diagram of Euler model vertical coordinate.

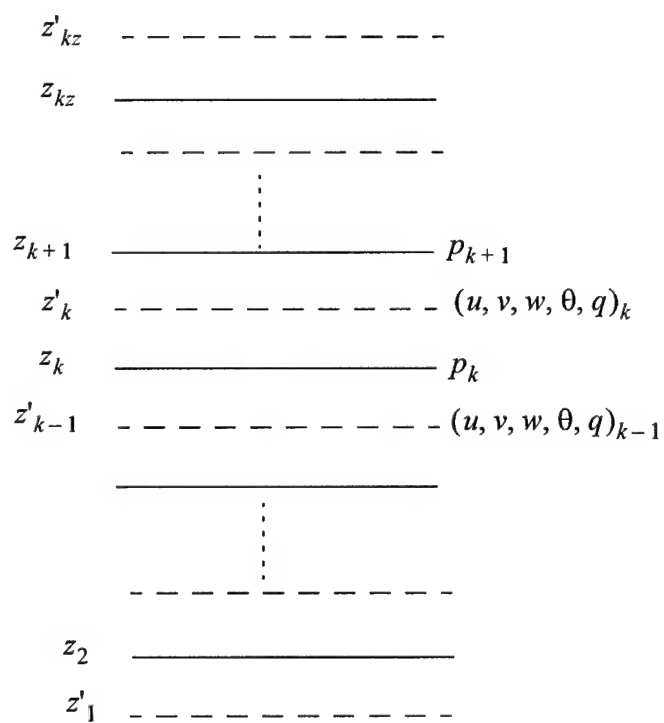


Fig. A.2. Vertical staggering of dependent variables.

scheme. A similar equation is used to obtain p'_{k+1}^{n+1} and these equations are solved for p'_k^{n+1}

and p'_{k+1}^{n+1} which are inserted in the vertical momentum equation:

$$\frac{w_k^{n+1} - w_k^{n-1}}{2\Delta t} + (\vec{V} \cdot \nabla w)_k^n = \frac{-\bar{s}}{(s - z_G)(z_{k+1} - z_k)} \left[\left(\frac{1-\beta}{2} p'_{k+1}^{n-1} + \frac{1+\beta}{2} p'_{k+1}^{n+1} \right) - \left(\frac{1-\beta}{2} p'_k^{n-1} + \frac{1+\beta}{2} p'_k^{n+1} \right) \right] - \alpha \left(\frac{\rho'}{\rho} g \right)_k^n + F_w^{n+1} \quad (\text{A.12})$$

where $\rho' = (p' - \rho_s RT') / (RT_s)$, $T' = \theta \left(\frac{p}{p_o} \right)^{R/C_p} - T_s + 0.61 q T$, and $\alpha=1$. Basic state ther-

modynamic quantities (T_s , ρ_s , and p_s) are computed from global averages of initial values on

constant height surfaces, and are interpolated to terrain following, z^* , coordinates. The final

equation for w^{n+1} is of the form:

$$A_k w_{k-1}^{n+1} + B_k w_k^{n+1} + C_k w_{k+1}^{n+1} = D_k^n \quad (\text{A.13})$$

where

$$A_k = A'_k - (\hat{K}_{k-1} + \hat{K}_k) / [(z_k - z_{k-1})(z_{k+1} - z_{k-1})] \quad (\text{A.14})$$

$$B_k = B'_k + \left[\frac{(\hat{K}_{k-1} + \hat{K}_k)}{(z_k - z_{k-1})} + \frac{(\hat{K}_k + \hat{K}_{k+1})}{(z_{k+1} - z_k)} \right] / (z_{k+1} - z_{k-1}) \quad (\text{A.15})$$

$$C_k = C'_k - (\hat{K}_k + \hat{K}_{k+1}) / [(z_{k+1} - z_k)(z_{k+1} - z_{k-1})] \quad (\text{A.16})$$

$$\begin{aligned} D_k = & \frac{w_k^{n-1}}{2\Delta t} - (\vec{V} \cdot \nabla w)_k^n - \frac{\bar{s}\alpha}{\rho_k(s - z_G)(z_{k+1} - z_k)} \left[\frac{1-\beta}{2} (p'_{k+1}^{n-1} - p'_k^{n-1}) \right] - \\ & \frac{\alpha g}{\gamma p_k} \left[\frac{1-\beta}{2} \frac{(p'_k^{n-1} + p'_{k+1}^{n-1})}{2} \right] + \alpha \left(\frac{\rho'}{\rho} \right)_k^n g - \\ & \frac{\bar{s}(\alpha/\rho_k)}{s - z_G} \frac{(1+\beta)}{2(z_{k+1} - z_k)} (E_{k+1} - E_k) + \nabla_H \cdot (K_H \nabla w) \end{aligned} \quad (\text{A.17})$$

$$E_k = p_k^{n-1} - 2\Delta t (\vec{V}_H \cdot \nabla p)_k^n - 2\Delta t \delta \gamma \bar{p}_k \left\{ \frac{\nabla \cdot [\vec{V}_H(s - z_G)]}{(s - z_G)} \right\}_k^n - \left(\frac{\bar{s}}{s - z_G} \right) 2\Delta t \delta \gamma p_k \frac{(1 - \beta)(w_k^{n-1} - w_{k-1}^{n-1})}{2(z'_k - z'_{k-1})} + 2\Delta t \left[\frac{\rho_{s,k} g(1 - \beta)}{2} (w_{k-1}^{n-1} + w_k^{n-1}) \right] \quad (\text{A.18})$$

$$A'_k = XQ1_k(-XQ2_k - XQ3_k) + XQ4_k(XQ2_k + XQ3_k) \quad (\text{A.19})$$

$$B'_k = \frac{1}{2\Delta t} - XQ1_k(-XQ2_k - XQ2_{k+1} + XQ6_k) + XQ4_k(-XQ2_k + XQ3_k) + XQ4_k(XQ2_{k+1} + XQ3_{k+1}) \quad (\text{A.20})$$

$$C'_k = XQ1_k(-XQ2_{k+1} + XQ3_{k+1}) + XQ4_k(-XQ2_{k+1} + XQ3_{k+1}) \quad (\text{A.21})$$

and the following definitions apply:

$$XQ1_k = \frac{(\bar{s}\alpha/\rho_k)(1 + \beta)}{2(s - z_G)(z_{k+1} - z_k)} \quad (\text{A.22})$$

$$XQ2_k = \frac{2\Delta t \delta \gamma (1 + \beta)}{2(z'_k - z'_{k-1})} p_k \left(\frac{\bar{s}}{s - z_G} \right) \quad (\text{A.23})$$

$$XQ3_k = \frac{2\Delta t g(1 + \beta)}{2} \rho_{sk} \quad (\text{A.24})$$

$$XQ4_k = \alpha \frac{g(1 + \beta)}{\gamma p_k} \frac{1}{4} \quad (\text{A.25})$$

$$XQ6_k = \frac{2\Delta t g(1 + \beta)}{2} (\rho_{s,k+1} - \rho_{s,k-1}) \quad (\text{A.26})$$

Note that $XQ1_k$, $XQ2_k$, $XQ3_k$, $XQ4_k$, and $XQ6_k$ vary horizontally on terrain-following surfaces, as well as vertically.

The solution for w_k^{n+1} is obtained by Gauss elimination, subject to boundary conditions $w=0$ at the top and bottom of the model. This filters horizontally-propagating, external gravity waves. The solution for w is only slightly affected by horizontal and vertical diffusion,

and the diffusion terms (involving K and K_H) are generally ignored in present applications. After w_k^{n+1} is obtained, these values are used in the equation for pressure to obtain p_k^{n+1} . The parameters α and δ were introduced in early testing of the model. If $\alpha < 1$, then vertical sound wave propagation is slowed by a factor $\sqrt{\alpha}$. If $\delta < 1$, then three-dimensional sound wave propagation is slowed by the factor $\sqrt{\delta}$. These tactics are not employed in any of our integrations.

The equations for horizontal momentum and for specific humidity use centered time differencing to approximate $\partial(\)/\partial t$

$$\left. \frac{\partial(\)}{\partial t} \right|_n \Rightarrow \frac{(\)^{n+1} - (\)^{n-1}}{2\Delta t} \quad (\text{A.27})$$

and all terms in these equations, with the exception of horizontal and vertical diffusion are specified at time step n . Horizontal diffusion is specified at time step $n-1$ and vertical diffusion at time step $n+1$.

The vertical structure of solutions for u , v , and q are expanded in finite element representation, and the resulting implicit equations for u , v , and q are of the form

$$a_k \Gamma_{k-1} + b_k \Gamma_k + c_k \Gamma_{k+1} = d_k \quad (\text{A.28})$$

where $\Gamma_k = u_k, v_k, \text{ or } q_k$ and solutions for Γ_k are obtained subject to lower and upper boundary conditions on Γ_1 and Γ_{kz} . For wind components, $\Gamma_1 = 0$, while for specific humidity the lower boundary condition specifies either q_1 at a water surface or $(dq/dz)_1$ at a land surface. In the latter case, the vertical gradient of q depends upon surface evaporation. The top boundary condition maintains Γ_{kz} equal to the initial value.

The equations for atmospheric potential temperature (θ) and for soil temperature (T_s) also use centered time differencing and all terms of these equations, with the exception of horizontal and vertical diffusion, are specified at time step n . Horizontal diffusion is specified at time step $n-1$ and vertical diffusion at time step $n+1$.

Figure A.3 shows the vertical distribution of temperature variables and governing equations in the atmosphere, interface and subsurface. Here ρ , c , and K represent density, specific heat, and vertical diffusivity for the atmosphere (subscript A) or the soil (subscript s). T_s is soil temperature and F_N , G_r and LHF are infrared, solar and latent heat fluxes at the surface.

The vertical structure of θ in the atmosphere and of T_s in the soil are expanded in finite elements, leading to tri-diagonal algebra. The interface condition uses

$$\frac{\theta_2 - \theta_1}{z'_1 - z_0} \Rightarrow \frac{\partial \theta}{\partial z} \Big|_{sfc} \quad \frac{T_{s,0} - T_{s,-1}}{z_0 - z_{-1}} \Rightarrow \frac{\partial T_s}{\partial z} \Big|_{sfc} \quad (\text{A.29})$$

and internally computed surface infrared flux, F_N , and surface solar radiative flux, G_r . LHF is currently prespecified. Here \hat{K} , K_A , and K_s are conductivities of air (\hat{K} and K_A) and soil or water (K_s), and may differ from the diffusivity used in the other equations. The surface type is specified by ρ_s , c_s , and K_s , and varies with soil type or water. Roughness length, z_0 , is prespecified, as is the subsurface temperature at z_{bottom} .

The vertical structure solution for θ^{n+1} and T_s^{n+1} consists of a single tri-diagonal matrix inversion, extending from z_{bottom} to z'_{kz} .

The horizontal variation is carried on a "b-grid," with horizontal flow variables depicted on a staggered grid with respect to other variables (see Figure A.4). The model uses a spherical coordinate, and the poles carry w , p' , θ , and q .

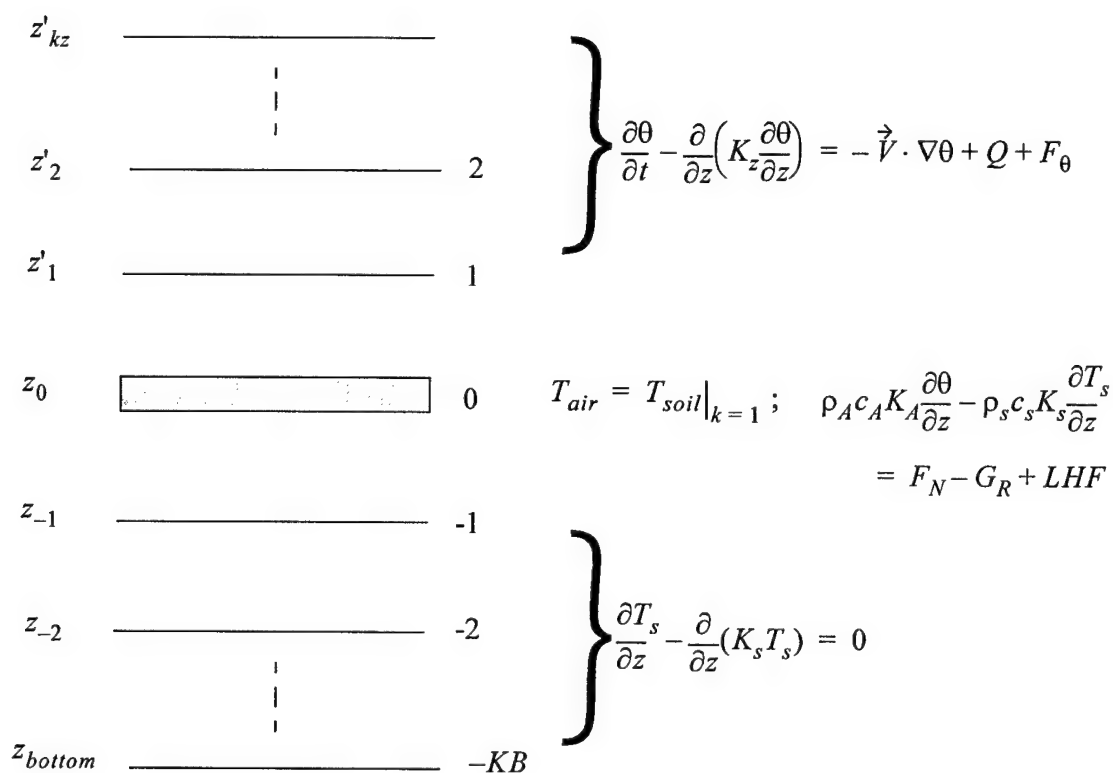


Fig. A.3. Vertical distribution of temperature variables and governing equations in the atmosphere, interface and subsurface.

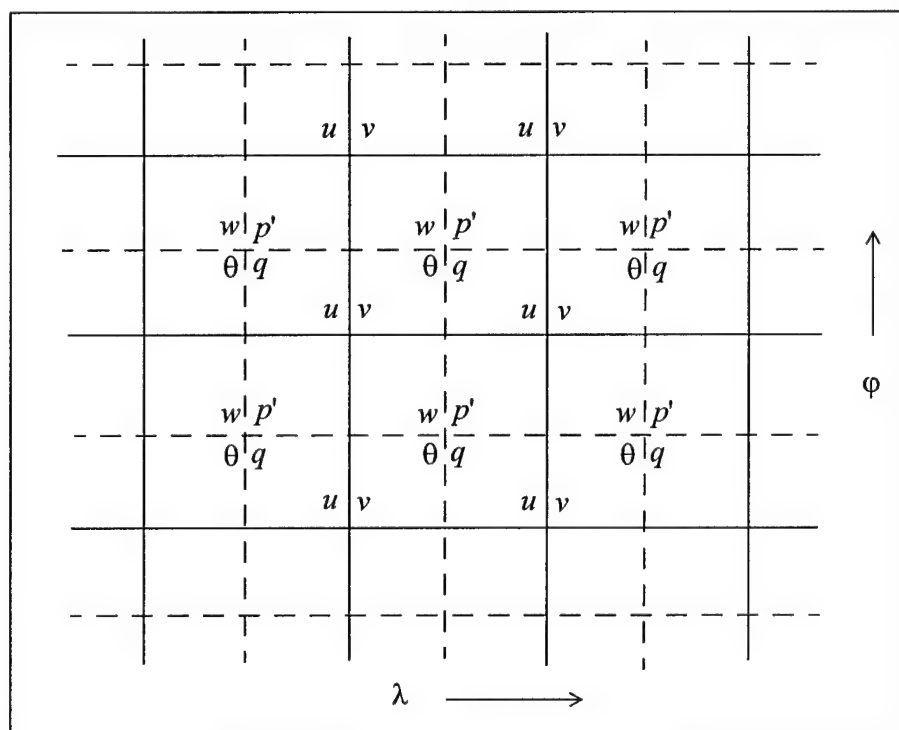


Fig. A.4. Euler model "b-grid" used to represent horizontal variation of variables.

All advection terms are rewritten

$$\vec{V} \cdot \nabla \Gamma = \vec{V}_H \cdot \nabla_H \Gamma + w \frac{\partial \Gamma}{\partial z} = \nabla_H \cdot (\vec{V} \Gamma) - \Gamma (\nabla_H \cdot \vec{V}_H) + w \frac{\partial \Gamma}{\partial z} \quad (\text{A.30})$$

where $\vec{V}=(u,v)$ and

$$\nabla_H() = \frac{1}{r \cos \varphi} \frac{\partial()}{\partial \lambda} i + \frac{1}{r} \frac{\partial()}{\partial \varphi} j \quad (\text{A.31})$$

Calculation of fluxes on the staggered “b-grid” is done in the usual manner by averaging wind components and the fluxed quantity to common intermediate points.

The model retains options to use finite difference or finite element (compact implicit) approximations for flux divergence. The finite element approach appears to be more accurate and more stable, and is used presently.

Convergence of meridians produces severe time step restrictions. A fourier filter is applied in longitude to alleviate this problem. The filter removes all longitudinal waves with wavelength less than the shortest wavelength locally resolved in latitude.

The model also has options for variable latitude grid spacing and for a mathematical coordinate rotation that allow a region of telescoping, refined resolution within a selected sub-domain, similar to the method described for the UGM (primitive equation model) in Paegle (1989.)

The model is similar to that described by Dudhia and Bresch (2002), but uses a single, unified coordinate (rather than the patched map projection used by Dudhia and Bresch) and allows variable resolution. The current model does not incorporate time splitting for acoustic modes (as used by Dudhia and Bresch). It, therefore, requires a small time step and is relatively computationally slow.

APPENDIX B

ASYMPTOTIC LIMITS FOR CORRELATION COEFFICIENT

The correlation coefficients of the error of the 500-mb meridional flow forecast by the UGM correlated with the error of the same variable forecast by the MRF is calculated by

$$\text{corr coeff} = \frac{\overline{(V_U - V_A)(V_M - V_A)}}{[\overline{(V_U - V_A)^2} \overline{(V_M - V_A)^2}]^{1/2}}, \quad (\text{B.1})$$

where V_U , V_M , and V_A are the UGM-predicted, MRF-predicted and analyzed 500-mb meridional winds, respectively, and $\overline{(\)}$ represents the global average. This measure of error correlation asymptotes to a nonzero value at long times when predictability is lost due to initial state uncertainty and to the chaotic nature of the atmosphere. The limiting value appears to be approximately 0.5 in long simulations, and a similar value can also be expected from the following analysis.

The correlation can be expanded as

$$C = \frac{(\overline{V_U V_M} - \overline{V_U V_A} - \overline{V_M V_A} + \overline{V_A^2})}{[(\overline{V_U^2} + \overline{V_A^2} - 2\overline{V_U V_A})(\overline{V_M^2} + \overline{V_A^2} - 2\overline{V_M V_A})]^{1/2}}. \quad (\text{B.2})$$

After a sufficiently long time, random errors of the initial state would amplify differently in the two models, which might then diverge sufficiently from reality and from each other so that the average of many forecasts would imply

$$\overline{V_M V_U} = \overline{V_M V_A} = \overline{V_U V_A} = 0; \quad \overline{V_M^2} = \overline{V_U^2} = \overline{V_A^2}. \quad (\text{B.3})$$

In this case, C approaches 0.5 in the long time limit average of many forecasts. Since the models are not nearly perfect, and the UGM systematically underestimates the wave activity, the precise value to which C should asymptote in the long time limit of vanishing predictability is unclear, but empirical evidence points to a value close to 0.5.

REFERENCES

- Bath, L. M., M. A. Dias, D. L. Williamson, G. S. Williamson, and R. J. Wolski, 1987: User's guide to NCAR CCM1. Tech. Rep. NCAR/TN-286+IA, 173 pp.
- Baumhefner, D., and P. Downey, 1978: Forecast intercomparisons from three numerical weather prediction models. *Mon. Wea. Rev.*, **106**, 1245-1279.
- Buchmann, J., L. E. Buja, J. Nogues-Paegle, and J. Paegle, 1995: The dynamical basis of regional vertical motion fields surrounding localized tropical heating. *J. Climate*, **8**, 1217-1234.
- Byerle, L. A., and J. Paegle, 2003: Description of the seasonal cycle of low-level flows flanking the Andes and their interannual variability. *Meteorologica*, **27**, 71-88.
- Dudhia, J., 1993: A non-hydrostatic version of the Penn State-NCAR mesoscale model: validation tests and simulation of an Atlantic cyclone and cold front. *Mon. Wea. Rev.*, **121**, 1493-1513.
- , and J. F. Bresch, 2002: A global version of the PSU-NCAR mesoscale model. *Mon. Wea. Rev.*, **130**, 2989-3007.
- Gibson, J. K., P. Kallberg, S. Uppala, A. Nomura, A. Hernandez, and E. Serrano, 1997: ERA description. ECMWF Re-Analysis Project Report Series, No. 1, 58 pp.
- Hacker, J. P., E. S. Krayenhoff, and R. B. Stull, 2003: Ensemble experiments on numerical weather prediction error and uncertainty for a North Pacific forecast failure. *Wea. Forecasting*, **18**, 12-31.
- Hart, K. A., 2004: An evaluation of high-resolution modeling and statistical forecast techniques over complex terrain. Ph.D. dissertation, University of Utah, 104 pp.
- Hartmann, D. L., R. Buizza, and T. N. Palmer, 1995: Singular vectors: The effect of spatial scale on linear growth of disturbances. *J. Atmos. Sci.*, **52**, 3885-3894.
- Kalnay, E., and Coauthors, 1996: The NCEP/NCAR 40-Year Reanalysis Project. *Bull. Amer. Meteor. Soc.*, **77**, 437-471.

Lorenz, E. N., 1969: The predictability of a flow which possesses many scales of motion. *Tellus*, **21**, 289-307.

Mahrer, Y., and R. A. Pielke, 1977: The effects of topography on sea and land breezes in a two-dimensional numerical model. *Mon. Wea. Rev.*, **105**, 1151-1162.

Miguez-Macho, G., and J. Paegle, 1999a: Optimal observation distribution for numerical weather prediction. Preprints, *Third Symp. on Integrated Observing Systems*, Dallas, TX, Amer. Meteor. Soc., 18-23.

-----, and -----, 1999b: Optimal observation distribution for numerical weather prediction. Preprints, *13th Conf. on Numerical Weather Prediction*, Denver, CO, Amer. Meteor. Soc., 23-26.

-----, and -----, 2000: Sensitivity of a global forecast model to initializations with reanalysis datasets. *Mon. Wea. Rev.*, **128**, 3879-3889.

-----, and -----, 2001: Sensitivity of North American numerical weather prediction to initial state uncertainty in selected upstream subdomains. *Mon. Wea. Rev.*, **129**, 2005-2022.

Nicolini, M., K. M. Waldron, and J. Paegle, 1993: Diurnal variations of low-level jets, vertical motion, and precipitation: A model case study. *Mon. Wea. Rev.*, **121**, 2588-2610.

Nogues-Paegle, J., K. C. Mo, and J. Paegle, 1998: Predictability of the NCEP-NCAR reanalysis model during austral summer. *Mon. Wea. Rev.*, **126**, 3135-3152.

Paegle, J., 1989: A variable resolution global model based upon Fourier and finite element representation. *Mon. Wea. Rev.*, **117**, 583-606.

-----, and J. Horel, 1991: The influence of observational uncertainty upon wind-based analyses. Preprints, *Ninth Conf. on Numerical Weather Prediction*, Denver, CO, Amer. Meteor. Soc., 779-782.

-----, and D. McLawhorn, 1983: Numerical modeling of diurnal convergence oscillations above sloping terrain. *Mon. Wea. Rev.*, **111**, 67-85.

-----, Q. Yang, and M. Wang, 1997: Predictability in limited area and global models. *Meteor. Atmos. Phys.*, **63**, 53-69.

Palmer, T. N., R. Gelaro, J. Barkmeijer, and R. Buizza, 1998: Singular vectors, metrics, and adaptive observations. *J. Atmos. Sci.*, **55**, 633-653.

Rabier, F., E. Klinker, P. Courtier, and A. Hollingsworth, 1996: Sensitivity of forecast errors to initial conditions. *Quart. J. Roy. Meteor. Soc.*, **122**, 121-150.

- Reynolds, C. A., P. J. Webster, and E. Kalnay, 1994: Random error growth in NMC's global forecasts. *Mon. Wea. Rev.*, **122**, 1281-1305.
- Semazzi, F. H. M., J. Qian, and J. S. Scroggs, 1995: A global nonhydrostatic semi-Lagrangian atmospheric model without orography. *Mon. Wea. Rev.*, **123**, 2534-2550.
- Simmons, A. J., and A. Hollingsworth, 2002: Some aspects of the improvement in skill of numerical weather prediction. *Quart. J. Roy. Meteor. Soc.*, **128**, 647-677.
- Thompson, P. D., 1957: Uncertainty of initial state as a factor in the predictability of large scale atmospheric flow patterns. *Tellus*, **9**, 275-295.
- Tribbia, J. J., and D. P. Baumhefner, 2004: Scale interactions and atmospheric predictability: an updated perspective. *Mon. Wea. Rev.*, **132**, 703-713.
- Vukicevic, T., and J. Paegle, 1989: The influence of one-way interacting lateral boundary conditions on predictability of flow in bounded numerical models. *Mon. Wea. Rev.*, **117**, 340-350.
- Warner, T. T., R. A. Peterson, and R. E. Treadon, 1997: A tutorial on lateral boundary conditions as a basic and potentially serious limitation to regional numerical weather prediction. *Bull. Amer. Meteor. Soc.*, **78**, 2599-2617.
- White, B. G., J. Paegle, W. J. Steenburgh, J. D. Horel, R. T. Swanson, L. K. Cook, D. J. Onton, and J. G. Miles, 1999: Short-term forecast validation of six models. *Wea. Forecasting*, **14**, 84-108.